

# Derivation of realistic forcing schemes to reproduce turbulent characteristics of round jets on centerline

Thesis by  
Kyupaekc Jeff Rah

In Partial Fulfillment of the Requirements for the  
Degree of  
Doctor of Philosophy

The logo for the California Institute of Technology (Caltech), featuring the word "Caltech" in a bold, orange, sans-serif font.

CALIFORNIA INSTITUTE OF TECHNOLOGY  
Pasadena, California

2020  
Defended July 11, 2019

© 2020

Kyupaek Jeff Rah  
ORCID: 0000-0003-1898-2930

All rights reserved

어머니, 아버지  
감사합니다

## ACKNOWLEDGEMENTS

I would first like to say that I am very grateful to my advisor, Professor Guillaume Blanquart, for teaching me knowledge, providing guidance, giving insights, sharing great ideas, and solving problems that I could not solve myself. I would also like to thank the professors in my thesis committee, Professor Tim Colonius, Dale Pullin, and Melany Hunt, for their patience and willingness to spend their precious time on me.

I would like to acknowledge the previous group members, Simon Lapointe, Jason Schlup, and Nicholas Burali, for helping me out from the beginning, when I did not have much knowledge or skills needed for our researches. I wish to thank the current group members, Chandru Dhandapani, Guillaume Beardsell, Joseph Ruan, and Rachel Krueger, for sharing their knowledge with me throughout my studies. I would also like to thank all of my friends in Pasadena and Los Angeles for spending time with me.

I am thankful for generous funding from the National Science Foundation (CBET 1512771 and 1761690) and from the Air Force Office of Scientific Research (FA9550-16-1-0510) under the supervision of Dr. Chiping Li. In addition, I gratefully acknowledge the financial support from the Samsung Scholarship Foundation.

Finally, I thank my mom, dad, and my younger brother for their unconditional support from Korea, both emotionally and financially, before and after I came to the U.S. when I was fifteen. I have always been feeling grateful and indebted to my mom, dad, and brother for sacrificing a lot for me. I would also like to thank Joey, Dave, and Nathan Baugh for being my American family.

## ABSTRACT

Turbulence forcing techniques are often required in the numerical simulation of statistically stationary turbulent flows. However, the existing forcing techniques are not based on physics, but rather arbitrary numerical methods that sustain the turbulent kinetic energy. In this work, a realistic forcing technique is devised to reproduce the centerline turbulent characteristics of round jets in a triply periodic box.

A velocity forcing term is derived from the Navier-Stokes equations by applying a Reynolds decomposition with the mean velocity of the axisymmetric jet. The result is an anisotropic linear forcing term. A series of direct numerical simulations (DNS) are performed over a range of Reynolds numbers by applying the derived velocity forcing term in a 3D cubic box. The budget of the terms in the kinetic energy equation is found to be very close to the experimental measurement on the centerline. The anisotropy ratio, kinetic energy, and dissipation rate of the simulations are also comparable to experimental values. Finally, the kinetic energy spectrum in the axial direction is presented. With appropriate normalizations, the spectrum agrees well with the round jet spectrum on its centerline.

A similar procedure is applied to passive scalars to derive a scalar forcing term to simulate the centerline mixing properties of round jets. The term is derived from the scalar transport equation using a Reynolds-like decomposition of the scalar field. The equation is closed by applying the known mean velocity and scalar profiles of axisymmetric jets. The result is a combination of a mean gradient term and a linear scalar term. DNS at different Reynolds numbers have been performed with these source terms for unity Schmidt number. Scalar flux values and scaling exponents of scalar energy spectra from simulations are comparable to experimental values. In addition, a dimensional analysis shows that the normalized scalar statistics, such as variance, flux, and dissipation rate, should only be a function of Reynolds number; indeed, such quantities computed from our simulations approach constant values as the Reynolds number increases. The effects of velocity forcing on scalar fields are also investigated; changing velocity forcing terms may result in unstable scalar fields even under the same scalar forcing.

More computations on higher Schmidt number scalars are performed with the same velocity and scalar forcing terms. It is found that the scalar flux values decrease

with increasing Schmidt number for low Reynolds number flows, and reach plateaus as the Schmidt number increases. The flux values also increase with the Reynolds number for all non-unity Schmidt numbers. The scaling exponents of scalar energy spectra are found to decrease with increasing Schmidt number for all Reynolds numbers.

## PUBLISHED CONTENT AND CONTRIBUTIONS

1. Kyupaeck Jeff Rah, Chandru Dhandapani, and Guillaume Blanquart. Derivation of a realistic forcing term to reproduce the turbulent characteristics of round jets on the centerline. *Physical Review Fluids* 3(8):084606, 2018. doi: [10.1103/PhysRevFluids.3.084606](https://doi.org/10.1103/PhysRevFluids.3.084606).  
The author of this thesis performed all simulations, analyzed the data, made the figures, and wrote the manuscript.
2. Kyupaeck Jeff Rah and Guillaume Blanquart. Numerical forcing scheme to generate passive scalar mixing on the centerline of turbulent round jets in a triply periodic box. *Physical Review Fluids*. (Under review).  
The author of this thesis performed all simulations, analyzed the data, made the figures, and wrote the manuscript.

## TABLE OF CONTENTS

Acknowledgements . . . . .	iv
Abstract . . . . .	v
Published Content and Contributions . . . . .	vii
Table of Contents . . . . .	viii
List of Illustrations . . . . .	x
List of Tables . . . . .	xv
Chapter I: Introduction . . . . .	1
1.1 Anisotropy . . . . .	2
1.2 Scaling of energy spectrum . . . . .	3
1.3 Computational cost . . . . .	5
1.4 Objectives and outline . . . . .	6
Chapter II: Velocity forcing scheme to reproduce the turbulent characteristics of round jets on the centerline . . . . .	8
2.1 Previous velocity forcing methods . . . . .	8
2.2 Review of Lundgren’s linear forcing term and motivation . . . . .	10
2.3 Proposed forcing term . . . . .	12
2.3.1 Review of turbulent jets . . . . .	12
2.3.2 Derivation of the forcing term . . . . .	13
2.3.3 Properties of the forcing scheme . . . . .	16
2.3.4 A priori analysis and simulation procedure . . . . .	17
2.3.5 Reynolds numbers . . . . .	19
2.4 Results . . . . .	20
2.4.1 Simulation framework and parameters . . . . .	20
2.4.2 Instantaneous turbulence structures . . . . .	20
2.4.3 Temporal fluctuations . . . . .	23
2.4.4 Vorticity . . . . .	25
2.4.5 Validation against experimental data - energy budget . . . . .	26
2.4.6 Validation against experimental data - single point values . . . . .	27
2.4.7 Validation against experimental data - energy spectra . . . . .	31
2.5 Energy spectra - anisotropy . . . . .	34
2.6 Summary . . . . .	35
Chapter III: A numerical forcing scheme to generate passive scalar mixing on the centerline of turbulent round jets in a triply periodic box . . . . .	37
3.1 Previous scalar forcing methods . . . . .	37
3.2 Proposed forcing term . . . . .	39
3.2.1 Derivation of the forcing term . . . . .	39
3.2.2 Properties of the forcing term . . . . .	41
3.2.3 Dimensional analysis . . . . .	41
3.3 Results . . . . .	43

3.3.1	Simulation procedure	43
3.3.2	Scaling coefficient	44
3.3.3	Instantaneous mixing structures	45
3.3.4	Validation against experimental data - scalar flux	47
3.3.5	Validation against experimental data - scaling exponent of scalar energy spectra	49
3.4	Discussion	52
3.4.1	Simulations with different velocity forcing terms	52
3.4.2	Time scale ratio	53
3.4.3	Effect of velocity forcing on scalar flux	53
3.4.4	Stability of scalar equation	54
3.5	Summary	56
Chapter IV: Effects of Schmidt number on scalar statistics under Jet Centerline forcing		58
4.1	Background	58
4.2	Simulation procedure	61
4.3	Results	61
4.3.1	Instantaneous mixing structures	61
4.3.2	Scaling coefficient	63
4.3.3	Scalar flux	63
4.3.4	Scaling exponent of energy spectra	68
4.3.5	Discussion on the scaling exponent	72
Chapter V: Conclusion		74
5.1	Jet centerline (JC) velocity forcing scheme	74
5.2	JC scalar forcing scheme	74
5.3	Effects of Schmidt number under JC forcing schemes	75
5.4	Significance and future work	76
Appendix A: Uncertainty quantification		77
A.1	Definitions	77
A.2	Modeling	77
A.3	Calculation	78
A.4	Example	80
Appendix B: Resolution test		81
Appendix C: Simulation code (NGA)		84
C.1	Discretization	84
C.2	Temporal integration	85
Bibliography		88

## LIST OF ILLUSTRATIONS

<i>Number</i>	<i>Page</i>
1.1 Isosurface of an instantaneous scalar field in a three-dimensional turbulent box simulation. . . . .	1
1.2 Anisotropy ratio $\frac{\langle\langle u_x'^2 \rangle\rangle}{\langle\langle \mathbf{u}'^2 \rangle\rangle}$ from turbulent round jet experiments [24–31], jet DNS [32, 33], boundary layer [34], and grid turbulence [35], as a function of $Re_\lambda$ . . . . .	2
1.3 A schematic diagram of an energy spectrum, $\phi(\kappa)$ , in log-log scales. . . . .	4
1.4 Scaling exponent $m$ for energy spectra, $\phi \sim \kappa^{-m}$ , computed from turbulent jet experiments. The solid line is a fit found by Mydlarski and Warhaft [43] by using wind tunnel experiments. The dashed line shows $m = 5/3$ . Reprinted from [44], with the permission of AIP Publishing. . . . .	4
1.5 $Re_D$ from turbulent round jet DNS and experiments in log scale, listed in Table 1.1. . . . .	5
2.1 Contours of the velocity, $u_x$ and $u_y$ , from DNS1 with the jet centerline (JC) forcing, in comparison with homogeneous isotropic turbulence (HIT) at the same $Re_\lambda$ in $xy$ and $yz$ planes. . . . .	21
2.2 Contours of the vorticity, $\omega_x$ and $\omega_y$ , from DNS1 with the jet centerline (JC) forcing, in comparison with homogeneous isotropic turbulence (HIT) at the same $Re_\lambda$ in $xy$ and $yz$ planes. . . . .	22
2.3 Temporal fluctuations of turbulent parameters: (a) ratio of the integral length scale, $l$ , to the domain width, $L_x$ ; (b) anisotropy $\langle u_x^{*2} \rangle / \langle \mathbf{u}^{*2} \rangle$ ; (c) the volume-averaged kinetic energy, $\langle k^* \rangle$ , with respect to the expected value, $k_o$ ; (d) the volume-averaged dissipation rate, $\langle \varepsilon^* \rangle$ , with respect to the expected value, $\varepsilon_o$ . The parameters are plotted as a function of the time normalized by the a priori eddy time scale, $\tau_o$ . . . . .	24
2.4 Normalized vorticity as a function of $Re_\lambda$ . . . . .	25
2.5 Energy budget comparison. Each term is normalized by $U_c^3 / r_{1/2}$ . The lines are experimental data from P&Lu [25], and the points are the estimated values from Eqs. (2.48)–(2.54). . . . .	28

2.6	Single point values comparison: (a) anisotropy $\frac{\overline{u_x'^2}}{\overline{u'^2}}$ ; (b) normalized kinetic energy $\frac{\overline{k}}{U_c^2}$ ; (c) normalized dissipation rate $\frac{\overline{\varepsilon}}{U_c^3/x_o}$ . Boersma(98) [32] and Boersma(04) [33] are DNS. P&Li [24], P&Lu [25], Antonia [26], Romano [27], Xu [28], W&F [29], Burattini [30], and Darisse [31] are experiments. . . . .	31
2.7	Examination of the origins of the forcing term: (a) anisotropy $\frac{\langle u_x^{*2} \rangle}{\langle u^{*2} \rangle}$ ; (b) normalized kinetic energy $\frac{\langle k^* \rangle}{U_c^2}$ . The parameters are plotted as a function of the time normalized by the a priori eddy time scale, $\tau_o$ . <i>All</i> (black) refers to the original forcing term; <i>Mean</i> (blue), the forcing term from $\nabla \overline{u}$ only; <i>Mean+Adv</i> (red), the forcing term from $\nabla \overline{u}$ and advection normalization. . . . .	32
2.8	Comparison of normalized kinetic energy spectra in the longitudinal direction. Kolmogorov velocity scale, $u_k = (\nu\varepsilon)^{1/4}$ , is used for normalization. . . . .	33
2.9	Comparison of $E_i$ for JC and HIT. . . . .	34
3.1	Scaling coefficients for the variance (a, Eq. (3.15)), the scalar flux (b, Eq. (3.16)), and the dissipation rate (c, Eq. (3.17)) from SCL1-5. The dashed lines are weighted least-squares fits of a functional form $h(\text{Re}_\lambda) = a_1 - a_2 \exp(-a_3 \text{Re}_\lambda)$ . . . . .	45
3.2	Contours of scalar fields from SCL2 in xy (top) and yz (bottom) planes with three different forcing methods: the linear scalar (LS) forcing (left), the jet centerline (JC) forcing (middle), and the mean gradient (MG) forcing (right). . . . .	46
3.3	Normalized scalar flux $\frac{\langle\langle u_x^* C^* \rangle\rangle}{\sqrt{\langle\langle u_x^{*2} \rangle\rangle \langle\langle C^{*2} \rangle\rangle}}$ and its corresponding experimental quantity. Round jet experiments used for the comparison are summarized in Table 3.3. The figure displays SCL1-5 results with the original jet centerline (JC) terms, $\frac{U_c}{x_o} C^* + \frac{C_c}{x_o} u_x^*$ (red triangles); with only the linear scalar (LS) term, $\frac{U_c}{x_o} C^*$ (black triangles); and with only the mean gradient (MG) term, $\frac{C_c}{x_o} u_x^*$ (blue triangles). The mean of SCL1-5 values with the original forcing terms is 0.52, shown as the dashed red line. . . . .	48

3.4	Scalar energy spectrum: $\phi_c(\kappa_1)$ computed from SCL5 at $\text{Re}_\lambda = 129$ , and its least-squares fit result with model spectrum, Eq. (3.25). . . . .	49
3.5	Scaling exponent $n$ for the scalar energy spectra, $\phi_c \sim \kappa^{-n}$ , calculated from SCL1-6. Experiments used for the comparison are summarized in Table 3.5. The dashed line is a weighted least-squares fit of an exponential function, using all the presented data. The dash-dot line shows $n = 5/3$ . . . . .	51
3.6	Time scale ratio $r_\chi$ (Eq. (3.28)) from SCL1-5, Iso1-2, and Mag1-2. The mean of SCL1-5 values is shown as the dashed red line. . . . .	54
3.7	Normalized scalar flux from SCL1-5, Iso1-2, and Mag1-2. The mean of SCL1-5 values is shown as the dashed red line. . . . .	55
3.8	Volume-averaged ratio, $2 \frac{U_c \langle k \rangle}{x_o \langle \varepsilon \rangle}$ , from SCL1, Iso1-2, and Mag1-2, plotted as a function of the time normalized by the eddy time scale, $\tau_o = k_o/\varepsilon_o$ . The horizontal dashed line indicates the time-averaged value of each simulation. . . . .	55
4.1	A schematic diagram of a scalar energy spectrum, $\phi_c(\kappa)$ , and a kinetic energy spectrum, $\phi_k(\kappa)$ , in log-log scales. . . . .	59
4.2	Contours of scalar fields in $xy$ (top) and $yz$ (bottom) planes with $\text{Sc} = 1$ and $\text{Sc} = 16$ . . . . .	62
4.3	Scaling coefficients for the variance ( $\alpha_1$ , Eq. (3.15)), the scalar flux ( $\alpha_2$ , Eq. (3.16)), and the dissipation rate ( $\alpha_3$ , Eq. (3.17)) from SCH1-8, plotted as a function of $\text{Re}_\lambda$ (left) and as a function of $\text{Sc}$ (right). The dashed lines are the mean values for $\text{Sc} = 1$ . . . . .	64
4.4	Comparison of numerical and experimental normalized scalar flux as a function of $\text{Re}_\lambda$ for different Schmidt numbers. Round jet experiments with $\text{Sc} \approx 1$ are Anderson & Bremhorst [71], Darisse <i>et al.</i> [31], and Chevray & Tutu [74], from low to high Reynolds numbers. Round jet experiments with $\text{Sc} \gg 1$ are Webster <i>et al.</i> [59] and Antoine <i>et al.</i> [75], from low to high Reynolds numbers. A detailed summary is shown in Table 3.3. The figure displays SCL2,3,5 and SCH1-9 results. The mean of SCL2,3,5 values is shown as the red dashed line. . . . .	65
4.5	Normalized scalar flux as a function of $\text{Sc}$ . The figure displays SCL2,3,5 and SCH1-9 results. The dashed lines for $\text{Re}_\lambda = 51$ and $81$ are weighted least-squares fits of a functional form $q(\text{Sc}) = a_1 + a_2 \exp(-a_3 \text{Sc})$ . The red dashed line is the mean of $\text{Re}_\lambda = 129$ values. . . . .	66

4.6	The mean of normalized scalar flux values for $Re_\lambda = 129$ , and extrapolated high Schmidt number limits for $Re_\lambda = 51$ and $81$ from Fig. 4.5 are plotted in Fig. 4.7 as simulation data (black circles). . . .	67
4.7	Comparison of extrapolated high Schmidt number limits of numerical normalized scalar flux for $Re_\lambda = 51$ and $81$ , the mean value for $Re_\lambda = 129$ , and their corresponding experimental quantity as a function of $Re_\lambda$ . Round jet experiments with $Sc \gg 1$ are Webster <i>et al.</i> [59] ( $Re_\lambda = 71$ ) and Antoine <i>et al.</i> [75] ( $Re_\lambda = 130$ ), from low to high Reynolds numbers. A detailed summary of the experiments is shown in Table 3.3. . . . .	67
4.8	Scalar energy spectrum: $\phi_c(\kappa_1)$ computed from SCH6 at $Sc = 16$ , $Re_\lambda = 51$ , and its least-squares fit result with model spectrum, Eq. (4.11). The velocity spectrum $\phi_k(\kappa_1)$ from SCH6 has been computed and divided by $10^{3.5}$ to show the comparison. . . . .	68
4.9	Scaling exponent $n$ for the scalar energy spectra, $\phi \sim \kappa^{-n}$ , calculated from SCL2,3,5 and SCH1-9. Experimental values are taken from round jets with $Sc = 1900$ [92]. The dashed line is an exponential fitting using the three high $Sc$ simulation data and all of the experimental values. The dash-dot line shows $n = 5/3$ . . . . .	69
4.10	Scaling exponent $n$ as a function of $Sc$ . The figure displays SCL2,3,5 and SCH1-9 results. The dashed lines for $Re_\lambda = 51$ and $81$ are weighted least-squares fits of a functional form $q(Sc) = a_1 + a_2 \exp(-a_3 Sc)$ . 71	
A.1	Volume-averaged scalar flux, $\langle u_x^* C^* \rangle$ , from SCL2 plotted as a function of the time normalized by the eddy time scale, $\tau_o$ . The horizontal dashed line indicates its time-averaged value. . . . .	78
A.2	Averaging error $\hat{\delta}^2$ as a function of $n$ , for $\langle u_x^* C^* \rangle$ data presented in Fig. A.1. The solid line represents the least-squares fit result with $\hat{\delta}^2$ for $n \geq 920$ : $\hat{\delta}^2 = 0.00309/n - 0.911/n^2$ . . . . .	79
A.3	$f(N; \mathbf{B} _{n_k})$ from Eq. (A.10) is computed as a function of $n_k$ . . . . .	79
B.1	Temporal fluctuations of anisotropy $\langle u_x^{*2} \rangle / \langle u^{*2} \rangle$ as a function of the time normalized by the eddy time scale, $\tau_o$ . The time-averaged value for each curve is indicated as a dashed-line. . . . .	82
B.2	Temporal fluctuations of normalized scalar flux $\langle u_x^* C^* \rangle / \sqrt{\langle u_x^{*2} \rangle \langle C^{*2} \rangle}$ as a function of time normalized by the eddy time scale, $\tau_o$ . The time-averaged value for each curve is indicated as a dashed-line. . . . .	83

C.1	Staggering in space and time. Velocity components are stored at cell faces, and all scalar quantities are stored at cell centers. . . . .	85
-----	---	----

## LIST OF TABLES

<i>Number</i>	<i>Page</i>
1.1 $Re_D$ from turbulent round jet DNS and experiments. . . . .	6
2.1 Sources of the forcing term . . . . .	16
2.2 Relevant parameters of the target experiments and the corresponding simulations . . . . .	20
2.3 Mean values and standard deviations ( $Mean \pm SD$ ) of turbulent parameters over the statistically stationary region . . . . .	25
2.4 Round jet experiments and DNS used for the comparison. . . . .	30
2.5 Examination of the origins of the forcing term: time-averaged values of turbulent parameters. For our study, $\frac{\langle\langle u_x^{*2} \rangle\rangle}{\langle\langle \mathbf{u}^{*2} \rangle\rangle}$ and $\frac{\langle\langle k^* \rangle\rangle}{U_c^2}$ are used.	
For experiments, $\frac{\overline{u_x'^2}}{\mathbf{u}'^2}$ and $\frac{\overline{k}}{U_c^2}$ are used. . . . .	32
2.6 Least-squares fit results. . . . .	34
3.1 Inputs and outputs of DNS . . . . .	42
3.2 Relevant parameters of the target experiments and the corresponding simulations . . . . .	44
3.3 Round jet experiments used for the scalar flux comparison. . . . .	48
3.4 Least-squares fit results. . . . .	50
3.5 Experiments used for the energy spectrum comparison. . . . .	50
3.6 Forcing coefficients for the linear velocity forcing terms for simulations with $A = U_c/2x_0$ . . . . .	52
4.1 Relevant parameters of the target experiments and the corresponding simulations . . . . .	61
4.2 Least-squares fit results. . . . .	70
B.1 Relevant parameters of simulations for resolution test . . . . .	81

*Chapter 1*

## INTRODUCTION

Turbulence, by nature, loses its energy and decays over time, if there is no external force to prevent it from decaying. In practical flows, turbulence is generated by the strong kinetic energy of fluids. In some simulations, however, an artificial numerical technique is employed to sustain turbulence. For example, it is used when studying the nature of turbulent flames [1–3]. Turbulence forcing is a great tool when developing and testing subgrid models [4, 5] for large-eddy simulations (LES) [6, 7]. It is often applied in a triply periodic box with a zero mean flow to conveniently study turbulence and scalar mixing processes in a simple geometry [8–17]. An example of such simulations is shown in Fig. 1.1. If the forcing methods preserve turbulent properties of practical flows, they can be a great help in studying turbulence because the computational cost can be reduced to a great extent, and data can be easily computed and gathered.

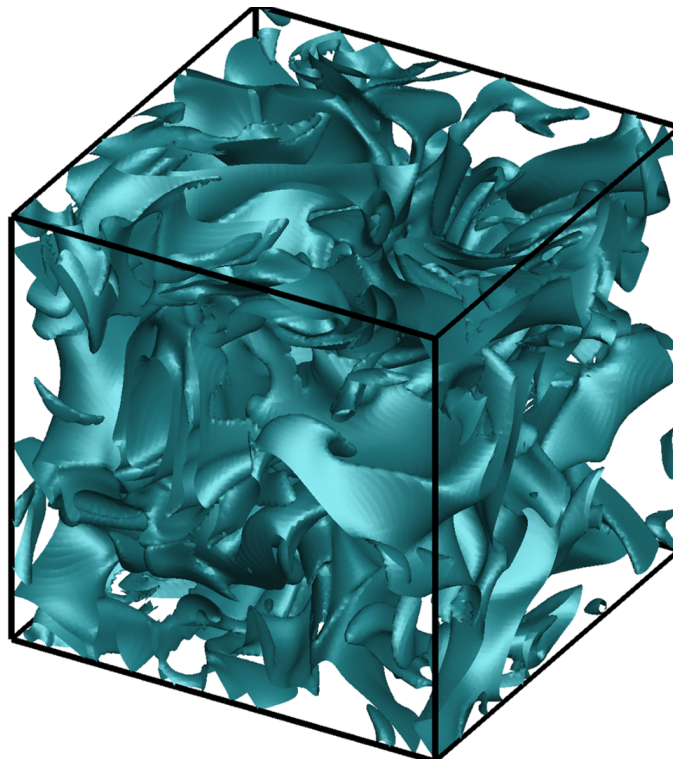


Figure 1.1: Isosurface of an instantaneous scalar field in a three-dimensional turbulent box simulation.

There have been previous forcing methods that successfully generate turbulence by numerically maintaining the variance of velocity or scalar fluctuations at a certain value [4–8, 18–23]. However, they were not developed to produce turbulence that resembles that of a practical flow. In this section, we will introduce what differences there are between practical flows and the flows produced by previous forcing methods.

## 1.1 Anisotropy

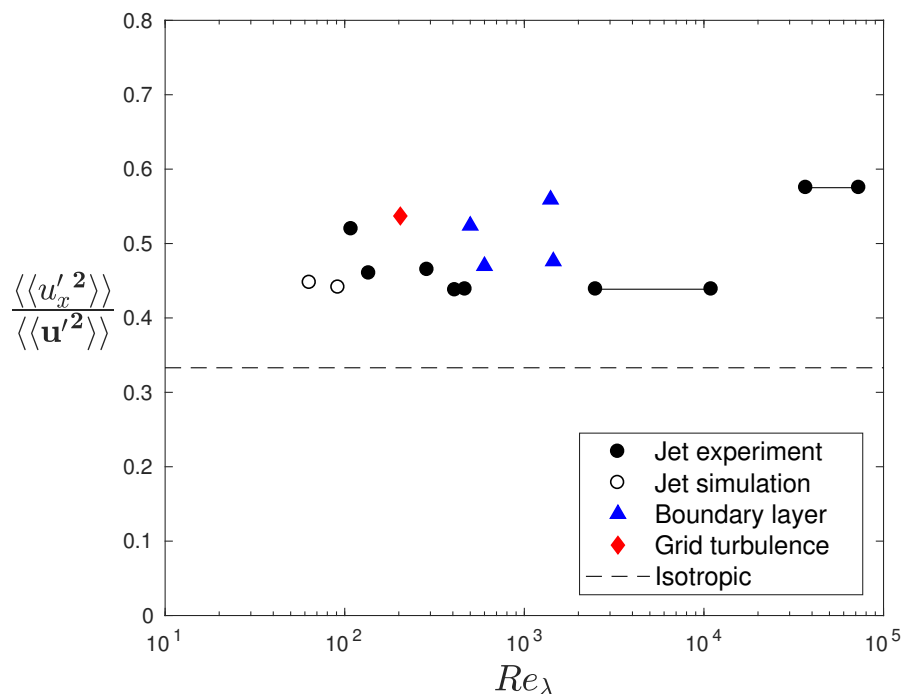


Figure 1.2: Anisotropy ratio  $\frac{\langle\langle u_x'^2 \rangle\rangle}{\langle\langle \mathbf{u}'^2 \rangle\rangle}$  from turbulent round jet experiments [24–31], jet DNS [32, 33], boundary layer [34], and grid turbulence [35], as a function of  $Re_\lambda$ .

Numerical simulations with a forcing scheme are often performed in spectral space with triply periodic boundary conditions. Many of these forcing schemes were designed to inject energy at low wavenumbers in spectral computations, such that the energy cascades down to high wavenumbers [4–7, 18–20]. These methods are explained in more detail in Sec. 2.1. It should be noted that all of these methods force the flows isotropically. While Lundgren’s linear forcing scheme [21] is applied in physical space, it is also invariant with respect to direction. Practical flows, however, are rarely isotropic.

One simple way to measure anisotropy is to calculate  $\frac{\langle\langle u_x'^2 \rangle\rangle}{\langle\langle \mathbf{u}'^2 \rangle\rangle}$ , where  $u_x'$  is the velocity fluctuation in the longitudinal direction, and  $\langle\langle \cdot \rangle\rangle$  denotes time-averaging of volume-averaged values. Also,  $\mathbf{u}'^2$  denotes  $\mathbf{u}' \cdot \mathbf{u}'$ . Figure 1.2 shows the anisotropy values from turbulent round jet experiments [24–31], jet DNS [32, 33], boundary layer [34], and grid turbulence [35], as a function of  $\text{Re}_\lambda$ . If the flow is isotropic, the ratio  $\frac{\langle\langle u_x'^2 \rangle\rangle}{\langle\langle \mathbf{u}'^2 \rangle\rangle}$  is exactly 1/3, as indicated by a dashed line. However, all the other various turbulent flows listed here are between 0.4 and 0.6.

All atmospheric and oceanic flows are also anisotropic, due to the rotation of planets [36, 37]. Other experiments on turbulent flows also found that there exist some degrees of anisotropy at all scales [34, 35, 38–40].

The concept of isotropy has been very useful in deriving important theories like the Kármán-Howarth equation [41] or Kolmogorov’s 4/5 law [42]. This approximation is a great tool, because it considerably simplifies the fluid mechanics theories. A true isotropy means that all the turbulent properties of velocity fields are statistically invariant to any rotation. As mentioned above, however, it is difficult to find real flows that are truly isotropic.

When we apply artificial forcing to create turbulent environments, we want the turbulence to be similar to that of real flows, even if the computation geometry is a triply periodic box. However, all the previous forcing schemes generate statistically isotropic turbulence. These observations clearly motivate the need for a more realistic forcing scheme.

## 1.2 Scaling of energy spectrum

The energy spectrum,  $\phi(\kappa)$ , is defined as:

$$\int \phi(\kappa) d\kappa = \overline{k}, \quad (1.1)$$

where  $\kappa$  is the wavenumber,  $k = \frac{1}{2} \mathbf{u}'^2$  is the kinetic energy, and the overline  $\overline{\cdot}$  denotes ensemble-averaging. Also,  $\phi(\kappa)$  can be computed by applying a Fourier transform on the auto-correlation function. Energy spectra are often used as a simple way to characterize turbulence. A schematic diagram of an energy spectrum is shown in Fig. 1.3.

A typical energy spectrum consists of a few different subranges. Figure 1.3 shows the inertial and dissipative subranges. In the inertial region, the energy cascades

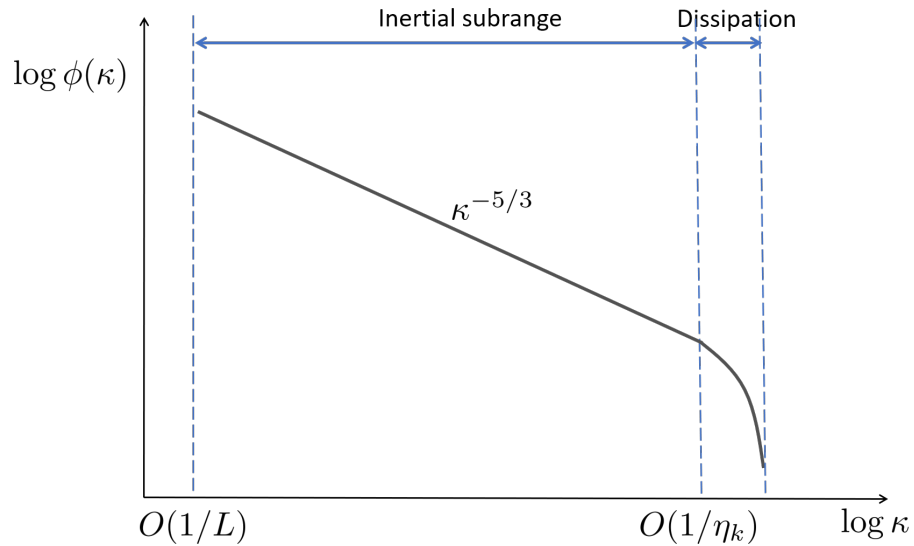


Figure 1.3: A schematic diagram of an energy spectrum,  $\phi(\kappa)$ , in log-log scales.

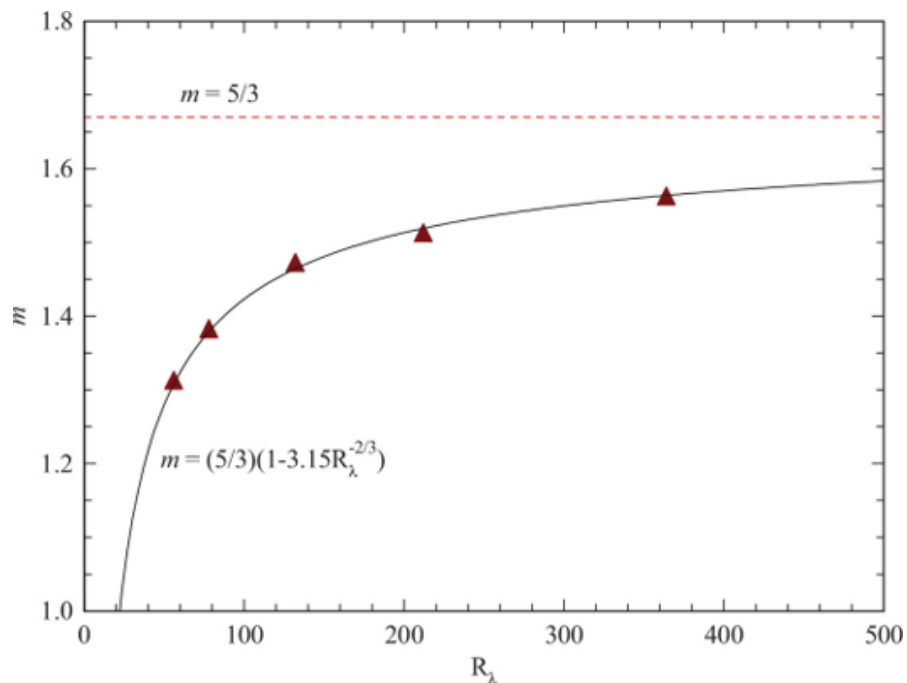


Figure 1.4: Scaling exponent  $m$  for energy spectra,  $\phi \sim \kappa^{-m}$ , computed from turbulent jet experiments. The solid line is a fit found by Mydlarski and Warhaft [43] by using wind tunnel experiments. The dashed line shows  $m = 5/3$ . Reprinted from [44], with the permission of AIP Publishing.

down from large scales to small scales, and in the dissipative region, the viscous friction dissipates the energy. Kolmogorov's theory predicts that  $\phi \sim \kappa^{-5/3}$  in the inertial range at very high Reynolds numbers [42].

In lower Reynolds number flows, however, the scaling exponent  $n$ , as in  $\phi \sim \kappa^{-n}$  in the inertial subrange, can differ from  $5/3$ . Mydlarski and Warhaft [43] found that  $n$  increases as a function of the Reynolds number toward  $n = 5/3$  by using grid turbulence data from wind tunnel experiments. Xu *et al.* [44] observed that  $n$  computed from turbulent jet experiments increases in a similar manner, as shown in Fig. 1.4, as a function of the Taylor-microscale Reynolds number,  $Re_\lambda$ .

Even though it is clear that the scaling slope is less than  $5/3$  for  $Re_\lambda < 500$ , previous forcing schemes seem to produce velocity fields with  $n = 5/3$  regardless of the Reynolds number [5, 7, 20], with the exception of Lundgren’s isotropic linear forcing in physical space [21]. Realistic forcing schemes must generate energy spectra whose scaling exponent is smaller than  $5/3$ .

### 1.3 Computational cost

Direct numerical simulations (DNS) are capable of providing detailed information about velocity or scalar fields as they resolve the smallest length scales, such as the Kolmogorov length scale  $\eta_k$  or the Batchelor length scale  $\eta_B$ . However, the high computational cost of DNS has always been problematic; typically, DNS is limited to low Reynolds numbers. Experiments, on the other hand, can be conducted at high Reynolds numbers, but practical difficulties in measurements make it hard to obtain detailed information on velocity and scalar fields.

For instance, DNS of turbulent round jets have been studied for decades, but their computational cost is still too expensive to reach the high Reynolds numbers of experiments. Table 1.1 reviews some DNS and experiments found in the literature, and their jet Reynolds numbers,  $Re_D = U_o D / \nu$ , based on the exit nozzle velocity,  $U_o$ , and the nozzle diameter,  $D$ .

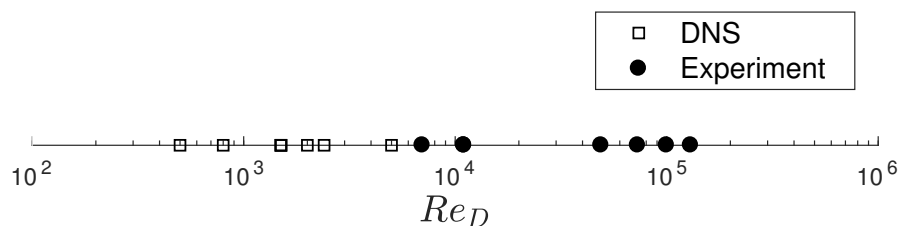


Figure 1.5:  $Re_D$  from turbulent round jet DNS and experiments in log scale, listed in Table 1.1.

Table 1.1:  $Re_D$  from turbulent round jet DNS and experiments.

	Author	$Re_D$
DNS	Gohil <i>et al.</i> [45]	500 – 2000
	Freund & Moin [46]	800
	Tsujimoto <i>et al.</i> [47]	1500
	Lardeau <i>et al.</i> [48]	1500
	Boersma <i>et al.</i> [32]	2400
	Boersma [33]	5000
Experiment	Papanicolaou & List [24]	7000
	Panchapakesan & Lumley [25]	11000
	Xu & Antonia [28]	37000 – 73000
	Romano & Antonia [27]	49000
	Wynanski & Fiedler [29]	100000
	Burattini <i>et al.</i> [30]	130000
	Darisse <i>et al.</i> [31]	140000

Figure 1.5 displays  $Re_D$  of turbulent round jet DNS and experiments in log scale. For the cases shown here, DNS are mostly conducted at low  $Re_D$  and experiments are at high  $Re_D$ .

We can help resolve this issue, if we derive forcing schemes that can generate the turbulence of round jets in a triply periodic box. The cost of the computations will be reduced because we do not need to simulate the entire jet. Furthermore, the simple geometry and boundary conditions will make it easy to conduct computations and calculate the desired data. However, while previously existing forcing schemes successfully injected velocity energy, they did not produce turbulence of a practical flow, as discussed in Sec. 1.1 and 1.2. Thus, a novel forcing method will be a great tool to study practical flows.

#### 1.4 Objectives and outline

The motivation for the current study is the need to find a realistic forcing scheme that produces turbulence of a practical flow, as opposed to the previous arbitrary ones. Any turbulent flow can be chosen as the target practical flow. In this investigation, however, we aim to reproduce the turbulence (both velocities and passive scalars) in the centerline region of fully-developed turbulent round jets. More specifically, the goal of this thesis is to derive velocity and scalar forcing terms that generate the local velocity and scalar fields of axisymmetric jets on the centerline.

1. Derive a velocity forcing term from the Navier-Stokes equations by using

- mean velocity profiles of round jets;
2. Perform numerical simulations of turbulent velocity fields by applying the derived velocity forcing term in a triply periodic box; compute turbulent properties from the resulting velocity fields; and validate the results against experimental measurements;
  3. Derive a scalar forcing term from the scalar transport equation by using mean velocity and scalar profiles of round jets;
  4. Perform numerical simulations of velocity and passive scalar fields with unity Schmidt number by applying the derived velocity and scalar forcing terms in a triply periodic box; compute mixing properties from the resulting velocity and scalar fields; and validate the results against experimental measurements;
  5. Repeat #4 with higher Schmidt numbers.

The objectives #1 and #2 are fulfilled in Ch. [2](#); #3 and #4 in Ch. [3](#); and #5 in Ch. [4](#).

## *Chapter 2*

### VELOCITY FORCING SCHEME TO REPRODUCE THE TURBULENT CHARACTERISTICS OF ROUND JETS ON THE CENTERLINE

Chapter 2 has been adapted from:

- [49] Kyupaeck Jeff Rah, Chandru Dhandapani, and Guillaume Blanquart. Derivation of a realistic forcing term to reproduce the turbulent characteristics of round jets on the centerline. *Physical Review Fluids* 3(8):084606, 2018. DOI: [10.1103/PhysRevFluids.3.084606](https://doi.org/10.1103/PhysRevFluids.3.084606).

Turbulence forcing techniques are often required in the numerical simulation of statistically stationary turbulent flows. However, the existing forcing techniques are not based on physics, but rather arbitrary numerical methods that sustain the turbulent kinetic energy. In this work, a novel forcing technique is devised to reproduce the centerline turbulent characteristics of round jets in a triply periodic box. It is derived from the Navier-Stokes equations by applying a Reynolds decomposition with the mean velocity of the axisymmetric jet. The result is an anisotropic linear forcing term, which is intended to be used in a 3D box to create turbulence. Four direct numerical simulations with different  $Re_\lambda$  have been performed with the new forcing terms. The budget of the terms in the kinetic energy equation is very close to the experimental measurement on the centerline. The anisotropy, kinetic energy  $k$ , and dissipation rate  $\varepsilon$  of the simulations are also comparable to experimental values. Finally, the kinetic energy spectrum in the axial direction,  $\phi(\kappa_1)$ , is presented. With appropriate normalizations, the spectrum agrees well with the round jet spectrum on its centerline.

#### **2.1 Previous velocity forcing methods**

In numerical simulations, stationary turbulence is often required to obtain meaningful statistics. For instance, it is needed in the simulations of turbulent flows and scalar mixing processes in a triply periodic box [4–7, 18, 22, 50]. It can also be desired in geometries other than triply periodic box; for example, Savard *et al.* [1], Poludnenko and Oran [2], and Hamlington *et al.* [3] needed statistically stationary

turbulence when examining turbulent flames. In these cases, an artificial forcing scheme must be used to prevent the turbulence from decaying.

Traditional forcing schemes have been implemented in spectral space. Below is the Fourier-transformed incompressible momentum equation.

$$\frac{\partial \widehat{\mathbf{u}}}{\partial t} + \widehat{\mathbf{u} \cdot \nabla \mathbf{u}} = -\frac{1}{\rho} \widehat{\nabla p} + \nu \widehat{\nabla^2 \mathbf{u}} + \widehat{\mathbf{f}}_u, \quad (2.1)$$

where  $\mathbf{u}$  is the velocity;  $\rho$ , density;  $p$ , pressure; and  $\nu$ , kinematic viscosity. The operator  $\widehat{\cdot}$  denotes a Fourier transformation.  $\mathbf{f}_u$  is the forcing term that prevents the turbulence from decaying. In the literature, mainly three categories of forcing schemes can be found.

In the first category, a forcing term  $\widehat{\mathbf{f}}_u(\boldsymbol{\kappa}, t) = c_u(\boldsymbol{\kappa}, t)\widehat{\mathbf{u}}(\boldsymbol{\kappa}, t)$  is used for certain chosen wavenumber shells. For example, Ghosal *et al.* [6] and Carati *et al.* [4] applied the following forcing to all the modes in the wavenumber shell  $|\boldsymbol{\kappa}| \leq \kappa_f$ :

$$\widehat{\mathbf{f}}_u(\boldsymbol{\kappa}, t) = \varepsilon \frac{\widehat{\mathbf{u}}(\boldsymbol{\kappa}, t)}{N|\widehat{\mathbf{u}}(\boldsymbol{\kappa}, t)|^2}, \quad (2.2)$$

where  $\varepsilon$  is the average dissipation rate,  $N$  is the number of modes in the wavenumber shell, and  $\kappa_f$  is the maximum wavenumber subjected to forcing. Both simulations of Ghosal and Carati used  $\kappa_f = 2\kappa_{min}$ , where  $\kappa_{min}$  is the minimum wavenumber determined by the domain size.

The second class of schemes maintains the energy of certain wavenumber shells at a constant level for all time steps. For instance, Chasnov [5] and Sullivan *et al.* [18] kept the energy constant in the wavenumber shell  $|\boldsymbol{\kappa}| \leq \kappa_f$ . Chasnov used  $\kappa_f = 2\kappa_{min}$  and Sullivan used  $\kappa_f = 2\sqrt{2}\kappa_{min}$ . This method assumes that the higher wavenumber flow structure should not be changed much, and that the energy should pass down to the smaller scales. Seror *et al.* [7] maintained the total kinetic energy at a constant level by injecting the lost energy into the wavenumbers at  $|\boldsymbol{\kappa}| \leq 5\kappa_{min}$  for each time step. This was achieved by forcing

$$\widehat{\mathbf{u}}^{n+1}(\boldsymbol{\kappa}) = \sqrt{1 + \frac{\Delta E}{\int_{\kappa_{min}}^{\kappa_{max}} E(\boldsymbol{\kappa}) d\boldsymbol{\kappa}}}} \widehat{\mathbf{u}}^*(\boldsymbol{\kappa}), \quad (2.3)$$

where  $\widehat{\mathbf{u}}^{n+1}(\boldsymbol{\kappa})$  is the Fourier coefficient at time  $(n+1)\Delta t$  for  $|\boldsymbol{\kappa}| \leq 5\kappa_{min}$ , and  $\widehat{\mathbf{u}}^*(\boldsymbol{\kappa})$  is the Fourier coefficient computed by integrating the Navier-Stokes equation with  $\widehat{\mathbf{u}}^n(\boldsymbol{\kappa})$  as an initial condition.  $\Delta E$  is the lost energy, and  $\kappa_{max} = 5\kappa_{min}$ .

Stochastic schemes have also been devised for the forcing term. Eswaran and Pope [19] developed the following expression:

$$\widehat{\mathbf{f}}_u(\boldsymbol{\kappa}, t) = \widehat{\mathbf{b}}_u(\boldsymbol{\kappa}, t) - \frac{\boldsymbol{\kappa} \left( \boldsymbol{\kappa} \cdot \widehat{\mathbf{b}}_u(\boldsymbol{\kappa}, t) \right)}{\boldsymbol{\kappa} \cdot \boldsymbol{\kappa}}, \quad (2.4)$$

where  $\widehat{\mathbf{b}}_u$  is a complex vector-valued stochastic process based on Uhlenbeck-Ornstein random process [51]. This expression is the projection of the stochastic process onto the plane normal to  $\boldsymbol{\kappa}$ . The forcing term is only applied for  $|\boldsymbol{\kappa}| \leq \kappa_f$ . Two values of  $\kappa_f$ ,  $\sqrt{2}\kappa_{min}$  and  $2\sqrt{2}\kappa_{min}$ , were tested for the simulations of Eswaran and Pope. Alvelius [20] also formulated a random force:

$$\widehat{\mathbf{f}}_u(\boldsymbol{\kappa}, t) = A_{ran}(\boldsymbol{\kappa}, t)e_1(\boldsymbol{\kappa}) + B_{ran}(\boldsymbol{\kappa}, t)e_2(\boldsymbol{\kappa}), \quad (2.5)$$

where  $e_1$  and  $e_2$  are unit vectors orthogonal to each other and to  $\boldsymbol{\kappa}$ , and  $A_{ran}$  and  $B_{ran}$  are random complex numbers determined by the prescribed force spectrum.

As shown above, there have been various forcing methods in spectral space to create statistically stationary turbulence. However, these spectral forcing schemes are not applicable to non-periodic boundary condition cases, and it is difficult to implement in numerical simulations based on the momentum equations in physical space. Furthermore, these methods are not developed to represent any practical flows. They sustain the turbulent energy of velocity fields, yet they are rather arbitrary numerical methods.

The objective of the current study is to develop a forcing scheme to produce a turbulent flow whose characteristics resemble those of a practical flow. Any turbulent flow can be chosen as a target. In this investigation, however, we aim to reproduce the turbulence in the centerline region of fully-developed turbulent round jets. In other words, the purpose is to imitate the local turbulent characteristics of axisymmetric jets at  $r = 0$ . It is not our goal to derive a source term for the entire region of a round jet.

## 2.2 Review of Lundgren's linear forcing term and motivation

The linear forcing scheme, suggested by Lundgren [21] and further explored by Rosales and Meneveau [52], is different from the other spectral schemes. The essential difference, as described at the end of Sec. 2.1, is that the forcing term is applied in physical space instead of in spectral space. Since the forcing term of the current study takes a similar form, this linear method is reviewed in detail first.

Let's consider the Reynolds decomposition,  $\mathbf{u} = \bar{\mathbf{u}} + \mathbf{u}'$ , where  $\bar{\mathbf{u}}$  is the mean velocity, and  $\mathbf{u}'$  is the fluctuating velocity. The momentum equation for the velocity fluctuation can be obtained from the original Navier-Stokes equation after subtracting the mean of the equation:

$$NS(\bar{\mathbf{u}} + \mathbf{u}') - \overline{NS(\bar{\mathbf{u}} + \mathbf{u}')}. \quad (2.6)$$

This gives

$$\begin{aligned} & \frac{\partial \mathbf{u}'}{\partial t} + \bar{\mathbf{u}} \cdot \nabla \mathbf{u}' + \mathbf{u}' \cdot \nabla \bar{\mathbf{u}} + \mathbf{u}' \cdot \nabla \mathbf{u}' - \nabla \cdot \overline{\mathbf{u}' \mathbf{u}'} \\ & = -\frac{1}{\rho} \nabla p' + \nu \nabla^2 \mathbf{u}', \end{aligned} \quad (2.7)$$

where  $NS$  is the set of Navier-Stokes equations, and  $p'$  is the pressure fluctuation. The overline  $\overline{\quad}$  denotes ensemble-averaging.

The third term,  $\mathbf{u}' \cdot \nabla \bar{\mathbf{u}}$ , appears as an energy production term in the kinetic energy equation. Lundgren argued that since this production term is proportional to  $\mathbf{u}'$ , a source term in physical space should have the following form:

$$\mathbf{f}_u = A \mathbf{u}', \quad (2.8)$$

where  $A$  is an arbitrary constant. Then, the resultant momentum equation is

$$\frac{\partial \mathbf{u}'}{\partial t} + \mathbf{u}' \cdot \nabla \mathbf{u}' = -\frac{1}{\rho} \nabla p' + \nu \nabla^2 \mathbf{u}' + A \mathbf{u}'. \quad (2.9)$$

This isotropic source term provides a continuous energy injection at all scales, maintaining the turbulence at a statistically stationary state.

The kinetic energy equation can be derived by multiplying  $\mathbf{u}'$  to equation (2.9):

$$\frac{\partial k}{\partial t} + \mathbf{u}' \cdot \nabla k = -\frac{1}{\rho} \nabla \cdot \mathbf{u}' p' + \nu \nabla^2 k - \varepsilon + 2Ak, \quad (2.10)$$

where  $k = \frac{1}{2} \mathbf{u}' \cdot \mathbf{u}'$  is the kinetic energy,  $\varepsilon = 2\nu S_{ij} S_{ij}$  is the energy dissipation rate, and  $S_{ij} = \frac{1}{2} \left( \frac{\partial u'_i}{\partial x_j} + \frac{\partial u'_j}{\partial x_i} \right)$  is the strain-rate tensor. Since time and spatial derivatives of ensemble-averaged quantities are zero for statistically stationary homogeneous flows, the following relation can be derived:

$$0 = -\bar{\varepsilon} + 2A\bar{k}. \quad (2.11)$$

Then, it follows that  $A$  determines the ratio of the average turbulent kinetic energy to the average energy dissipation rate for statistically stationary turbulence; i.e.,

$$A = \frac{\overline{\varepsilon}}{2k}. \quad (2.12)$$

Lundgren examined one term in Eq. (2.7), and proposed a generic expression,  $f_u = Au'$ , for the forcing term in Eq. (2.8). However, all the terms in Eq. (2.7) could be examined by using mean velocity information of practical turbulent flows.

### 2.3 Proposed forcing term

The new forcing term is meant to replicate the turbulent characteristics of round jets in a triply periodic cubic box, in which the flow is statistically homogeneous with zero mean velocity. A periodic geometry is convenient to compute statistics and perform spectral analyses.

#### 2.3.1 Review of turbulent jets

A typical turbulent jet consists of three zones: the potential core, the transition zone, and the fully-developed self-similar zone. The velocity in the self-similar zone can be expressed as a function of the centerline velocity,  $U_c$ , and the similarity variable,  $\eta = r/x$ , where  $r$  is the radial distance and  $x$  is the axial distance. It has been shown that  $U_c$  scales as  $1/x$  in the self-similar region by many experiments [25, 28, 30, 53, 54].

Abramovich [55] and Pope [53] used a stream function theory to describe the mean velocity of axisymmetric turbulent jets. The result is shown below:

$$\bar{u}_x = U_c \frac{F'_o(\eta)}{\eta}, \quad (2.13)$$

$$\bar{u}_r = U_c \left[ F'_o(\eta) - \frac{1}{\eta} F_o(\eta) \right], \quad (2.14)$$

where  $F_o(\eta)$  is a function to be determined. Abramovich and Pope used different expressions for  $F_o(\eta)$  to fit the experimental velocity profiles. However, the two expressions yield the same velocity gradient matrix, when evaluated at the centerline of a certain location  $x_o$ :

$$\nabla \bar{\mathbf{u}}(x = x_o, \eta = 0) = \begin{bmatrix} -\frac{U_c}{x_o} & 0 & 0 \\ 0 & \frac{1}{2} \frac{U_c}{x_o} & 0 \\ 0 & 0 & \frac{1}{2} \frac{U_c}{x_o} \end{bmatrix}. \quad (2.15)$$

In the self-similar region, the fluctuating velocity is also a function of the centerline velocity and the similarity variable only. More importantly,

$$\sqrt{\langle u_i'^2 \rangle} = U_c f_i(\eta), \quad (2.16)$$

as demonstrated by many experiments [25, 28, 30, 53, 54]. Thus,  $\sqrt{\langle u_i'^2 \rangle}/U_c$  must only be a function of  $\eta$ . The summation convention over repeated indices is not adopted here.

### 2.3.2 Derivation of the forcing term

Theoretically, Eq. (2.13)–(2.15) can be applied to Eq. (2.7), to remove the  $\bar{u}$  terms and obtain the momentum equation for the fluctuating velocities. However, the resulting turbulent flow would not be statistically homogeneous; indeed,  $\mathbf{u}'$  decreases as  $1/x$  in a turbulent jet. It is thus preferable to normalize first  $\mathbf{u}'$  with  $x/x_o$ . Then,

$$\mathbf{u}^* = \frac{x}{x_o} \mathbf{u}' = \frac{x}{x_o} (\mathbf{u} - \bar{\mathbf{u}}), \quad (2.17)$$

where  $\mathbf{u}$  is the original velocity of the jet, and the asterisk  $\cdot^*$  denotes the normalized quantity. With this normalization, the continuity equation, when evaluated at  $x = x_o$ , would have a non-zero term on the right hand side as below:

$$\nabla \cdot \mathbf{u}^* = \frac{u_x^*}{x_o}. \quad (2.18)$$

Although it is possible to perform a numerical simulation with an extra term in the continuity equation, it is preferred not to, for practical reasons. Thus, we propose the following normalization in lieu of Eq. (2.17):

$$\begin{aligned} u_x^* &= \frac{x}{x_o} (u_x - \bar{u}_x) \exp\left(1 - \frac{x}{x_o}\right) \\ u_i^* &= \frac{x}{x_o} (u_i - \bar{u}_i) \end{aligned} \quad (2.19)$$

$u_i$  denotes either of the transverse velocities.

Now, Eqs. (2.13)–(2.15), and (2.19) can be applied to Eq. (2.7). The terms are evaluated on the centerline at a certain location  $x_o$ , leading to the following equations:

- Continuity

$$\nabla \cdot \mathbf{u}^* = 0 \quad (2.20)$$

- Longitudinal direction

$$\begin{aligned} & \frac{Du_x^*}{Dt} + \mathbf{u}^* \cdot \nabla u_x^* + \frac{1}{\rho} \frac{\partial p}{\partial x} - \nu \nabla^2 u_x^* \\ &= \nabla \cdot \overline{\mathbf{u}^* u_x^*} + \nu \frac{u_x^*}{x_o^2} + \frac{U_c}{x_o} u_x^* \end{aligned} \quad (2.21)$$

- Transverse directions

$$\begin{aligned} & \frac{Du_i^*}{Dt} + \mathbf{u}^* \cdot \nabla u_i^* + \frac{1}{\rho} \frac{\partial p}{\partial x_i} - \nu \nabla^2 u_i^* \\ &= \nabla \cdot \overline{\mathbf{u}^* u_i^*} + \nu \left[ 2 \frac{u_i^*}{x_o^2} - \frac{2}{x_o} \frac{\partial u_i^*}{\partial x} \right] - \frac{\overline{u_x^* u_i^*}}{x_o} + \frac{u_x^* u_i^*}{x_o} + \frac{1}{2} \frac{U_c}{x_o} u_i^* \end{aligned} \quad (2.22)$$

The vector notation applies to all three directions, and  $u_i^*$  and  $x_i$  apply to either of the transverse directions. The material derivative is defined as  $\frac{D}{Dt} \equiv \frac{\partial}{\partial t} + U_c \frac{\partial}{\partial x}$ , which provides the effect of a Galilean transformation. This  $\frac{D}{Dt}$  will be used as the time derivative in the computations.

Several terms on the right-hand side (RHS) of Eq. (2.21) and (2.22) are negligible, as compared to the other terms. First,  $\nu u_i^*/x_o^2 \ll U_c u_i^*/x_o$  for high Reynolds number flows. In fact, the ratio  $U_c x_o/\nu$  is proportional to the jet Reynolds number  $Re_D = U_o D/\nu$ , based on the exit nozzle velocity,  $U_o$ , and the nozzle diameter,  $D$  [55]. Similarly,  $\frac{\nu}{x_o} \frac{\partial u_i^*}{\partial x} \ll \mathbf{u}^* \cdot \nabla u_i^*$ . The ratio of the two terms is of the same magnitude as the local turbulent Reynolds number. In addition,  $\nabla \cdot \overline{\mathbf{u}^* u_i^*}$  and  $\overline{u_x^* u_i^*}/x_o$  appear as  $\overline{u_i^* \nabla \cdot \mathbf{u}^* u_i^*}$  and  $\overline{u_i^* u_x^* u_i^*}/x_o$ , respectively, in the kinetic energy equation. They do not contribute to the mean kinetic energy, because  $\overline{u_i^*} \equiv 0$ .  $u_x^* u_i^*/x_o$ , on the other hand, appears as  $\overline{u_x^* u_i^{*2}}/x_o$  in the kinetic energy equation. The magnitude of  $\overline{u_x^* u_i^{*2}}/x_o$  can be compared to that of  $\frac{1}{2} \frac{U_c}{x_o} \overline{u_i^{*2}}$ . According to experiments [25, 31, 54], the value of  $\overline{u_x^* u_i^2}/U_c^3$  is 0.0010~0.0017, and that of  $\overline{u_i^2}/U_c^2$  is 0.036~0.050. Then, the ratio of  $\overline{u_x^* u_i^2}/x_o$  to  $\frac{1}{2} \frac{U_c}{x_o} \overline{u_i^2}$  ranges from 0.040 to 0.094. Although the governing equations are for the normalized quantities,  $u_i^*$ , we will assume here that turbulent parameters of  $u_i^*$  are comparable to those of  $u_i'$ . Thus, we will conclude that  $u_x^* u_i^*/x_o$  is also negligible. With these simplifications, the only terms significantly contributing to the production of kinetic energy are  $\frac{U_c}{x_o} u_x^*$  in Eq. (2.21) and  $\frac{1}{2} \frac{U_c}{x_o} u_i^*$  in Eq. (2.22). Thus, only these RHS terms in the momentum equations are retained; the other terms are removed.

The final governing equations for  $\mathbf{u}^*$  are as follows:

- Continuity

$$\nabla \cdot \mathbf{u}^* = 0, \quad (2.23)$$

- Longitudinal direction

$$\frac{Du_x^*}{Dt} + \mathbf{u}^* \cdot \nabla u_x^* + \frac{1}{\rho} \frac{\partial p}{\partial x} - \nu \nabla^2 u_x^* = \frac{U_c}{x_o} u_x^*, \quad (2.24)$$

- Transverse directions

$$\frac{Du_i^*}{Dt} + \mathbf{u}^* \cdot \nabla u_i^* + \frac{1}{\rho} \frac{\partial p}{\partial x_i} - \nu \nabla^2 u_i^* = \frac{1}{2} \frac{U_c}{x_o} u_i^*, \quad (2.25)$$

- Ensemble-averaged kinetic energy

$$0 = -\overline{\varepsilon^*} + \frac{U_c}{x_o} \overline{k^*} + \frac{\overline{u_x^{*2}}}{2}, \quad (2.26)$$

where  $\overline{\varepsilon^*} = 2\nu \overline{S_{ij}^* S_{ij}^*} = \nu \frac{\partial u_i^*}{\partial x_j} \frac{\partial u_i^*}{\partial x_j}$  is the energy dissipation rate, and  $S_{ij}^* = \frac{1}{2} \left( \frac{\partial u_i^*}{\partial x_j} + \frac{\partial u_j^*}{\partial x_i} \right)$

is the strain-rate tensor. It is important to note that the magnitude of the source terms is determined by two simple experimental parameters,  $U_c$  and  $x_o$ .

The sources of this forcing term are summarized below:

- Longitudinal direction

$$\begin{aligned} \text{Production :} \quad & -\mathbf{u}' \cdot \nabla \bar{u}_x \Big|_{x=x_o} = \frac{U_c}{x_o} \frac{x_o}{x} e^{\frac{x}{x_o}-1} u_x^* \Big|_{x=x_o} \\ & = \frac{U_c}{x_o} u_x^* \end{aligned} \quad (2.27)$$

$$\begin{aligned} \text{Advection :} \quad & -\bar{\mathbf{u}} \cdot \nabla u_x' \Big|_{x=x_o} = -U_c \frac{\partial}{\partial x} \left( \frac{x_o}{x} e^{\frac{x}{x_o}-1} u_x^* \right) \Big|_{x=x_o} \\ & = \frac{U_c}{x_o} u_x^* - \frac{U_c}{x_o} u_x^* - U_c \frac{\partial u_x^*}{\partial x} \end{aligned} \quad (2.28)$$

- Transverse directions

$$\begin{aligned} \text{Production :} \quad & -\mathbf{u}' \cdot \nabla \bar{u}_i \Big|_{x=x_o} = -\frac{1}{2} \frac{U_c}{x_o} \frac{x_o}{x} u_i^* \Big|_{x=x_o} \\ & = -\frac{1}{2} \frac{U_c}{x_o} u_i^* \end{aligned} \quad (2.29)$$

$$\begin{aligned} \text{Advection :} \quad & -\bar{\mathbf{u}} \cdot \nabla u_i' \Big|_{x=x_o} = -U_c \frac{\partial}{\partial x} \left( \frac{x_o}{x} u_i^* \right) \Big|_{x=x_o} \\ & = \frac{U_c}{x_o} u_i^* - U_c \frac{\partial u_i^*}{\partial x} \end{aligned} \quad (2.30)$$

The  $U_c \frac{\partial u_i^*}{\partial x}$  terms do not appear in the governing equations, as they are combined with  $\frac{\partial u_i^*}{\partial t}$  to make  $\frac{Du_i^*}{Dt}$ .

Essentially, the source term from *production* is generated by the gradient of the mean flow,  $\nabla \bar{\mathbf{u}}$ . The source term from *advection*, on the other hand, is generated by two normalizations,  $\frac{x_o}{x}$  and the exponential one. Since  $\mathbf{u}'$  decreases as the mean flow travels in  $x$ -direction, the  $\frac{x_o}{x}$  normalization is intended to convert this advection effect into a source term. Thus, this normalization will be called *advection normalization*. The  $e^{(x/x_o-1)}$  normalization is a mathematical technique to remove the extra source term in the continuity equation, Eq. (2.18). This will be called *continuity normalization*. All three contributions are summarized in Table 2.1.

Table 2.1: Sources of the forcing term

	Mean flow	Advection normalization	Continuity normalization
Longitudinal	$\frac{U_c}{x_o} u_x^*$	$\frac{U_c}{x_o} u_x^*$	$-\frac{U_c}{x_o} u_x^*$
Transverse	$-\frac{1}{2} \frac{U_c}{x_o} u_i^*$	$\frac{U_c}{x_o} u_i^*$	0

The source terms from the mean flow make this forcing scheme seem as simulating an axisymmetric expansion, but the two normalizations are essential to the derivation. The first normalization takes into account the decrease of  $\mathbf{u}'$  along the axial direction, and the second one maintains its continuity. The source terms from the two normalizations, with a combination with the mean flow terms, create turbulence in a 3D box that is similar to the centerline of a round jet.

### 2.3.3 Properties of the forcing scheme

Three key observations must be made about the derived forcing scheme.

First, this current forcing term is the result of applying the physical laws of a practical turbulent flow. The other forcing schemes introduced in Sec. 2.1 did not directly reflect the physical situations, but rather devised some arbitrary numerical methods to maintain the turbulence. Even Lundgren's linear forcing scheme introduced in Sec. 2.2 was theoretical; it was not specific to any flow configurations. The isotropic turbulence generated by this forcing is not close to any practical types of flows. In the present derivation, on the other hand, the physics of a practical flow is considered.

Second, the resultant source term is a linear forcing term. It may have been expected from the form of the term  $\mathbf{u}' \cdot \nabla \bar{\mathbf{u}}$  that the source term should be linear, but the additional normalizations also yield linear terms. Also, this new source term is a forcing term in physical space, not in spectral space. This physical forcing also injects energy throughout all the scales. It is essentially different from other spectral forcing schemes that often restrict the energy injection to narrow wavenumber regions.

Third, the forcing term is anisotropic; it is twice as strong in one direction as in the other directions. Lundgren's forcing term is also linear, but it is isotropic. Real flows rarely approach isotropy at the large scale. The anisotropic forcing in the current study is qualitatively consistent with the anisotropy of turbulent jets, in which the fluctuating velocity is stronger in one direction.

### 2.3.4 A priori analysis and simulation procedure

As detailed in [22], for triply periodic direct numerical simulations (DNS) with Lundgren's linear source term in physical space, the average values of some turbulent parameters, such as the kinetic energy  $k$  and the dissipation rate  $\varepsilon$ , can be predicted by analyzing the kinetic energy equation. The same analysis is applied to the current investigation.

First, Eq. (2.26) shows the balance between energy dissipation and energy production.

Let  $k_o$  and  $\varepsilon_o$  denote the expected values for the kinetic energy and dissipation rate, respectively. Also, the integral length scale is defined as

$$l \equiv \frac{\left(\frac{2}{3}k_o\right)^{3/2}}{\varepsilon_o}. \quad (2.31)$$

Let  $l_o$  denote its expected value. Using this definition with Eq. (2.26),  $k_o$  and  $\varepsilon_o$  may be expressed as

$$k_o = \frac{27 U_c^2}{8 x_o^2} \left(1 + \frac{\langle\langle u_x^{*2} \rangle\rangle}{\langle\langle \mathbf{u}^{*2} \rangle\rangle}\right)^2 l_o^2, \quad (2.32)$$

and

$$\varepsilon_o = \frac{27 U_c^3}{8 x_o^3} \left(1 + \frac{\langle\langle u_x^{*2} \rangle\rangle}{\langle\langle \mathbf{u}^{*2} \rangle\rangle}\right)^3 l_o^2, \quad (2.33)$$

where  $U_c$  and  $x_o$  are input values related to a particular experimental setup. The ratio  $\langle\langle u_x^{*2} \rangle\rangle / \langle\langle \mathbf{u}^{*2} \rangle\rangle$  and the integral length scale are outputs of the numerical simulations, which are unknown a priori.  $\langle\langle \cdot \rangle\rangle$  denotes time-averaging of volume-averaged values. As will be shown later in Sec. 2.4.3, they are found to be constant across a wide range of Reynolds numbers, and given by

$$l_o \approx 0.24L_x \quad (2.34)$$

$$\frac{\langle\langle u_x^{*2} \rangle\rangle}{\langle\langle \mathbf{u}^{*2} \rangle\rangle} \approx 0.49, \quad (2.35)$$

where  $L_x$  is the computational domain width. The integral length scale evaluated from any 3D box of turbulence is a function of the box size, and the ratio of  $l$  to  $L_x$  is determined by the forcing term. Rosales and Meneveau [52] found that  $l \approx 0.19L_x$ , when Lundgren's linear forcing term is used. For spectral methods,  $l/L_x$  ranges from 0.15 to 0.30.

It is well accepted that the integral length scale is proportional to the downstream distance. According to Pope [53],  $l \approx 0.0962x_o$  in a turbulent jet experiment. However, it should be noted that this approximation varies by experiments, mainly due to the different estimations of  $\varepsilon$ , as later shown in Sec. 2.4.6. In this study,  $l_o = 0.0962x_o$  is used to determine the domain width. Since we want the periodic DNS to have the same integral length scale as the experiments, we should set the size of the computational domain as

$$L_x = 0.399x_o. \quad (2.36)$$

The procedure of conducting the DNS in the current investigation can be summarized as follows:

- Find the centerline velocity  $U_c$  and the axial location  $x_o$  of the target experiment
- Use the ratio of  $U_c$  and  $x_o$  to determine the source term for the DNS
- Use  $x_o$  to determine the length of the DNS cubic box, as  $L_x = 0.399x_o$
- Perform the DNS in a triply periodic configuration

These various a priori values are compared against actual values from turbulent jet experiments and simulations in Sec. 2.4.6.

### 2.3.5 Reynolds numbers

The root mean square velocity fluctuation,  $u_{rms}$ , the Taylor-microscale,  $\lambda$ , and the Taylor-microscale Reynolds number,  $Re_\lambda$ , are defined as

$$u_{rms} = \sqrt{\frac{2k}{3}}, \quad (2.37)$$

$$\lambda = \sqrt{15 \frac{\nu}{\varepsilon} u_{rms}}, \quad (2.38)$$

$$Re_\lambda = \frac{\lambda u_{rms}}{\nu}. \quad (2.39)$$

The entire turbulent flow can be represented by  $Re_\lambda$ . Once appropriate normalizations are applied to the dimensional parameters,  $Re_\lambda$  is the only free input parameter for the triply periodic DNS [22, 52].  $Re_\lambda$  can also be predicted a priori, as  $k_o$  and  $\varepsilon_o$  are predicted in Sec. 2.3.4:

$$Re_\lambda^o = \sqrt{\frac{45 U_c}{2\nu x_o} \left( 1 + \frac{\langle\langle u_x^{*2} \rangle\rangle}{\langle\langle \mathbf{u}^{*2} \rangle\rangle} \right) l_o^2}. \quad (2.40)$$

$Re_\lambda^o$  is related to the number of grid points in each direction,  $N$ , and the spatial resolution determined by the dimensionless parameter  $\kappa_{max}\eta_k$  [56].  $\kappa_{max}$  is the maximum wavenumber, and  $\eta_k = (\nu^3/\varepsilon)^{1/4}$  is the Kolmogorov length scale. According to Yeung and Pope [57],  $\kappa_{max}\eta_k = 1.0$  is adequate for low-order velocity statistics, but at least  $\kappa_{max}\eta_k = 1.5$  is needed for higher-order quantities such as dissipation. Since the current study examines higher-order statistics as well as low-order ones, we want  $\kappa_{max}\eta_k \geq 1.5$ . In a triply periodic DNS,  $\kappa_{max} = \pi N/L_x$ . Then, the number of grid points is constrained by the Reynolds number.

$$N \geq \frac{1.5}{15^{1/4}\pi} \frac{L_x}{l} Re_\lambda^{o\ 3/2}. \quad (2.41)$$

This relation has been used a priori to determine proper grid resolutions for DNS 1-4 in Sec. 2.4.1.

Finally, the Reynolds number  $Re_D$  of the target experiment can be related to  $Re_\lambda$  of the DNS. Since the ratio  $U_c x_o/\nu$  is proportional to the jet Reynolds number  $Re_D$  [55],  $U_c x_o/\nu = C Re_D$ , where  $C$  is a constant typically ranging from 5 to 7 in turbulent round jet experiments [25, 27, 29, 54, 58, 59]. Then, it follows from Eq. (2.40) that

$$Re_\lambda^o = \sqrt{\frac{45}{2} C \left( \frac{l_o}{x_o} \right)^2 \left( 1 + \frac{\langle\langle u_x^{*2} \rangle\rangle}{\langle\langle \mathbf{u}^{*2} \rangle\rangle} \right) Re_D}. \quad (2.42)$$

This form of relation in a turbulent jet,  $Re_\lambda \sim Re_D^{1/2}$ , was also suggested by Antonia *et al.* [60].

## 2.4 Results

### 2.4.1 Simulation framework and parameters

The governing equations, Eqs. (2.23)–(2.25), are solved using the NGA [61] code. NGA is a three-dimensional finite difference solver suitable for variable density, low Mach number, laminar and turbulent flows. It solves the continuity and Navier-Stokes equations in physical space, not in spectral space, while discretely conserving kinetic energy. The Courant-Friedrichs-Lewy condition,  $CFL \leq 0.8$ , has been imposed for all the simulations in the current paper.

The initial velocity fields are randomly generated, following the method used by Eswaran and Pope [19]. The velocity fields are subject to the continuity constraint and conformed to a specified Passot-Pouquet energy spectrum [62]. A detailed explanation can be found in [63].

Four simulations have been conducted at different Reynolds numbers. The relevant parameters are shown in Table 2.2. The target experiment of DNS1 is Webster *et al.* [59]; DNS2, Vouros and Panidis [58]; DNS3, Panchapakesan and Lumley [25]; and DNS4, Antonia and Zhao [26]. Any experiment could be selected, but the limiting factor is the Reynolds number.

As stated in Sec. 2.3.4,  $U_c$  and  $x_o$  of each experiment are used to determine the domain width and forcing terms for the simulation.  $Re_\lambda$  is estimated a priori according to Eq. (2.40). Finally,  $N$  is determined according to Eq. (2.41).

Table 2.2: Relevant parameters of the target experiments and the corresponding simulations

	Target experiments			Simulation parameters		
	$U_c[m/s]$	$x_o[m]$	$Re_D$	$N$	$L_x[m]$	$Re_\lambda$
DNS1	0.0796	0.232	3000	192	0.0932	76
DNS2	2.06	0.239	5500	256	0.0920	99
DNS3	1.36	0.732	11000	512	0.294	140
DNS4	1.95	1.60	37000	1024	0.640	255

### 2.4.2 Instantaneous turbulence structures

Contours of the velocity from DNS1 are shown in Fig. 2.1, in comparison with those of homogeneous isotropic turbulence (HIT) at the same  $Re_\lambda$ . Each plot shows a cross section in the middle of the simulation cubic box, with 10 number of contour levels from its own minimum value (dark blue) to maximum value (bright yellow).

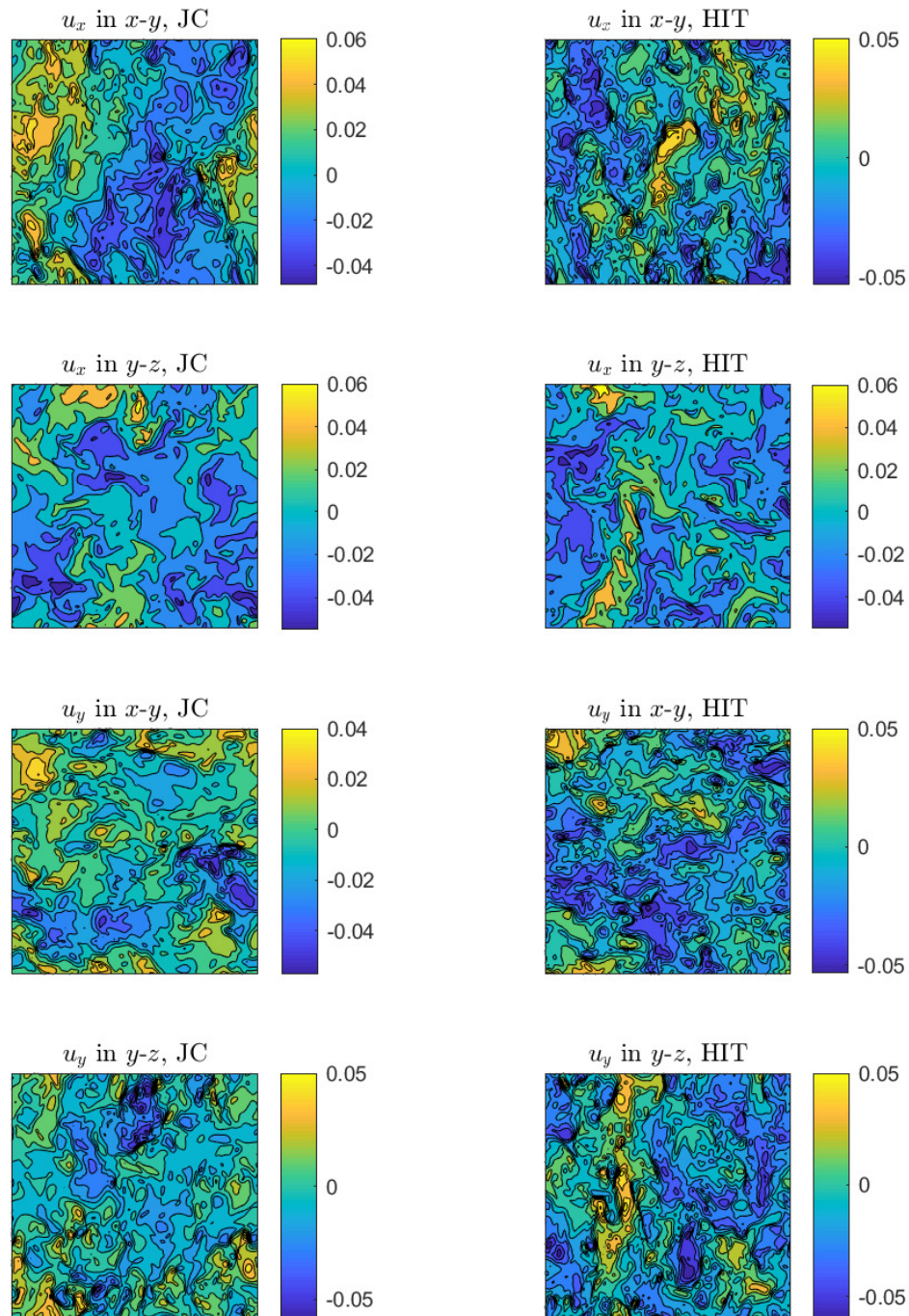


Figure 2.1: Contours of the velocity,  $u_x$  and  $u_y$ , from DNS1 with the jet centerline (JC) forcing, in comparison with homogeneous isotropic turbulence (HIT) at the same  $Re_\lambda$  in  $xy$  and  $yz$  planes.

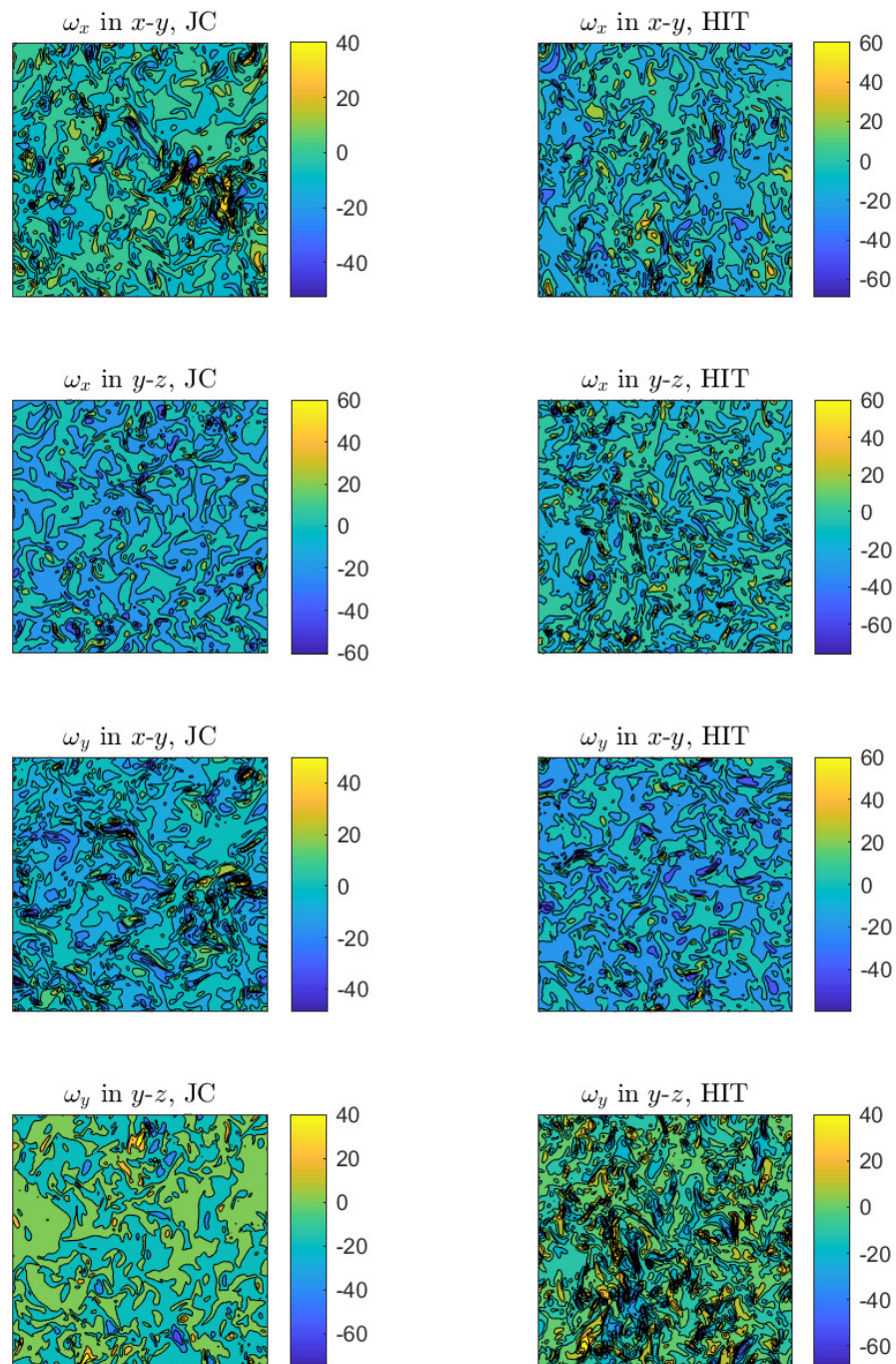


Figure 2.2: Contours of the vorticity,  $\omega_x$  and  $\omega_y$ , from DNS1 with the jet centerline (JC) forcing, in comparison with homogeneous isotropic turbulence (HIT) at the same  $Re_\lambda$  in  $xy$  and  $yz$  planes.

The homogeneous flow structures in the jet centerline (JC) simulations seem very similar to those of HIT. The anisotropy of JC forcing is difficult to observe.

Contours of the vorticity from the same simulation are shown in Fig. 2.2. Vorticity  $\omega$  is defined as

$$\omega = \left( \frac{\partial u_z}{\partial y} - \frac{\partial u_y}{\partial z} \right) \hat{\mathbf{i}} + \left( \frac{\partial u_x}{\partial z} - \frac{\partial u_z}{\partial x} \right) \hat{\mathbf{j}} + \left( \frac{\partial u_y}{\partial x} - \frac{\partial u_x}{\partial y} \right) \hat{\mathbf{k}}. \quad (2.43)$$

Vorticity also seems homogeneous and isotropic in both JC and HIT at any plane. It is difficult to find evident differences between JC and HIT. Additionally, there are very small regions in the highest or lowest level of vorticity. Most area is in the contour level with the smallest magnitude of vorticity.

### 2.4.3 Temporal fluctuations

After a transient period, the turbulence statistics under the linear forcing technique asymptotically reaches a unique solution [52]. Rosales and Meneveau noticed that the turbulent statistics are subject to large oscillations around their respective average values, even when the flow becomes statistically stationary. For the purpose of reducing the magnitudes of such oscillations while retaining the underlying physics, Carroll and Blanquart [22] proposed a modification to the linear forcing terms. Since the current study also uses linearly forcing terms, albeit anisotropic, the same modification is used for the simulations DNS 1-4:

- Longitudinal direction

$$\frac{\varepsilon_o}{\langle k^* + \frac{u_x^{*2}}{2} \rangle} u_x^*, \quad (2.44)$$

- Transverse directions

$$\frac{1}{2} \frac{\varepsilon_o}{\langle k^* + \frac{u_x^{*2}}{2} \rangle} u_i^*. \quad (2.45)$$

Figure 2.3 shows  $l$ ,  $\langle u_x^{*2} \rangle / \langle \mathbf{u}^{*2} \rangle$ ,  $\langle k^* \rangle / k_o$ , and  $\langle \varepsilon^* \rangle / \varepsilon_o$ , as a function of the normalized time,  $t/\tau_o$ , where  $\tau_o = k_o/\varepsilon_o$ .  $\tau_o$  is the eddy time scale determined a priori. The quantities are spatially averaged over the cubic box at each time step. All of the turbulent parameters reach statistical stationarity after a transient period. The length of the transient periods appears to depend on  $\text{Re}_\lambda$ ; simulations with higher  $\text{Re}_\lambda$  have shorter transient periods. For DNS1 with  $\text{Re}_\lambda = 76$ , stationary conditions are attained approximately at  $t/\tau_o = 6$ ; for DNS 4 with  $\text{Re}_\lambda = 255$ ,  $t/\tau_o = 3$ .

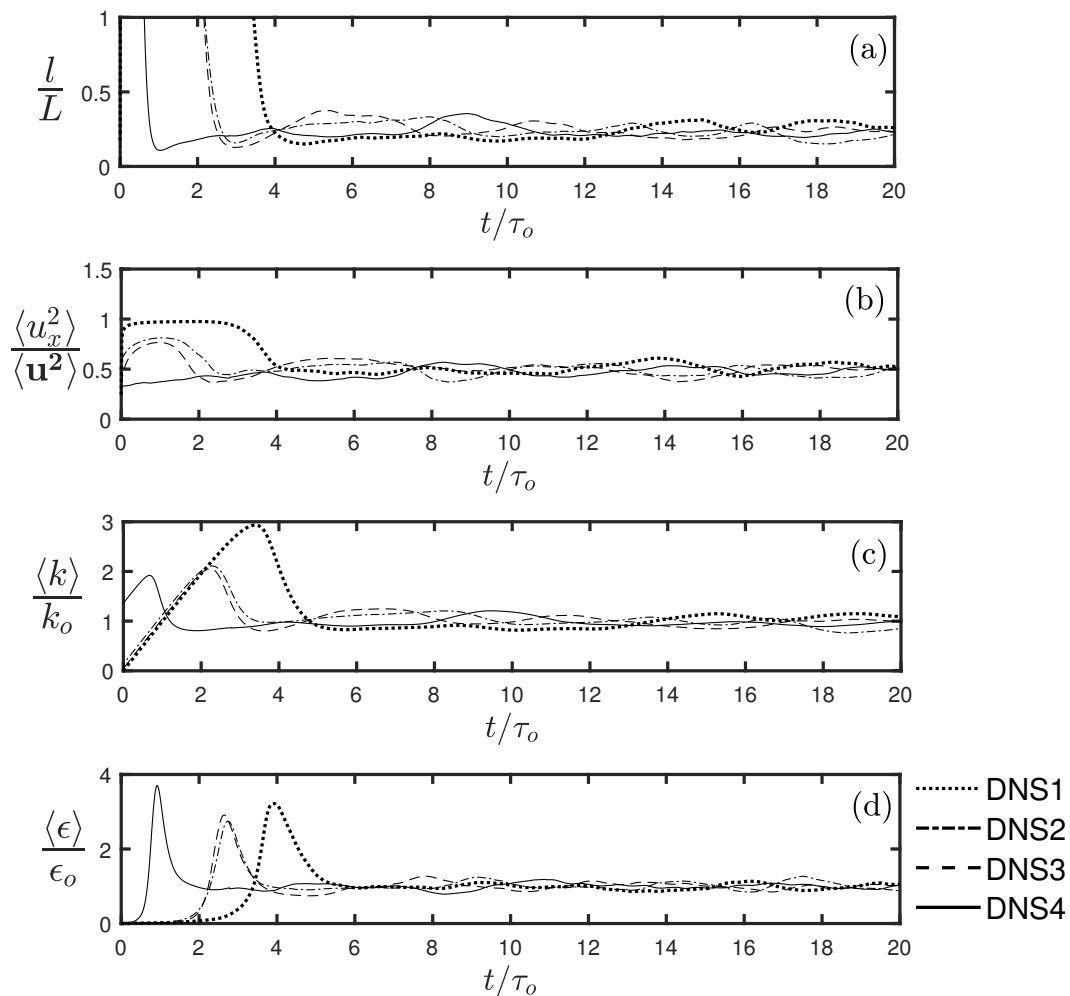


Figure 2.3: Temporal fluctuations of turbulent parameters: (a) ratio of the integral length scale,  $l$ , to the domain width,  $L_x$ ; (b) anisotropy  $\langle u_x^{*2} \rangle / \langle \mathbf{u}^{*2} \rangle$ ; (c) the volume-averaged kinetic energy,  $\langle k^* \rangle$ , with respect to the expected value,  $k_o$ ; (d) the volume-averaged dissipation rate,  $\langle \epsilon^* \rangle$ , with respect to the expected value,  $\epsilon_o$ . The parameters are plotted as a function of the time normalized by the a priori eddy time scale,  $\tau_o$ .

The mean values of the turbulent parameters and the magnitudes of fluctuations over the statistically stationary periods are shown in Table 2.3. The standard deviations are small enough to assume that the velocity fields have reached statistical stationarity.

The mean value of  $l/L_x$  is about 0.24, and the mean value of  $\langle u_x^{*2} \rangle / \langle \mathbf{u}^{*2} \rangle$  is about

Table 2.3: Mean values and standard deviations ( $Mean \pm SD$ ) of turbulent parameters over the statistically stationary region

	$l/L_x$	$\langle u_x^{*2} \rangle / \langle \mathbf{u}^{*2} \rangle$	$\langle k^* \rangle / k_o$	$\langle \varepsilon^* \rangle / \varepsilon_o$
DNS1	$0.238 \pm 0.002$	$0.504 \pm 0.002$	$0.986 \pm 0.011$	$0.996 \pm 0.006$
DNS2	$0.242 \pm 0.002$	$0.493 \pm 0.004$	$0.992 \pm 0.012$	$1.009 \pm 0.012$
DNS3	$0.239 \pm 0.002$	$0.485 \pm 0.003$	$1.002 \pm 0.011$	$1.001 \pm 0.007$
DNS4	$0.244 \pm 0.002$	$0.490 \pm 0.002$	$1.000 \pm 0.008$	$0.991 \pm 0.007$

0.49. It indicates that the mean values of the two parameters are independent of  $Re_\lambda$ , despite the small variations. In addition, Fig. 2.3 (c) and (d) display the temporal evolution of  $\langle k^* \rangle$  and  $\langle \varepsilon^* \rangle$  with their respective expected values. Regardless of  $Re_\lambda$ , the kinetic energy and dissipation rate indeed fluctuate around their expected values with relatively small amplitudes, when the system reaches statistical stationarity. Thus, it shows that the calculations for  $k_o$  and  $\varepsilon_o$  are quite accurate.

#### 2.4.4 Vorticity

Time-averaged values of volume-averaged vorticity  $\omega_i$  have been computed from DNS1-4 and an extra simulation at a lower Reynolds number, shown in Fig. 2.4. For each time-averaged quantity shown in this work, averaging uncertainty is presented as an error bar. This uncertainty quantification method is explained in details in Appendix A.

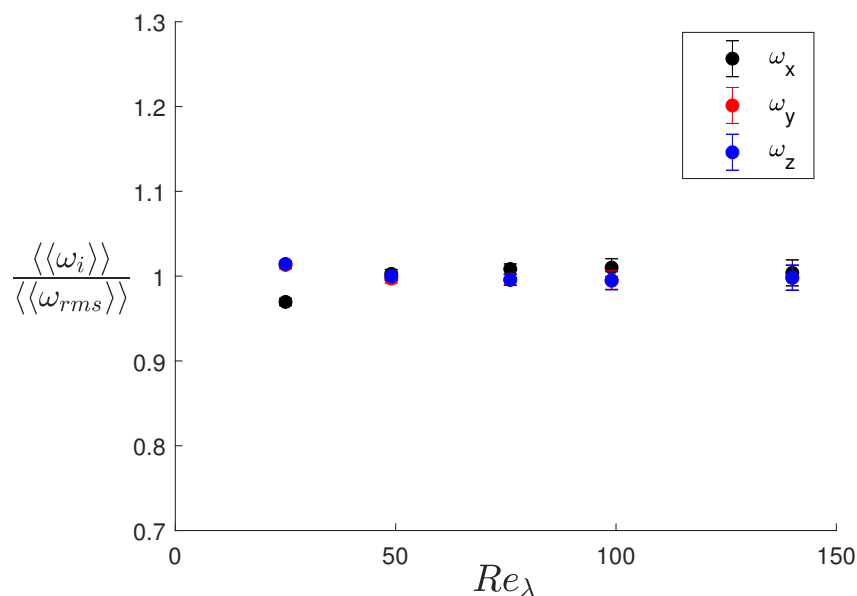


Figure 2.4: Normalized vorticity as a function of  $Re_\lambda$ .

The transverse vorticities,  $\omega_y$  and  $\omega_z$ , are almost exactly the same for all Reynolds numbers. At the lowest Reynolds number,  $Re_\lambda = 25$ , the longitudinal vorticity  $\omega_x$  is lower than the other two, but they quickly reach isotropy; i.e.  $\omega_i \approx \omega_{rms}$  for  $Re_\lambda \geq 49$ . The longitudinal vorticity  $\omega_x$  is slightly larger than  $\omega_y$  and  $\omega_z$  at  $Re_\lambda = 99$  and 140. However, the difference is only 1.3%.

This isotropy of vorticity is consistent with Kolmogorov's hypothesis of local isotropy [42] that the small-scale turbulent motions are statistically isotropic at sufficiently high Reynolds number. It is based on the notion that the anisotropy at large scales gets gradually lost as energy cascades down to smaller scales.

#### 2.4.5 Validation against experimental data - energy budget

We need to ensure that the simulation quantities, such as  $k^*$  and  $\varepsilon^*$ , are indeed equivalent to the experimental counterparts,  $k$  and  $\varepsilon$ . We start with the turbulent kinetic energy equation:

$$\begin{aligned}
 k &= \frac{1}{2} \mathbf{u}' \cdot \mathbf{u}' \Big|_{x=x_o} \\
 &= \frac{1}{2} \left[ \left( \frac{x_o}{x} e^{\left(\frac{x}{x_o}-1\right)} u_x^* \right)^2 + \left( \frac{x_o}{x} u_y^* \right)^2 + \left( \frac{x_o}{x} u_z^* \right)^2 \right] \Big|_{x=x_o} \\
 &= \frac{1}{2} \mathbf{u}^* \cdot \mathbf{u}^* = k^*
 \end{aligned} \tag{2.46}$$

To examine the dissipation rate, let us consider the kinetic energy equation for the full jet derived from Eq. (2.7). Neglecting the pressure term and viscous diffusion, we can write the ensemble-averaged energy equation as

$$-\overline{\mathbf{u}' \cdot \nabla \bar{\mathbf{u}} \cdot \mathbf{u}'} - \bar{\mathbf{u}} \cdot \nabla \bar{k} - \nabla \cdot \overline{\mathbf{u}' k} - \bar{\varepsilon}_k = 0. \tag{2.47}$$

These four terms are named production, advection, diffusion, and dissipation terms from left to right [25]. The production term is the same for experiment and simulation:

$$-\overline{\mathbf{u}' \cdot \nabla \bar{\mathbf{u}} \cdot \mathbf{u}'} \Big|_{x=x_o} = -\overline{\mathbf{u}^* \cdot \nabla \bar{\mathbf{u}} \cdot \mathbf{u}^*} \tag{2.48}$$

$$= \frac{U_c}{x_o} k_o \left( 3 \frac{\langle \langle u_x^{*2} \rangle \rangle}{\langle \langle \mathbf{u}^{*2} \rangle \rangle} - 1 \right). \tag{2.49}$$

For the advection term, we only apply the *advection normalization*, because *continuity normalization* is a mathematical technique to make the flow divergence-free,

and therefore should not be related to the advection term. Then,

$$-\bar{\mathbf{u}} \cdot \nabla \bar{k}|_{x=x_o} = -\bar{\mathbf{u}} \cdot \nabla \frac{x_o^2}{x^2} k^* \Big|_{x=x_o} \quad (2.50)$$

$$= \bar{\mathbf{u}} \cdot \nabla \bar{k}^* + 2 \frac{U_c}{x_o} k_o. \quad (2.51)$$

The diffusion term is zero for both experiments and simulations, because these third-order moments are zero:

$$-\nabla \cdot \overline{\mathbf{u}'k}|_{x=x_o} = -\nabla \cdot \overline{\mathbf{u}^*k^*} + \frac{3}{2x_o} \overline{u_x^*k^*} = 0. \quad (2.52)$$

Finally, the dissipation term is simply the negation of the sum of the other terms:

$$\bar{\varepsilon}_k|_{x=x_o} = -\left(\bar{\mathbf{u}} \cdot \nabla \bar{k} + \overline{\mathbf{u}' \cdot \nabla \bar{\mathbf{u}} \cdot \mathbf{u}'} + \nabla \cdot \overline{\mathbf{u}'k}\right)|_{x=x_o} \quad (2.53)$$

$$= \frac{U_c}{x_o} k_o \left(1 + 3 \frac{\langle\langle u_x'^2 \rangle\rangle}{\langle\langle \mathbf{u}'^2 \rangle\rangle}\right). \quad (2.54)$$

With the expression for  $k_o$  from Eq. (2.32) and  $\langle\langle u_x'^2 \rangle\rangle / \langle\langle \mathbf{u}'^2 \rangle\rangle = 0.49$  from Eq. (2.35), these four terms are directly compared against experimental values of Panchapakesan and Lumley [25] in Fig. 2.5. Each term is normalized by  $U_c^3 / r_{1/2}$ . The half-width of a round jet,  $r_{1/2}$ , is the radial distance where the axial velocity is  $\frac{1}{2}U_c$ . According to Panchapakesan and Lumley,  $r_{1/2} = 0.096x_o$ . Since the target flow of the current study is the centerline region of a round jet, the estimated values for each term are plotted as points at  $\eta = 0$ . Despite small differences, all of the four terms agree well with the experimental measures.

Note that the expression for  $\bar{\varepsilon}_k$  in Eq. (2.54) is different from the expression for  $\varepsilon_o$  in Eq. (2.33). The difference is caused by the *continuity normalization*, which creates an extra term through  $\bar{\mathbf{u}} \cdot \nabla \bar{k}$ . In other words,  $\varepsilon_k$  is equivalent to the sum of  $\varepsilon_o = 2\nu \overline{S_{ij}^* S_{ij}^*}$  computed from our DNS and the additional term from the *continuity normalization*; i.e.,

$$\bar{\varepsilon}_k = \varepsilon_o + 2 \frac{U_c}{x_o} k_o \left(\frac{\langle\langle u_x'^2 \rangle\rangle}{\langle\langle \mathbf{u}'^2 \rangle\rangle}\right). \quad (2.55)$$

#### 2.4.6 Validation against experimental data - single point values

As demonstrated in Sec. 2.4.3 and Sec. 2.4.5, the following values are the results of the DNS with the present source term:

$$\frac{k_o}{U_c^2} = 0.0698, \quad (2.56)$$

$$\frac{\varepsilon_{k,o}}{U_c^3 / x_o} = 0.171. \quad (2.57)$$

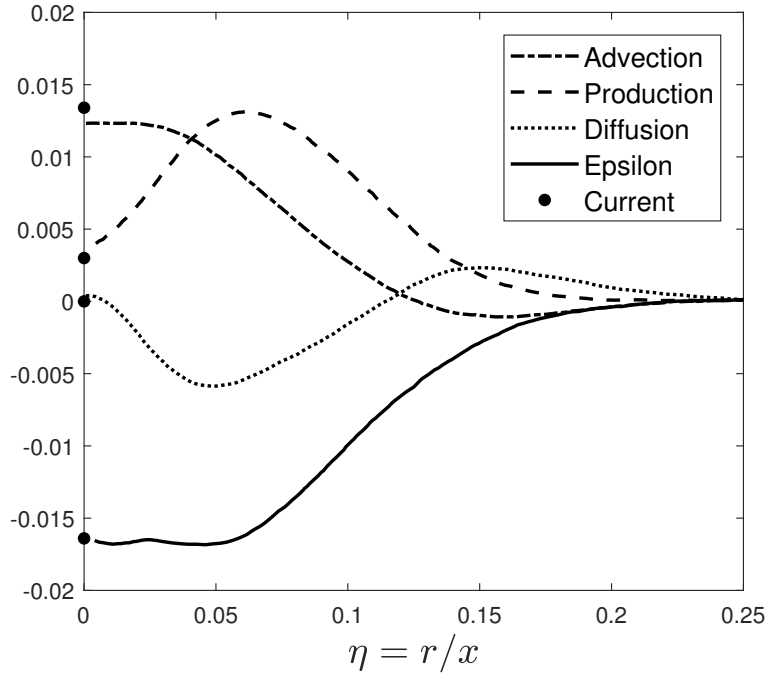


Figure 2.5: Energy budget comparison. Each term is normalized by  $U_c^3/r_{1/2}$ . The lines are experimental data from P&Lu [25], and the points are the estimated values from Eqs. (2.48)–(2.54).

$\varepsilon_{k,o}$  is the expected value of  $\bar{\varepsilon}_k$  for our simulations.

The three normalized scalar quantities, anisotropy  $\frac{\overline{u_x'^2}}{\mathbf{u}'^2}$ , normalized kinetic energy  $\frac{\bar{k}}{U_c^2}$ , and normalized dissipation rate  $\frac{\bar{\varepsilon}}{U_c^3/x_o}$ , from various jet experiments and DNS are plotted as a function of  $\text{Re}_D$  in Fig. 2.6. Table 2.4 shows the Reynolds number, jet fluid, and velocity-measuring technique of each experiment used for the comparison.

A dashed line is used to represent the corresponding values of the current study,  $\frac{\langle\langle u_x^{*2} \rangle\rangle}{\langle\langle \mathbf{u}^{*2} \rangle\rangle}$ ,  $\frac{k_o}{U_c^2}$ , and  $\frac{\varepsilon_{k,o}}{U_c^3/x_o}$ , for all the Reynolds numbers, since the results are independent of the Reynolds number. For the energy dissipation rate,  $\varepsilon_k$  is used instead of  $\varepsilon_o$ , because  $\varepsilon_k$  is the quantity equivalent to the dissipation in experiments.

Experiments used for the comparison have estimated the dissipation  $\bar{\varepsilon}$  in different ways. Panchapakesan & Lumley [25] obtained  $\bar{\varepsilon}$  by balancing the energy budget equation; they inherently computed  $\bar{\varepsilon}_k$  in Eq. (2.53). Antonia & Zhao [26] and Romano & Antonia [27] computed a temporal  $u_x'$  energy spectrum  $\phi_u(f)$ , defined such that  $\int_0^\infty \phi_u(f) df = \overline{u_x'^2}$ . Then, they converted  $\phi_u(f)$  to a spatial  $u_x$  energy

spectrum  $\phi_u(\kappa_1)$  by using Taylor's frozen turbulence hypothesis [64], and finally estimated  $\bar{\varepsilon}$  from the isotropic relation  $\bar{\varepsilon}_{iso} = 15\nu\overline{(\partial u'_x/\partial x)^2}$ , in which  $\overline{(\partial u'_x/\partial x)^2}$  was inferred from the integral  $\int_0^\infty \kappa_1^2 \phi_u(\kappa_1) d\kappa_1$ .

Burattini *et al.* [30] used the homogeneous relation,  $\bar{\varepsilon}_{hom} = 3\nu\left(\overline{(\partial u'_x/\partial x)^2} + 2\overline{(\partial u'_y/\partial x)^2}\right)$ . Wygnanski & Fiedler [29] devised its own semi-isotropic relation for the centerline dissipation rate:

$$\bar{\varepsilon} = 2\nu \left[ \overline{\left(\frac{\partial u'_x}{\partial x}\right)^2} + 5\overline{\left(\frac{\partial u'_x}{\partial y}\right)^2} + 2\overline{\left(\frac{\partial u'_y}{\partial x}\right)^2} \right], \quad (2.58)$$

which is based on the assumption that

$$2\overline{\left(\frac{\partial u'_x}{\partial x}\right)^2} = \overline{\left(\frac{\partial u'_y}{\partial x}\right)^2} = \overline{\left(\frac{\partial u'_z}{\partial x}\right)^2}, \quad (2.59)$$

$$\overline{\left(\frac{\partial u'_x}{\partial y}\right)^2} = 2\overline{\left(\frac{\partial u'_y}{\partial y}\right)^2} = \overline{\left(\frac{\partial u'_z}{\partial y}\right)^2} = \overline{\left(\frac{\partial u'_x}{\partial z}\right)^2} = \overline{\left(\frac{\partial u'_y}{\partial z}\right)^2} = 2\overline{\left(\frac{\partial u'_z}{\partial z}\right)^2}. \quad (2.60)$$

Darisse *et al.* [31] adopted the expression from Thiesset *et al.* [65] for the centerline dissipation rate:

$$\frac{\bar{\varepsilon}r_{1/2}}{U_c^3} = B_{RU} \frac{\overline{u_x'^2}}{U_c^2} \left( 2 + \frac{\overline{u_y'^2}}{\overline{u_x'^2}} \right), \quad (2.61)$$

where  $B_{RU}$  is the jet spreading rate, such that  $r_{1/2} = B_{RU}x$ . Thiesset *et al.* derived this equation from the (-4)th power law based on a classical self-similarity analysis [66],

$$\frac{\bar{\varepsilon}d}{U_o^3} = A_\varepsilon \left(\frac{x}{d}\right)^{-4}, \quad (2.62)$$

in which Thiesset *et al.* found the expression for  $A_\varepsilon$  under the assumptions of local isotropy and complete self-preservation.

One should first acknowledge that the published values do not completely agree with one another, even among experiments or computations. Instead, there seem to be some ranges of values for the respective parameters: 0.40–0.58 for  $\frac{\overline{u_x'^2}}{u'^2}$ , 0.05–0.09 for  $\frac{\bar{k}}{U_c^2}$ , and 0.08–0.23 for  $\frac{\bar{\varepsilon}}{U_c^3/x_o}$ . Possible reasons for these differences include the state of the boundary layer on the nozzle wall, differences in the experimental techniques, and different ways to estimate derivatives. The value of each parameter

Table 2.4: Round jet experiments and DNS used for the comparison.

	Author	$Re_D$	Fluid	Technique
Experiment	Papanicolaou & List [24]	7000	Water	Laser Doppler
	Panchapakesan & Lumley [25]	11000	Air	Hot-wire
	Antonia & Zhao [26]	2500 – 11000	Air	Hot-wire
	Romano & Antonia [27]	49000	Water	Laser Doppler
	Xu & Antonia [28]	37000 – 73000	Air	Hot-wire
	Wynanski & Fiedler [29]	100000	Air	Hot-wire
	Burattini <i>et al.</i> [30]	130000	Air	Hot-wire
	Darisse <i>et al.</i> [31]	140000	Air	Laser Doppler
DNS	Boersma <i>et al.</i> [32]	2400		
	Boersma [33]	5000		

for the current study lies within its respective range. Lundgren's forcing scheme would have  $\frac{\langle\langle u_x'^2 \rangle\rangle}{\langle\langle u'^2 \rangle\rangle} = 0.33$ , below the experimental values.

In addition, the origins of the forcing term are examined again in Fig. 2.7. *Mean* only uses the forcing term from  $\nabla \bar{u}$ . Thus, the forcing term is the first column of Table I:  $\frac{1}{2} \frac{U_c}{x_o} (2u_x^* \hat{\mathbf{i}} + u_y^* \hat{\mathbf{j}} + u_z^* \hat{\mathbf{k}})$ . *Mean+Adv* uses the forcing term from  $\nabla \bar{u}$  and the advection normalization; thus, the forcing term is the sum of the first and second columns of Table I:  $\frac{1}{2} \frac{U_c}{x_o} (4u_x^* \hat{\mathbf{i}} + u_y^* \hat{\mathbf{j}} + u_z^* \hat{\mathbf{k}})$ . *All* uses the original forcing term derived in Sec. 2.3.2.

The time-averaged values from  $10\tau_o$  to  $50\tau_o$  are displayed in Table 2.5. Also, the ranges for the experimental values are shown. Among the three forcing terms, only the original *All* forcing produces the turbulent characteristics of round jets correctly. These plots and table above help to show that the two normalizations are essential to create the right turbulence.

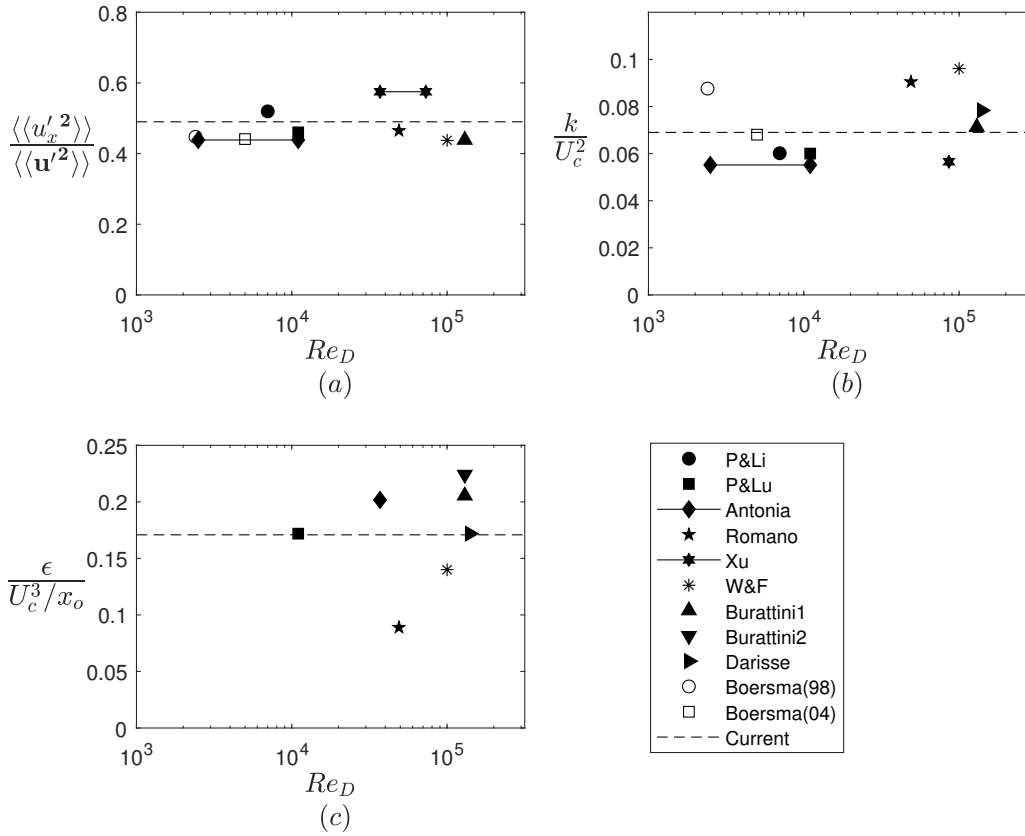


Figure 2.6: Single point values comparison: (a) anisotropy  $\frac{\overline{u_x'^2}}{\overline{\mathbf{u}'^2}}$ ; (b) normalized kinetic energy  $\frac{\bar{k}}{U_c^2}$ ; (c) normalized dissipation rate  $\frac{\bar{\epsilon}}{U_c^3/x_o}$ . Boersma(98) [32] and Boersma(04) [33] are DNS. P&Li [24], P&Lu [25], Antonia [26], Romano [27], Xu [28], W&F [29], Burattini [30], and Darisse [31] are experiments.

### 2.4.7 Validation against experimental data - energy spectra

The energy spectrum is compared against the experiment of Burattini *et al.* [30]. The one-dimensional energy spectrum,  $\phi_k(\kappa_1)$ , is defined as

$$\int_0^\infty \phi_k(\kappa_1) d\kappa_1 = \langle k \rangle, \quad (2.63)$$

where  $\kappa_1$  is the wavenumber in the longitudinal direction.  $\phi_k(\kappa_1)$  is the Fourier transformed function of the spatial correlation function  $\langle \mathbf{u}'(\mathbf{x}) \cdot \mathbf{u}'(\mathbf{x} + \mathbf{r}_1) \rangle$ , where  $\mathbf{r}_1$  is a vector in the longitudinal direction.

This spatial energy spectrum,  $\phi_k(\kappa_1)$ , can be easily computed in the triply periodic DNS. Since the governing equations in this study are in the Lagrangian reference

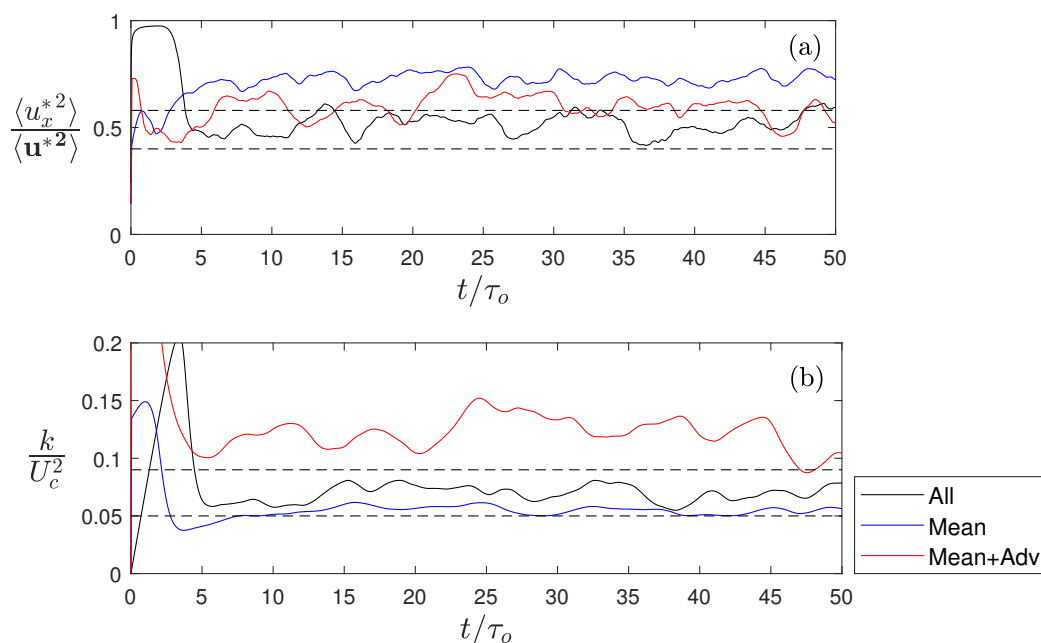


Figure 2.7: Examination of the origins of the forcing term: (a) anisotropy  $\frac{\langle u_x^{*2} \rangle}{\langle \mathbf{u}^{*2} \rangle}$ ; (b) normalized kinetic energy  $\frac{\langle k^* \rangle}{U_c^2}$ . The parameters are plotted as a function of the time normalized by the a priori eddy time scale,  $\tau_o$ . *All* (black) refers to the original forcing term; *Mean* (blue), the forcing term from  $\nabla \bar{\mathbf{u}}$  only; *Mean+Adv* (red), the forcing term from  $\nabla \bar{\mathbf{u}}$  and advection normalization.

Table 2.5: Examination of the origins of the forcing term: time-averaged values of turbulent parameters. For our study,  $\frac{\langle \langle u_x^{*2} \rangle \rangle}{\langle \langle \mathbf{u}^{*2} \rangle \rangle}$  and  $\frac{\langle \langle k^* \rangle \rangle}{U_c^2}$  are used. For experiments,  $\frac{\overline{u_x'^2}}{\overline{\mathbf{u}'^2}}$  and  $\frac{\bar{k}}{U_c^2}$  are used.

	$\frac{\langle \langle u_x^{*2} \rangle \rangle}{\langle \langle \mathbf{u}^{*2} \rangle \rangle}$	$\frac{\langle \langle k^* \rangle \rangle}{U_c^2}$
All	0.49	0.070
Mean	0.73	0.056
Mean+Adv	0.60	0.12
Experiments	0.40 – 0.58	0.05 – 0.09

frame, the spatial energy spectrum of our DNS can be compared to the temporal energy spectrum of an experiment, which assumes Taylor's frozen turbulence hypothesis [64]. The energy spectra from Burattini *et al.* and DNS4 are displayed in Fig. 2.8. The two spectra agree with each other very well in the inertial-convective

subrange as well as in the dissipative subrange. The small deviation in the high wavenumber region may be caused by the estimation of  $\eta_k$  in the experiment.

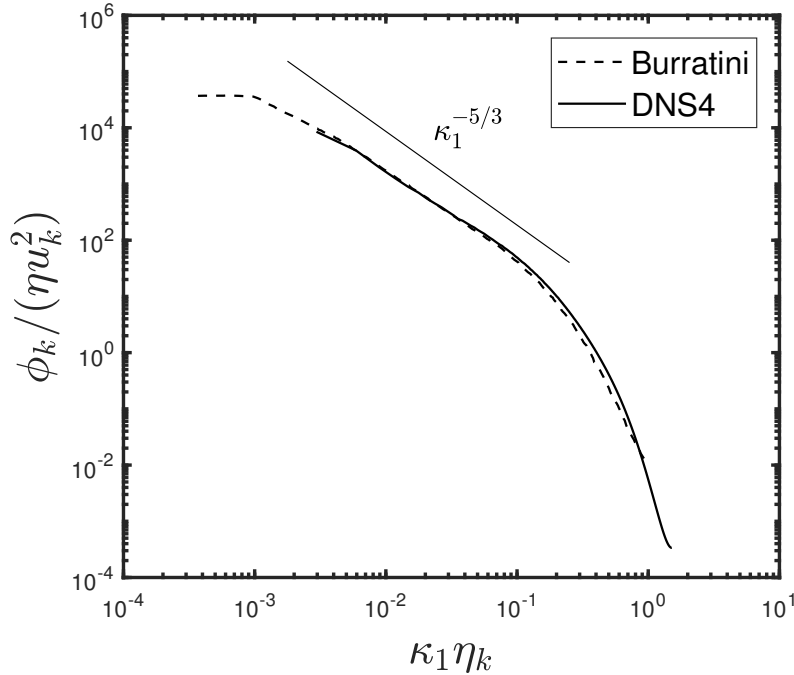


Figure 2.8: Comparison of normalized kinetic energy spectra in the longitudinal direction. Kolmogorov velocity scale,  $u_k = (\nu\varepsilon)^{1/4}$ , is used for normalization.

Burratini *et al.* obtained the relation,  $\phi_k \sim \kappa^{-1.52}$ , by using a least squares fit to the spectrum in the inertial subrange. We use the following model spectrum from Pope [53] to determine the power-law scaling:

$$\hat{\phi}_k(\kappa_1) = C_1 \varepsilon^{2/3} \kappa_1^{-n} f_L(\kappa_1 L) f_\eta(\kappa_1 \eta_k), \quad (2.64)$$

$$f_\eta(\kappa_1 \eta_k) = \exp\left(-\beta \left[ \left( (\kappa_1 \eta_k)^4 + c_\eta^4 \right)^{1/4} - c_\eta \right]\right), \quad (2.65)$$

$$f_L(\kappa_1 L) = \left( \frac{\kappa_1 L}{((\kappa_1 L)^2 + c_L)^{1/2}} \right)^{11/3}, \quad (2.66)$$

where  $C_1$  is a constant and  $L = k^{3/2}/\varepsilon$ . For high Reynolds numbers,  $c_\eta = 0.2$ ,  $\beta = 4.7$ , and  $c_L = 6.78$  should be appropriate, according to Pope [53]. A least-squares fit is used over the inertial subrange and the dissipation range with Eq.(2.64) to determine  $C_1 = 2.69$  and  $n = 1.50$ . The fitting results and verification of the model are shown in Table 2.6. The kinetic energy, computed from  $\int \hat{\phi}_k d\kappa$ , and the dissipation rate, computed from  $\int 2\nu\kappa^2 \hat{\phi}_k d\kappa$ , are compared against the actual values.

Table 2.6: Least-squares fit results.

	$C_1$	$n$	$k_{\text{fit}}$	$k$	$\varepsilon_{\text{fit}}$	$\varepsilon$
DNS4	2.69	1.50	0.280	0.285	0.407	0.418

The scalings from Burattini *et al.* and our study are very close to each other, different from the high-Reynolds number theoretical prediction of Kolmogorov [42]. The Reynolds numbers of both Burattini's experiment and DNS4 might not be high enough to reach  $n = -5/3$ , which is obtained as a result of assuming a very large Re.

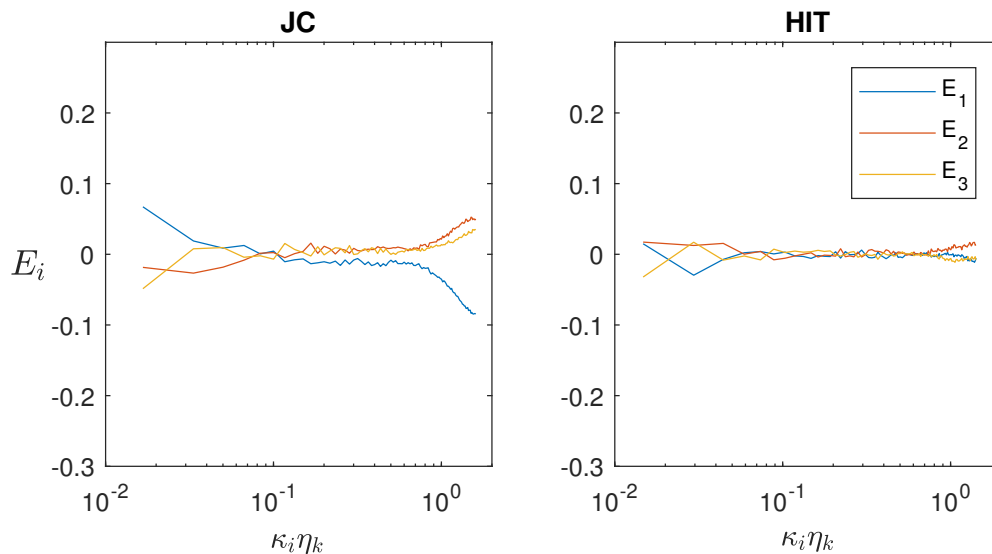
## 2.5 Energy spectra - anisotropy

To examine anisotropy through energy spectra, the following expression has been computed for DNS1 and HIT at a similar  $Re_\lambda$  and shown in Fig. 2.9:

$$E_i(\kappa_i) = \frac{\phi_i(\kappa_i)}{\sum_{i=1}^3 \phi_i(\kappa_i)} - \frac{1}{3}, \quad (2.67)$$

where

$$\int_0^\infty \phi_i(\kappa_i) d\kappa_i = \langle u_i^2 \rangle. \quad (2.68)$$

Figure 2.9: Comparison of  $E_i$  for JC and HIT.

The presented spectra have been computed from the velocity data at one time. Thus, there are some numerical uncertainties associated with the convergence of the

statistics. However, it is not necessary to average the spectra over time, in order to see the anisotropy existing in the spectral space.

For HIT case, the value of  $E_i$  is zero for all three directions, as expected for an isotropic flow. For JC, on the other hand,  $E_1$  is different from  $E_2$  and  $E_3$ , indicating the anisotropy introduced by the forcing scheme. Higher energy is contained in the low wavenumber region of  $E_1$ , which is consistent with our results that the longitudinal velocity is stronger than the transverse velocities. This anisotropy is located at the large scales and disappear at  $\kappa \approx \geq 0.1$ .

It is observed that  $E_1$  is smaller than  $E_2$  and  $E_3$  at very small scales. However, this apparent anisotropy is purely a numerical issue as Eq. (2.67) involves a division of two very small numbers at such small wavenumbers. The spectra are isotropic in the middle range, which is consistent with the isotropy of vorticity discussed in Sec. 2.4.4.

## 2.6 Summary

Existing forcing schemes are numerical methods that successfully prevent the turbulence from decaying, but they were not derived by using the information of a specific flow. In contrast, the purpose of this work was to derive a forcing technique based on the physical properties of a practical turbulent flow. Reynolds decomposition with the mean velocity of a turbulent round jet was used to find the momentum equations for the fluctuating velocity. The resulting forcing terms are found to be anisotropic linear forcing terms in physical space.

First, the anisotropy, kinetic energy, and dissipation rate were compared against multiple experiments. DNS results were found to be within the range of experimental values. Then, the energy budget terms were compared against experimental values at the centerline of a turbulent round jet. Finally, the spectrum computed from the DNS data of the current study agrees well with that of Burattini *et al.*, including the scaling of about  $\kappa^{-1.5}$  in the inertial-convective region. Thus, it seems appropriate to conclude that the proposed forcing terms successfully produce the turbulent characteristics of a turbulent round jet in a triply periodic box.

The essence of this work is to show the possibility that a forcing technique (for 3D periodic box turbulence) can be based on the physics of a practical flow, instead of being an arbitrary numerical method as all the previous ones. The current forcing term is focused on the centerline of a jet in the self-similar region. It is also developed to be used only in a 3D periodic box of turbulence. We developed a forcing scheme

for this local area on purpose, so that the forcing terms are simple and clear. By using similar derivation methods, however, more forcing terms can be discovered for different flow geometries.

*Chapter 3***A NUMERICAL FORCING SCHEME TO GENERATE PASSIVE SCALAR MIXING ON THE CENTERLINE OF TURBULENT ROUND JETS IN A TRIPLY PERIODIC BOX**

Chapter 3 has been adapted from:

[67] Kyupaekc Jeff Rah and Guillaume Blanquart. A numerical forcing scheme to generate passive scalar mixing on the centerline of turbulent round jets in a triply periodic box. *Physical Review Fluids*. (Under review).

Numerical studies of passive scalars in 3D periodic box turbulence have often used arbitrary scalar forcing schemes to sustain the variance. These existing methods do not represent specific practical flow configurations. In this work, a forcing technique is devised to generate centerline scalar mixing of round jets in a triply periodic box. It is derived from the scalar transport equation using a Reynolds-like decomposition of the scalar field. The equation is closed by applying the known mean velocity and scalar profiles of axisymmetric jets. The result is a combination of a mean gradient term and a linear scalar term. Direct numerical simulations at different  $Re_\lambda$  have been performed with these source terms for unity Schmidt numbers. Scalar flux values and scaling exponents of energy spectra from simulations are comparable to experimental values. In addition, a dimensional analysis shows that the normalized scalar statistics, such as variance, flux, and dissipation rate, should only be a function of Reynolds number; indeed, such quantities computed from our simulations approach constant values as the Reynolds number increases. The effects of velocity forcing on scalar fields are also investigated; changing velocity forcing terms may result in unstable scalar fields even under the same scalar forcing. It indicates that the velocity and scalar forcing schemes cannot be selected independently from each other.

**3.1 Previous scalar forcing methods**

Passive scalars refer to diffusive scalar quantities that are convected by the velocity field but do not influence the fluid motion itself. The transport of passive scalars in

an incompressible flow is governed by the following equation:

$$\frac{\partial C}{\partial t} + \mathbf{u} \cdot \nabla C = \nabla \cdot (D \nabla C), \quad (3.1)$$

where  $C$  is the scalar,  $D$  is its diffusivity, and  $\mathbf{u}$  is the velocity. Numerical computations are often used to examine the mixing characteristics of passive scalars, but the computational cost and complexity of geometry can make it difficult to conduct them. To cope with these problems, a 3D periodic box with zero mean scalar and velocity has been used intensively to study scalar turbulence [8–17, 23, 50]. Unfortunately, the solution of Eq. (3.1) with triply periodic boundary conditions is that of a decaying scalar field.

Scalar variance can be prevented from decaying by including a source term in the scalar transport equation. Below is the incompressible advection-diffusion equation with a forcing term:

$$\frac{\partial C'}{\partial t} + \mathbf{u} \cdot \nabla C' = \nabla \cdot (D \nabla C') + f_c, \quad (3.2)$$

where  $C'$  is the forced scalar and  $f_c$  is a forcing term. Three main schemes have been proposed in the literature: mean gradient forcing (MG) [8], linear scalar forcing (LS) [50], and reaction analogy forcing (RA) [23].

The mean gradient forcing technique (MG) [8] models a passive scalar in the presence of a mean gradient  $\mathbf{G}$  (e.g.  $\langle -g, 0, 0 \rangle$ ) across the scalar field. The forcing term can be derived by imposing a mean gradient:

$$C = C' + \mathbf{G} \cdot \mathbf{x}. \quad (3.3)$$

Then, the derived forcing term is  $f_c = -\mathbf{u} \cdot \mathbf{G}$ . Various numerical studies with the MG method have been conducted to examine the scalar mixing characteristics over a range of Schmidt numbers [8–11], with a particular emphasis on scalar flux [12], dissipation [13, 14], spectrum [15], and structure functions [16, 17].

The linear scalar forcing technique (LS) [50] aims to capture the nature of decaying turbulence. The derivation of the forcing term begins by normalizing the scalar field:

$$C' = C \sqrt{\frac{\sigma_t^2}{\sigma_c^2}}, \quad (3.4)$$

where  $\sigma_t^2$  is the targeted arbitrary scalar variance, and  $\sigma_c^2$  is the unforced scalar variance. When Eq. (3.4) is applied to Eq. (3.1) with an approximation that  $\sigma_t^2 = \sigma^2$

in the long-time limit, the forcing term  $f_c = \frac{1}{2} \frac{\overline{\chi}}{\sigma^2} C'$  is derived, where  $\chi \equiv 2D|\nabla C'|^2$  is the scalar dissipation rate and  $\sigma^2$  is the variance of  $C'$ . The overline  $\overline{\cdot}$  denotes ensemble-averaging.

The reaction analogy forcing technique (RA) [23] models a hypothetical chemical reaction that reverts the mixing process. The forcing term is

$$f_c = \text{sign}(C) f_c |C|^n (1 - |C|)^m, \quad (3.5)$$

where  $m$  and  $n$  are the stoichiometric coefficients of the hypothetical reaction.  $f_c = 2mK/2^m$ , where  $K$  is the reaction rate constant.

Although these three forcing methods successfully maintain scalar variance at a certain value, they do not represent specific practical flow configurations. Moreover, their derivations do not involve any information about velocity fields, nor is there any relation between the scalar forcing and the velocity forcing. The main objective of the current work is to introduce the first scalar forcing scheme that indeed generates the mixing of a specific practical flow. The target mixing is that of a fully-developed turbulent round jet in the centerline region with unity Schmidt number.

In Sec. 3.2, the forcing term is derived, and a dimensional analysis is provided. In Sec. 3.3, simulation results are presented and compared against experiments. Finally, in Sec. 3.4, the effects of velocity forcing on the scalar field are discussed.

## 3.2 Proposed forcing term

### 3.2.1 Derivation of the forcing term

In a similar fashion to the velocity case introduced in Sec. 2.3.2, the goal is to derive a scalar source term that generates turbulent mixing similar to that of a round jet on the centerline. This methodology is developed to be used in a cubic box with periodic boundary conditions. The passive scalar inside the box will be homogeneous with zero mean. In a practical round jet, however, the fluctuating scalar  $C'$  is known to decrease with the axial direction as  $1/x$  [55]. Thus, to make the scalar appropriate for homogeneity and periodic boundary conditions, the following normalization is suggested:

$$C^* = \frac{x}{x_o} (C - \overline{C}), \quad (3.6)$$

where  $C$  is the original scalar, and  $\overline{C}$  is the mean scalar.

With Eq. (2.19) and (3.6), we can obtain the governing equation for the scalar fluctuation from the incompressible advection-diffusion equation, Eq. (3.1). Then,

each term can be evaluated on the centerline (i.e.  $r = 0$ ) and at  $x = x_o$  by using the mean profiles for  $\bar{u}$  from [53, 55] and  $\bar{C}$  from [24, 59, 68–70]:

$$\bar{C} = C_c \exp\left(-\gamma_1(r/x)^2\right), \quad (3.7)$$

where  $C_c$  is the centerline mean scalar, and  $\gamma_1$  is a constant to be determined by the experiment. The result is

$$\begin{aligned} \frac{\partial C^*}{\partial t} + \mathbf{u}^* \cdot \nabla C^* - \nabla \cdot (D \nabla C^*) = \\ \frac{U_c}{x_o} C^* + \frac{C_c}{x_o} u_x^* + \overline{\mathbf{u}^* \cdot \nabla C^*} \\ + \frac{u_x^* C^*}{x_o} - \frac{\overline{u_x^* C^*}}{x_o} + 2D \left( \frac{C^*}{x_o^2} - \frac{1}{x_o} \frac{\partial C^*}{\partial x} \right). \end{aligned} \quad (3.8)$$

Each term of Eq. (3.8) impacts the distribution of  $C^*$  to a different extent. For the current study, it is our intent to retain only those terms significantly contributing to the first and second moment of  $C^*$ . Other terms will be considered negligible.

First,  $\overline{\mathbf{u}^* \cdot \nabla C^*}$  and  $\overline{u_x^* C^*}/x_o$  appear as  $\overline{C^* \mathbf{u}^* \cdot \nabla C^*}$  and  $\overline{C^* u_x^* C^*}/x_o$ , respectively, in the scalar variance equation. They do not contribute to the mean scalar variance, because  $\overline{C^*} \equiv 0$ . Similarly,  $u_x^* C^*/x_o$  appears as  $\overline{u_x^* C^{*2}}/x_o$  in the variance equation. The magnitude of  $\overline{u_x^* C^{*2}}/x_o$  can be compared to that of  $U_c \overline{C^{*2}}/x_o$ . According to experiments [25, 31, 71], the value of  $\overline{u_x' C'^2}/U_c C_c^2$  is about 0.0002 – 0.0008, and that of  $\overline{C'^2}/C_c^2$  is about 0.036 – 0.044. Then, the ratio of  $\overline{u_x' C'^2}/U_c C_c^2$  to  $\overline{C'^2}/C_c^2$  ranges from 0.0005 to 0.002. Although Eq. (3.8) is for the normalized quantities,  $\mathbf{u}^*$  and  $C^*$ , we will assume here that turbulent parameters of normalized quantities are comparable to those of  $\mathbf{u}'$  and  $C'$ . Thus, we conclude that  $\overline{u_x^* C^*}/x_o$  is also negligible.

Next,  $D C^*/x_o^2 \ll U_c C^*/x_o$  for high Reynolds number and/or high Schmidt number flows, where the Schmidt number is defined as  $Sc \equiv \nu/D$ . The ratio  $U_c x_o/D$  is proportional to the jet Péclet number,  $Pe_D = Re_D \cdot Sc = U_o d/D$ , based on the exit nozzle velocity,  $U_o$ , and the nozzle diameter,  $d$  [55]. Similarly,  $\frac{D}{x_o} \frac{\partial C^*}{\partial x} \ll \mathbf{u}^* \cdot \nabla C^*$ . The ratio of the two terms is also of the same magnitude as the Péclet number.

With these simplifications, the only terms significantly contributing to the scalar variance are  $\frac{U_c}{x_o} C^*$  and  $\frac{C_c}{x_o} u_x^*$ . Thus, only these two terms are retained on the right-hand side of the governing equation for the passive scalar:

$$\frac{\partial C^*}{\partial t} + \mathbf{u}^* \cdot \nabla C^* - \nabla \cdot (D \nabla C^*) = \frac{U_c}{x_o} C^* + \frac{C_c}{x_o} u_x^*. \quad (3.9)$$

Under the assumption of statistical homogeneity, we obtain the scalar variance equation from Eq. (3.9):

$$\frac{d\overline{C^{*2}}}{dt} = -\overline{\chi} + 2\frac{U_c}{x_o}\overline{C^{*2}} + 2\frac{C_c}{x_o}\overline{u_x^*C^*}, \quad (3.10)$$

where  $\chi \equiv 2D\nabla C^* \cdot \nabla C^*$  is the scalar dissipation rate. By construction, ensemble-averaged quantities should be statistically stationary in the considered region. Then, Eq. (3.10) becomes

$$\overline{\chi} = 2\frac{U_c}{x_o}\overline{C^{*2}} + 2\frac{C_c}{x_o}\overline{u_x^*C^*}. \quad (3.11)$$

### 3.2.2 Properties of the forcing term

This current forcing term,  $\frac{U_c}{x_o}C^* + \frac{C_c}{x_o}u_x^*$ , is the result of applying the physical laws of a practical turbulent flow. The mean velocity and scalar profiles of a round jet, Eq. (2.13), (2.14), and (3.7), have been used during the derivation. The target experiment determines the coefficients of the source terms with its  $U_c$ ,  $C_c$ , and  $x_o$  values. They control the magnitudes and characteristics of scalar turbulent quantities in a 3D box, which should be similar to those of a round jet on the centerline.

This forcing term is also a combination of two previously existing methods: the linear scalar forcing (LS) and mean gradient forcing (MG).  $\frac{U_c}{x_o}C^*$  is linear to a scalar like LS, and  $\frac{C_c}{x_o}u_x^*$  is linear to a velocity like MG. Although the coefficients are arbitrary for the original MG and LS terms, they have the same forms as the current forcing term. It should be noted that this similarity is only a result of applying the physics of a practical flow.

### 3.2.3 Dimensional analysis

There are four input parameters for the simulations: the coefficients for the forcing terms,  $U_c/x_o$  and  $C_c/x_o$ , the domain width  $L_x$ , and viscosity  $\nu$ . These four parameters control the outcomes of the simulations, such as  $\overline{C^{*2}}$ ,  $\overline{u_x^*C^*}$ , or  $\overline{\chi}$ . It is important to note that these three quantities are not independent and are related through the scalar variance equation, Eq. (3.11). Table 3.1 summarizes the inputs and outputs, and their units.  $T$  represents a time unit;  $L$ , a length unit; and  $\theta$ , a scalar unit.

We can apply Buckingham Pi theorem to a set of four inputs and one outcome. For example, there exists a function  $g$  of relating  $\overline{C^{*2}}$  to the four input parameters:

$$g\left(\overline{C^{*2}}, \frac{U_c}{x_o}, \frac{C_c}{x_o}, L_x, \nu\right) = 0. \quad (3.12)$$

Table 3.1: Inputs and outputs of DNS

Input	$\frac{U_c}{x_o}$ [ $T^{-1}$ ]	$\frac{C_c}{x_o}$ [ $\theta L^{-1}$ ]	$L_x$ [ $L$ ]	$\nu$ [ $L^2 T^{-1}$ ]
Output	$\overline{C^{*2}}$ [ $\theta^2$ ]	$\overline{u_x^* C^*}$ [ $\theta L T^{-1}$ ]	$\overline{\chi}$ [ $\theta^2 T^{-1}$ ]	

We suggest two non-dimensional groups:

$$\pi_1 \equiv \frac{\overline{C^{*2}}}{(C_c/x_o)^2 L_x^2}, \quad (3.13)$$

$$\pi_2 \equiv \frac{(U_c/x_o) L_x^2}{\nu}. \quad (3.14)$$

$\pi_2$  is proportional to  $\text{Re}_D$ , because  $L_x = 0.399x_o$  [49], and  $U_c x_o/\nu$  is proportional to  $\text{Re}_D$  [55], as discussed in Sec. 3.2.1. Then, by Buckingham Pi theorem,

$$\overline{C^{*2}} = \alpha_1 (\text{Re}_\lambda) \left(\frac{C_c}{x_o}\right)^2 L_x^2. \quad (3.15)$$

$\alpha_1$  is a scaling coefficient, which may be a function of the Reynolds number.  $\text{Re}_D$  is replaced by  $\text{Re}_\lambda$ , because it is found that  $\text{Re}_\lambda \propto \text{Re}_D^{1/2}$  for turbulent round jets [60, 72].

A similar procedure is used to suggest the following relation for  $\overline{u_x^* C^*}$ :

$$\overline{u_x^* C^*} = \alpha_2 (\text{Re}_\lambda) \left(\frac{U_c}{x_o}\right) \left(\frac{C_c}{x_o}\right) L_x^2. \quad (3.16)$$

This suggestion comes from Eq. (3.15) and the fact that  $\sqrt{\overline{u_x^{*2}}} \propto (U_c/x_o) L_x$  from Eq. (2.32).

The final relation is for  $\overline{\chi}$ :

$$\overline{\chi} = \alpha_3 (\text{Re}_\lambda) \left(\frac{U_c}{x_o}\right) \left(\frac{C_c}{x_o}\right)^2 L_x^2. \quad (3.17)$$

This relation comes from Eq. (3.11), (3.15), and (3.16). Sec. 3.3 will examine the three coefficients,  $\alpha_1$ ,  $\alpha_2$ , and  $\alpha_3$ .

Finally, since  $L_x = 0.399x_o$ , the ratios  $\overline{C^{*2}}/C_c^2$ ,  $\overline{u_x^* C^*}/(U_c C_c)$ , and  $\overline{\chi}/(U_c C_c^2)$  should only depend on the Reynolds number. In other words, after appropriate normalizations, the turbulent characteristics should only be determined by the Reynolds number.

### 3.3 Results

#### 3.3.1 Simulation procedure

The governing equations, Eq. (2.23-2.25), and (3.9), are solved using the NGA code [61]. The resulting velocity field is, thus, the same one introduced in Chapter 2.

The initial velocity and scalar fields are randomly generated, following the method used by Eswaran and Pope [19]. The velocity fields are subject to the continuity constraint and conformed to a specified Passot-Pouquet energy spectrum [62]. The scalar fields are produced in a similar manner. A detailed explanation can be found in [63]. As mentioned in Sec. 3.1, only unity Schmidt number simulations are considered in the present work. The Courant-Friedrichs-Lewy condition,  $CFL \leq 0.9$ , has been imposed for all the simulations in the current paper.

The procedure of conducting the direct numerical simulation (DNS) in the current investigation can be summarized as follows:

- Find the centerline velocity  $U_c$ , centerline scalar  $C_c$ , and the axial location  $x_o$  of the target experiment
- Use  $U_c/x_o$  and  $C_c/x_o$  to determine the source term for the DNS
- Use  $x_o$  to determine the length of the DNS cubic box,  $L_x$
- Perform the DNS in a triply periodic configuration with the target  $\nu = D$

As in our previous work,  $L_x = 0.399x_o$  is used to match the integral length scale with a given target experiment; a detailed analysis can be found in Sec. 2.3.4. The number of grid points can be determined by the following equation, which is adopted from Eq. (2.41):

$$N \geq \frac{2.0}{15^{\frac{1}{4}}\pi} \frac{L_x}{l} \text{Re}_\lambda^{\frac{3}{2}}. \quad (3.18)$$

The resolution  $\kappa_{max}\eta_k \geq 2.0$  is used to obtain accurate scalar statistics.

Six DNS have been performed with  $Sc = 1$ , as shown in Table 3.2, with the bounded cubic Hermite polynomial (BCH) scalar transport scheme [73]. The target experiment is a slightly heated turbulent air jet in [31]. However, since its Reynolds number is too high, we have applied lower  $U_c$  values for our simulations to decrease the Reynolds numbers.

Table 3.2: Relevant parameters of the target experiments and the corresponding simulations

	Target experiments				Simulation parameters			
	$U_c/x_o$	$C_c/x_o$	$\nu = D$	$Re_D$	$L_x$	$\kappa_{max}\eta_k$	$N$	$Re_\lambda$
SCL1	0.0212	2.41	$1.64 \times 10^{-5}$	600	0.649	2.0	64	32
SCL2	0.0531	2.41	$1.64 \times 10^{-5}$	1500	0.649	2.0	128	51
SCL3	0.134	2.41	$1.64 \times 10^{-5}$	3900	0.649	2.0	256	81
SCL4	0.230	2.41	$1.64 \times 10^{-5}$	6700	0.649	2.0	384	107
SCL5	0.339	2.41	$1.64 \times 10^{-5}$	9800	0.649	2.0	512	129
SCL6	0.852	2.41	$1.64 \times 10^{-5}$	25000	0.649	2.0	1024	205

For each time-averaged quantity shown in this work, averaging uncertainty is presented as an error bar. This uncertainty quantification method is explained in details in Appendix A. For the accurate examination of time-averaged values, the simulations have to run for a sufficiently long time. However, we could not run SCL6 long enough, due to its high computational cost. As a result, SCL6 has been omitted from analysis in Sec. 3.3.2 and 3.3.4.

### 3.3.2 Scaling coefficient

In this section, we report the values of  $\alpha_1$ ,  $\alpha_2$ , and  $\alpha_3$  by using SCL1-5, for the three relations, Eq.(3.15-3.17), in which time-averaged values of volume-averaged quantities are used in the place of ensemble-averaged ones. This is justified because of the statistically homogeneous and statistically stationary nature of the flow.

The results are plotted as a function of  $Re_\lambda$  in Fig. 3.1. Each coefficient appears to approach a plateau rapidly, as the Reynolds number increases. The lack of an inertial range for low Reynolds number flows might be the cause for the low coefficient values. An exponential fitting is provided to estimate the high Reynolds number limit. The dashed lines are weighted least-squares fits of a functional form  $h(Re_\lambda) = a_1 - a_2 \exp(-a_3 Re_\lambda)$ . It is found that

$$\alpha_1 \rightarrow 1.60, \quad (3.19)$$

$$\alpha_2 \rightarrow 0.453, \quad (3.20)$$

$$\alpha_3 \rightarrow 3.72. \quad (3.21)$$

As stated in Sec. 3.2.3, the three coefficients are related by the scalar variance equation under statistical stationarity (Eq. (3.11)). More precisely, it can be deduced

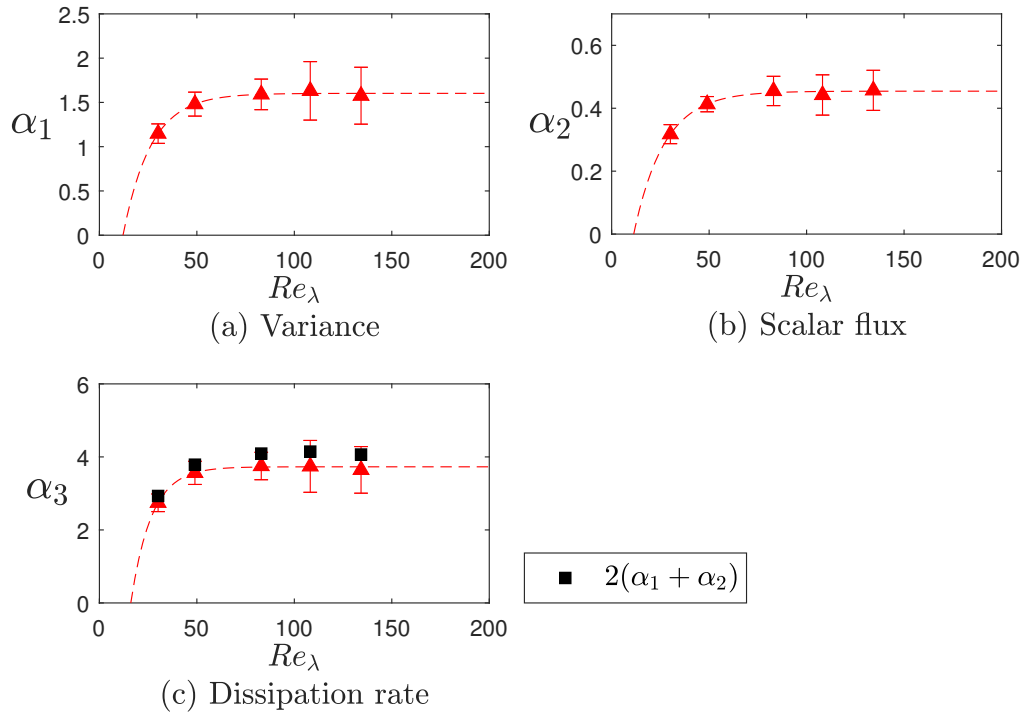


Figure 3.1: Scaling coefficients for the variance (a, Eq. (3.15)), the scalar flux (b, Eq. (3.16)), and the dissipation rate (c, Eq. (3.17)) from SCL1-5. The dashed lines are weighted least-squares fits of a functional form  $h(Re_\lambda) = a_1 - a_2 \exp(-a_3 Re_\lambda)$ .

that

$$\alpha_3 \approx 2(\alpha_1 + \alpha_2). \quad (3.22)$$

Figure 3.1 (c) shows  $2(\alpha_1 + \alpha_2)$ . There is a small difference between  $\alpha_3$  and  $2(\alpha_1 + \alpha_2)$ , which is the inevitable consequence of numerical dissipation of the scalar transport scheme.

### 3.3.3 Instantaneous mixing structures

To study the impact of the source terms, three scalars were transported simultaneously for all simulations: the first scalar with the original jet centerline (JC) source terms,  $\frac{U_c}{x_o} C^* + \frac{C_c}{x_o} u_x^*$ ; the second scalar with only the linear scalar (LS) term with the target variance  $\sigma_t^2 = 0.001$ ,  $\frac{U_c}{x_o} C^*$ ; and the third scalar with only the mean gradient (MG) term,  $\frac{C_c}{x_o} u_x^*$ . The contours of these three scalar fields from SCL2 are shown in Fig. 3.2. Each plot uses 10 number of contour levels from its own minimum value (dark blue) to maximum value (bright yellow).

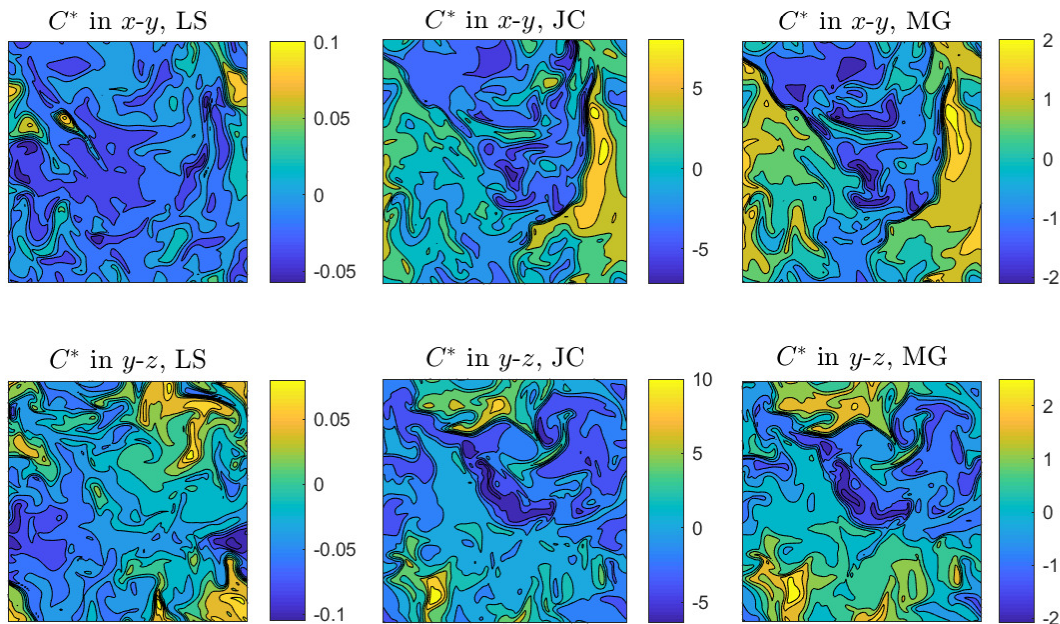


Figure 3.2: Contours of scalar fields from SCL2 in  $xy$  (top) and  $yz$  (bottom) planes with three different forcing methods: the linear scalar (LS) forcing (left), the jet centerline (JC) forcing (middle), and the mean gradient (MG) forcing (right).

Each plot shows a cross section in the middle of the simulation cubic box. The mixing structures are homogeneous for all plots, as expected. Although the three forcing methods produce different scalar statistics, as will be shown in Sec. 3.3.4, it is difficult to identify the difference visually from the contour plots. Also, the  $xy$  and  $yz$  planes do not display much difference for all three forcing methods; the structures seem isotropic as well.

The JC plots are highly similar to the MG plots, which is to be expected because one of the terms in the JC forcing method is a mean gradient term,  $\frac{C_c}{x_o} u_x^*$ . Since this term is shared by both JC and MG, there must be similarities in any instantaneous JC and MG scalar fields. However, they are not exactly the same, because there is another term in JC forcing, the linear scalar term. This LS term in JC forcing also leads to the increase of magnitude, as compared that of MG forcing. As seen in the contour color bars, the values of  $C^*$  in MG plots range from  $-2$  to about  $2$ , but those in JC plots range from about  $-6$  to about  $10$ .

For the scalars in LS plots, it is difficult to compare the magnitude against others, as the variance is imposed to be  $\sigma_t^2 = 0.001$  in LS forcing. As compared to MG

plots, the LS ones are much less similar to JC plots; there is much less correlation between the LS fields and the JC fields.

### 3.3.4 Validation against experimental data - scalar flux

Normalized scalar flux quantities,  $\langle\langle u_x^* C^* \rangle\rangle / \sqrt{\langle\langle u_x'^2 \rangle\rangle \langle\langle C'^2 \rangle\rangle}$ , have been calculated from simulations and compared against experiments. The equivalent experimental value is

$$\frac{\langle u_x' C' \rangle_t}{\sqrt{\langle u_x'^2 \rangle_t \langle C'^2 \rangle_t}} \Big|_{x=x_o}, \quad (3.23)$$

where  $\langle \cdot \rangle_t$  denotes time-averaging.

The scalar flux comparison is shown in Fig. 3.3. Experiments used for the comparison are summarized in Table 3.3. Darisse *et al.* [31] and Chevray & Tutu [74] both used slightly heated air (20°C above ambient). In these cases, the density ratio  $\rho_{jet}/\rho_{amb}$  is only about 0.99 [31]; therefore, the buoyancy effect is negligible. Anderson & Bremhorst [71], on the other hand, used highly heated air (118°C above ambient). In this case, the density ratio is around 0.72 [71]; however, the measurement used for this comparison was performed at the inertia dominated region. Therefore, all the air jet experiments in the referred table treated the fluid temperatures as passive scalars. In these cases, the Schmidt number is equivalent to the Prandtl number,  $Pr \equiv \nu/\alpha$ , where  $\alpha$  is the thermal diffusivity. High Schmidt number experiments are also listed for completeness, because the range of scalar flux values appears independent of Schmidt numbers.

$Re_\lambda = 1.3\sqrt{Re_D}$  has been applied to the experiments to convert  $Re_D$  to  $Re_\lambda$  [72]. There is some scatter in the published values ranging from 0.4 to 0.6 for all the experiments. However, there are no apparent trends.

As explained in Sec. 3.3.3, three different source terms were tested: JC, LS, and MG. Scalar flux values from these three different scalar fields are plotted. The error bars are only shown for the flux with the original source terms (red triangles), and were estimated using the numerator  $\langle\langle u_x^* C^* \rangle\rangle$  only. Once again, the simulations in this chapter have been performed with  $Sc = 1$ .

The scalar flux values from the current study seem fairly constant, independently of the Reynolds number. The mean of four scalar flux values with the original source terms,  $\frac{U_c}{x_o} C^* + \frac{C_c}{x_o} u_x^*$ , is about 0.52, which is expressed with the red dashed line in

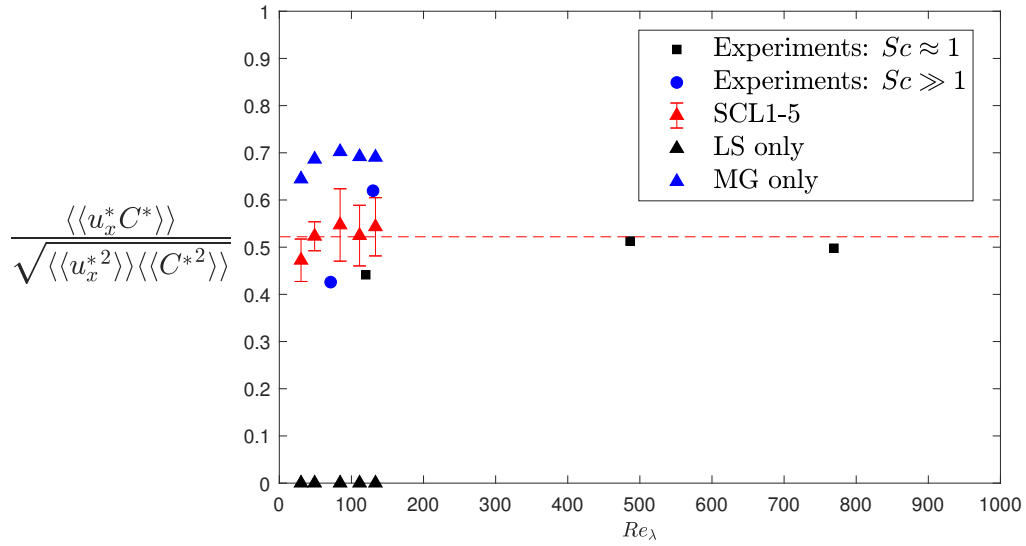


Figure 3.3: Normalized scalar flux  $\frac{\langle\langle u_x^* C^* \rangle\rangle}{\sqrt{\langle\langle u_x^{*2} \rangle\rangle \langle\langle C^{*2} \rangle\rangle}}$  and its corresponding experimental quantity. Round jet experiments used for the comparison are summarized in Table 3.3. The figure displays SCL1-5 results with the original jet centerline (JC) terms,  $\frac{U_c}{x_o} C^* + \frac{C_c}{x_o} u_x^*$  (red triangles); with only the linear scalar (LS) term,  $\frac{U_c}{x_o} C^*$  (black triangles); and with only the mean gradient (MG) term,  $\frac{C_c}{x_o} u_x^*$  (blue triangles). The mean of SCL1-5 values with the original forcing terms is 0.52, shown as the dashed red line.

Table 3.3: Round jet experiments used for the scalar flux comparison.

Author	$Re_D$	Sc or Pr	Fluid	Scalar
Anderson & Bremhorst [71]	7880	0.7	Air	Temperature
Darisse <i>et al.</i> [31]	140000	0.7	Air	Temperature
Chevray & Tutu [74]	350000	0.7	Air	Temperature
Webster <i>et al.</i> [59]	3000	2500	Water	Fluorescent dye (Rhodamine 6G)
Antoine <i>et al.</i> [75]	10000	2740	Water	Fluorescent dye (Rhodamine B)

Fig. 3.3. This value lies within the range of the reported experimental values. In contrast, the scalar flux  $\langle\langle u_x^* C^* \rangle\rangle$  is zero for LS forcing, because there is no term in the advection-diffusion equation that produces a correlation between the velocity

and the scalar. When the DNS is performed only with the MG term, the scalar flux is systematically larger than the largest experimental values.

### 3.3.5 Validation against experimental data - scaling exponent of scalar energy spectra

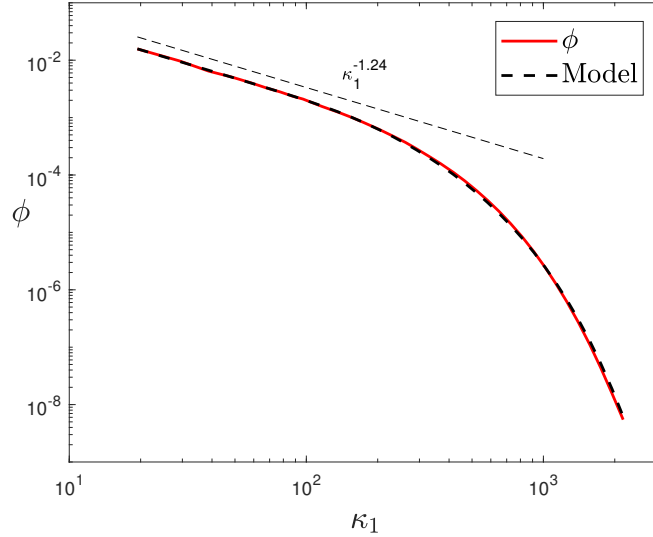


Figure 3.4: Scalar energy spectrum:  $\phi_c(\kappa_1)$  computed from SCL5 at  $\text{Re}_\lambda = 129$ , and its least-squares fit result with model spectrum, Eq. (3.25).

A scalar energy spectrum can be easily computed from the triply periodic DNS. The one-dimensional energy spectrum,  $\phi_c(\kappa_1)$ , is defined as:

$$\int_0^\infty \phi_c(\kappa_1) d\kappa_1 = \frac{1}{2} \langle C^{*2} \rangle, \quad (3.24)$$

where  $\kappa_1$  is the wavenumber in the longitudinal direction.  $\phi_c(\kappa_1)$  is the Fourier transform of the spatial correlation function  $\langle C^*(\mathbf{x}) \cdot C^*(\mathbf{x} + \mathbf{r}_1) \rangle$ , where  $\mathbf{r}_1$  is a vector in the longitudinal direction. An example of scalar energy spectra is shown in Fig. 3.4. It is computed from SCL5 at  $\text{Re}_\lambda = 129$ .

Our interest is to determine the scaling exponent  $n$  for the relation  $\phi_c \sim \kappa^{-n}$  in the inertial-convective subrange, and compare it against experiments. We use the following model spectrum:

$$\hat{\phi}_c(\kappa_1) = B_1 \kappa_1^{-n} \exp \left[ -B_2 \left( \left( (\eta_k \kappa_1)^4 + B_3^4 \right)^{\frac{1}{4}} - B_3 \right) \right], \quad (3.25)$$

where  $B_1$ ,  $B_2$ , and  $B_3$  are constants, and  $\eta_k = (\nu^3/\varepsilon)^{1/4}$  is the Kolmogorov length scale. This form of a function was used by Lee *et al.* to model a scalar spectrum [76]. The exponential part for the dissipation range is adopted from the kinetic energy model spectrum of Pope [53]. A least-squares fit is used over the spectrum with Eq. (3.25) to determine  $B_1$ ,  $B_2$ ,  $B_3$ , and  $n$ . For the example shown in Fig. 3.4,  $n$  is found to be 1.24 with this method. All of the fitting results are shown in Table 3.4. The scalar variance has been computed from  $\langle C^{*2} \rangle = \int 2\hat{\phi}_c d\kappa$ , as the spectrum is defined such that  $\int \phi_c(\kappa) d\kappa = \frac{1}{2}\langle C^{*2} \rangle$  in Eq. (3.25). The scalar dissipation rate has been computed from  $\chi = 2D|\nabla C'|^2 = 2D \int 2\kappa^2 \hat{\phi}_c d\kappa$ . These two parameters are compared against the actual values for the verification of fitting results.

Table 3.4: Least-squares fit results.

	$B_1$	$B_2$	$B_3$	$n$	$C_{\text{fit}}^2$	$C^2$	$\chi_{\text{fit}}$	$\chi$
SCL1	0.744	4.86	$1.21 \cdot 10^{-4}$	0.964	4.37	4.38	0.240	0.242
SCL2	0.843	3.85	0.0788	1.03	6.13	6.16	1.31	1.23
SCL3	0.492	5.37	0.106	1.15	3.38	3.40	1.32	1.35
SCL4	0.184	5.13	0.120	1.20	1.39	1.42	0.928	0.910
SCL5	0.650	5.40	0.110	1.24	4.11	4.13	3.81	3.82
SCL6	0.345	5.30	0.090	1.33	1.71	1.68	4.18	4.27

Table 3.5: Experiments used for the energy spectrum comparison.

Author	Flow	$Re_\lambda$	Sc or Pr	Fluid	Scalar
Dowling & Dimotakis [77]	Jet	260	1.0	Ar/C <sub>3</sub> H <sub>6</sub> mixture	C <sub>3</sub> H <sub>6</sub>
Duffet & Benaïssa [78]	Jet	290	0.7	Air	Temperature
Tavoularis & Corrsin [35]	Grid	242	0.7	Air	Temperature
Sreenivasan [79]	Wake of cylinder	175, 330, 350	0.7	Air	Temperature
Mestayer [80]	Boundary layer	616	0.7	Air	Temperature
Sreenivasan [79]	Atmospheric surface layer	1500	$\sim 1$	Air	Temperature
Pond [81]	Atmospheric surface layer	2000	$\sim 1$	Air	Temperature

The  $n$  values computed from SCL1-6 are displayed in Fig. 3.5. They show a clear

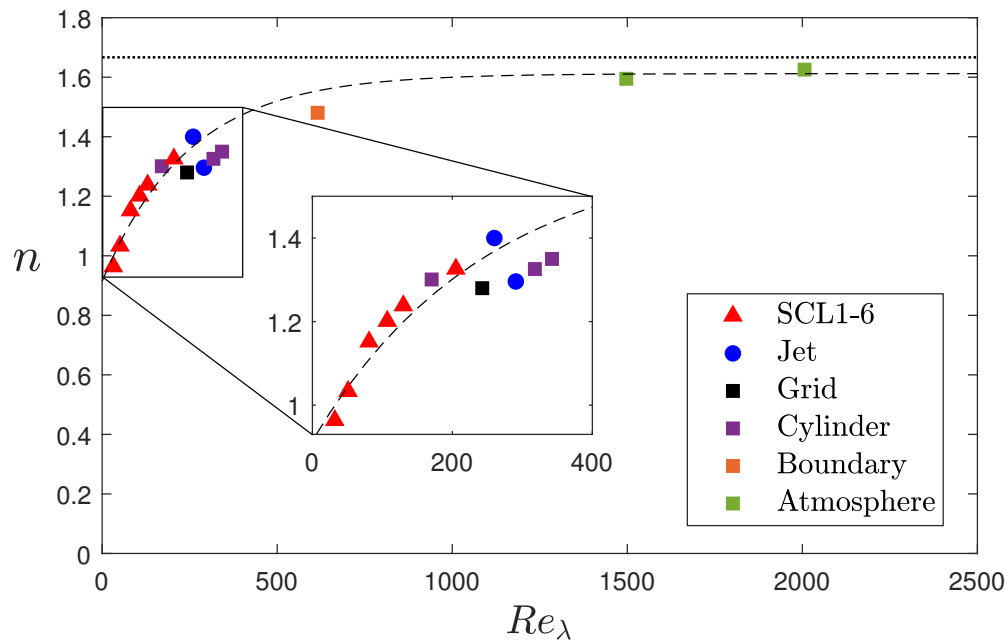


Figure 3.5: Scaling exponent  $n$  for the scalar energy spectra,  $\phi_c \sim \kappa^{-n}$ , calculated from SCL1-6. Experiments used for the comparison are summarized in Table 3.5. The dashed line is a weighted least-squares fit of an exponential function, using all the presented data. The dash-dot line shows  $n = 5/3$ .

trend of increasing scaling exponents with increasing  $Re_\lambda$ . Scaling exponents of two jet experiments are also plotted. Dowling & Dimotakis [77] estimated their slope to be  $7/5$  by simply comparing the spectrum against a straight line with a slope  $7/5$ . For the spectrum in Duffet & Benaïssa [78], we applied our least-squares fit method to find the scaling exponent. Although our simulations do not match the  $Re_\lambda$  of the two jet experiments presented in this work exactly, the result from SCL6 is comparable to them.

Scaling exponents from other various shear flows are also shown in Fig. 3.5 for an additional comparison. The scaling exponents of these shear flows were all measured by Sreenivan [79], which compensated the spectra with  $\kappa^n$  to find the zero slope in the inertial subrange. All the experiments used for this comparison summarized in Table 3.5. Experiments with  $Sc = 0.7$  appear to be in the same increasing curve with those with unity Schmidt numbers.

The dashed line is a weighted least-squares fit of an exponential function, using all the simulations and experiments data. Although it is difficult to conclude from this comparison that round jets display the same scalar energy spectra as other shear

flows, it should be noted that the  $n$  values from our simulations, jet experiments, and other shear flows are along the similar increase curve.

### 3.4 Discussion

In this section, we examine the effects of the velocity forcing scheme on the statistics of the scalar field. The numerical computations presented in the current study apply the jet centerline (JC) velocity forcing on velocity fields and the JC scalar forcing on the scalar fields.

#### 3.4.1 Simulations with different velocity forcing terms

The forcing term for the JC velocity method is anisotropic and linear with the velocity components, as shown in Eq. (2.21) and (2.22). We will denote the forcing coefficient  $U_c/2x_o$  as  $A$ . Then, the forcing terms in the original JC velocity method can be expressed as

$$\mathbf{f}_u = f_x u_x^* \hat{\mathbf{i}} + f_y u_y^* \hat{\mathbf{j}} + f_z u_z^* \hat{\mathbf{k}} \quad (3.26)$$

$$= 2A u_x^* \hat{\mathbf{i}} + A u_y^* \hat{\mathbf{j}} + A u_z^* \hat{\mathbf{k}}. \quad (3.27)$$

Additional DNS have been performed with different coefficients for the linear velocity forcing terms, as shown in Table 3.6. Each simulation still uses the same JC scalar forcing.

The baseline case is SCL1 from Table 3.2. Iso1 is isotropic, while Iso2 imposes a stronger anisotropy than SCL1. Mag1-2 use the same 2 : 1 : 1 ratio for the forcing coefficients, but Mag1 is smaller and Mag2 is larger in forcing magnitudes than SCL1. Iso1 and Mag1 are found to be unstable; their statistical values, such as volume-averaged variance and dissipation, increase exponentially over time. The stability issue will be discussed in Sec. 3.4.4.

Table 3.6: Forcing coefficients for the linear velocity forcing terms for simulations with  $A = U_c/2x_o$ .

	$f_x$	$f_y$	$f_z$	$\text{Re}_\lambda$	$r_\chi$	$2 \frac{U_c}{x_o} \frac{\langle\langle \varepsilon \rangle\rangle}{\langle\langle k \rangle\rangle}$
SCL1	2A	A	A	32	1.5	1.2
Iso1	A	A	A	22	1.8	2.1
Iso2	4A	A	A	49	1.3	0.76
Mag1	A	A/2	A/2	22	2.0	2.6
Mag2	4A	2A	2A	43	1.2	0.63

### 3.4.2 Time scale ratio

Let us define the time scale ratio as

$$r_\chi \equiv \frac{\overline{\chi}/C^{*2}}{\overline{\varepsilon}/k}. \quad (3.28)$$

For simulations with the proposed JC scalar forcing, we can deduce from Eq. (3.15) and (3.17) in Sec. 3.2.3 that

$$\frac{\overline{\chi}}{C^{*2}} = \frac{\alpha_3 U_c}{\alpha_1 x_o}. \quad (3.29)$$

Also, for the JC velocity forcing, we can find from Eq. (2.32) and (2.33) that

$$\frac{\overline{\varepsilon}}{k} = \left(1 + \frac{\langle\langle u_x^{*2} \rangle\rangle}{\langle\langle \mathbf{u}^{*2} \rangle\rangle}\right) \frac{U_c}{x_o}, \quad (3.30)$$

with the assumption that the ensemble-averaged quantities are equal to their expected values.

The time scale ratio,  $r_\chi$ , for the simulations with the original JC velocity and the proposed JC scalar forcing will be

$$r_\chi = \frac{\alpha_3/\alpha_1}{1 + \frac{\langle\langle u_x^{*2} \rangle\rangle}{\langle\langle \mathbf{u}^{*2} \rangle\rangle}}. \quad (3.31)$$

From the exponential fits in Sec. 3.3.2,  $r_\chi$  should be around 1.5 for any  $\text{Re}_\lambda$  larger than 25.

The ratios  $r_\chi$  from SCL1-5, Iso1-2, and Mag1-2 are displayed in Fig. 3.6. Once again, ensemble-averaging, denoted as  $\overline{\cdot}$ , in Eq. (3.28) has been replaced with time-averaging of volume-averaged quantities,  $\langle\langle \cdot \rangle\rangle$ , to find  $r_\chi$  for this plot.

As expected from Eq. (3.31),  $r_\chi$  of SCL1-5 is around 1.5. The ratios  $r_\chi$  of Iso2 and Mag2 are smaller than those of SCL1-5 by about 18% and 25%, respectively. Nevertheless, the ratio of scalar to velocity time scales is fairly independent of the velocity forcing scheme (both magnitude and anisotropy).

### 3.4.3 Effect of velocity forcing on scalar flux

Normalized scalar flux quantities,  $\langle\langle u_x^* C^* \rangle\rangle / \sqrt{\langle\langle u_x^{*2} \rangle\rangle \langle\langle C^{*2} \rangle\rangle}$ , have been computed from SCL1-5, Iso1-2, and Mag1-2, as shown in Fig. 3.7. The flux values of Iso2 and Mag2 are larger than those of SCL1-5, with a maximum deviation of about 18% for Mag2. In clear contrast,  $\langle\langle u_x^* C^* \rangle\rangle / \sqrt{\langle\langle u_x^{*2} \rangle\rangle \langle\langle C^{*2} \rangle\rangle}$  of Iso1 and Mag1 are

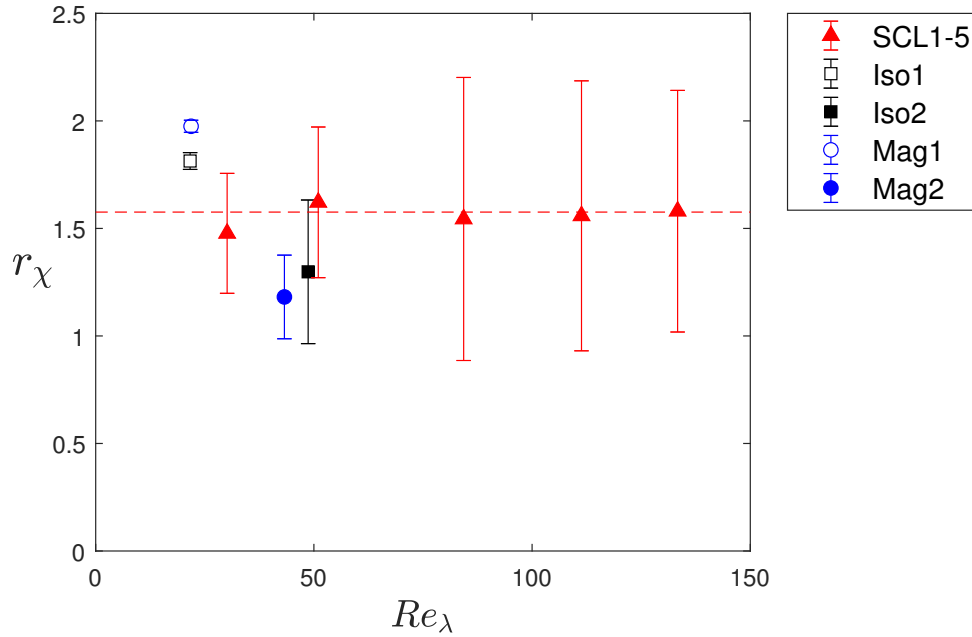


Figure 3.6: Time scale ratio  $r_\chi$  (Eq. (3.28)) from SCL1-5, Iso1-2, and Mag1-2. The mean of SCL1-5 values is shown as the dashed red line.

essentially zero, which indicates that velocity and scalar fields remain uncorrelated, despite the MG term in the transport equation. This phenomenon is actually caused by the instability of Iso1 and Mag1 simulations and is discussed next.

### 3.4.4 Stability of scalar equation

The stability of our simulation system can be examined by analyzing the scalar variance equation. Using Eq. (3.28), the equation for the volume-averaged scalar variance  $\langle C^{*2} \rangle$  can be expressed as

$$\frac{d\langle C^{*2} \rangle}{dt} = -\frac{\langle \varepsilon \rangle}{\langle k \rangle} \left( r_\chi - 2 \frac{U_c \langle k \rangle}{x_o \langle \varepsilon \rangle} \right) \langle C^{*2} \rangle + 2 \frac{C_c}{x_o} \langle u_x^* C^* \rangle. \quad (3.32)$$

If  $r_\chi > 2 \frac{U_c \langle k \rangle}{x_o \langle \varepsilon \rangle}$ , the solution is stable; the two terms on the right-hand side (RHS) become balanced, and the system finds a statistically stationary state. However, if  $r_\chi < 2 \frac{U_c \langle k \rangle}{x_o \langle \varepsilon \rangle}$ , the solution is unstable; the scalar variance keeps increasing and does not reach a statistically stationary state.

Figure 3.8 displays the ratios of volume-averages,  $2 \frac{U_c \langle k \rangle}{x_o \langle \varepsilon \rangle}$ , from SCL1, Iso1-2, and Mag1-2, plotted as a function of normalized time. As a reminder, for passive

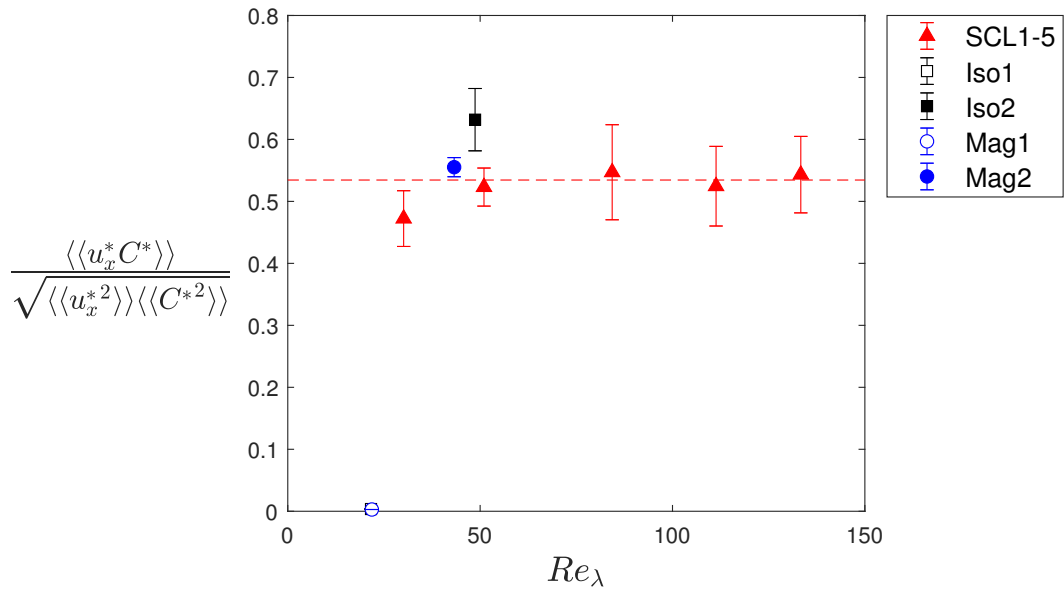


Figure 3.7: Normalized scalar flux from SCL1-5, Iso1-2, and Mag1-2. The mean of SCL1-5 values is shown as the dashed red line.

scalars, this ratio is only a result of the velocity forcing scheme and is not influenced by the scalar field. Table 3.6 reports the time-averages of  $r_\chi$  and  $2 \frac{U_c \langle k \rangle}{x_o \langle \varepsilon \rangle}$  for each simulation.

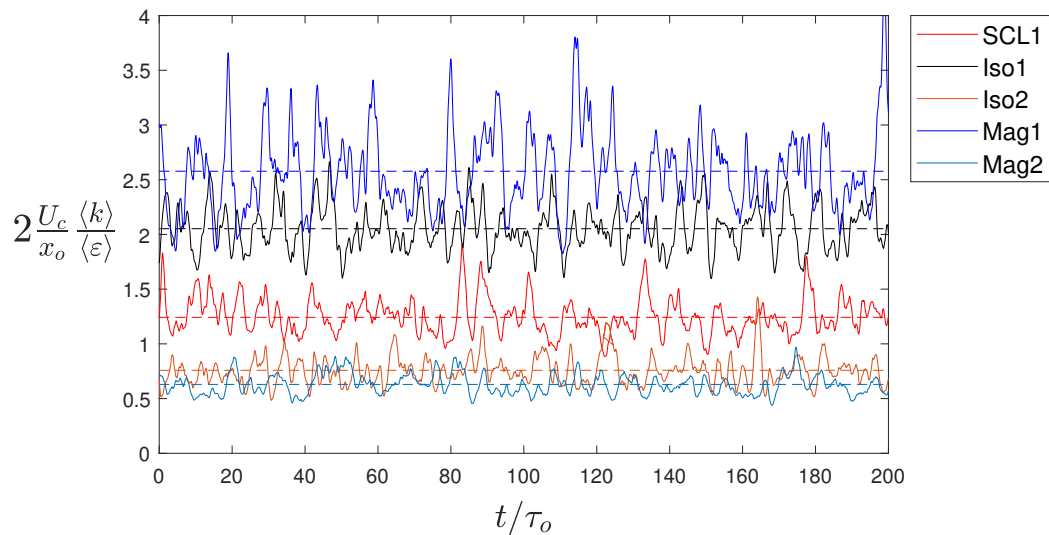


Figure 3.8: Volume-averaged ratio,  $2 \frac{U_c \langle k \rangle}{x_o \langle \varepsilon \rangle}$ , from SCL1, Iso1-2, and Mag1-2, plotted as a function of the time normalized by the eddy time scale,  $\tau_o = k_o/\varepsilon_o$ . The horizontal dashed line indicates the time-averaged value of each simulation.

As expected from Eq. (3.32), for stable simulations, SCL1, Iso2, and Mag2, the time-averaged value of  $2 \frac{U_c \langle k \rangle}{x_o \langle \varepsilon \rangle}$  is smaller than its respective  $r_\chi$ . On the other hand, for unstable simulations, Iso1 and Mag1, the time-averaged value of  $2 \frac{U_c \langle k \rangle}{x_o \langle \varepsilon \rangle}$  is larger than its respective  $r_\chi$ . For unstable Iso1 and Mag1, the velocity-scalar correlation cannot be developed, as shown in Sec. 3.4.3, because the scalar field cannot reach a statistically stationary state.

We have found that the velocity forcing affects the scalar statistics and the stability of the simulations. It also shows the need for an appropriate relation between the velocity and scalar forcings. Simulations with the proposed JC scalar forcing must use the JC velocity forcing, in order to produce the proper turbulence of a round jet on the centerline. This inherent relation ensures that the simulations are stable and produce the correct scalar turbulence.

### 3.5 Summary

Existing scalar forcing schemes successfully sustain the variance, but they do not represent specific practical flows. In contrast, the forcing method derived in this work is based on the physical properties of a turbulent round jet, which are applied to the scalar transport equation. A normalization on the scalar has also been applied to derive the source term to be used in a triply periodic box. The derivation result is a combination of two previously existing methods, namely mean gradient (MG) and linear scalar (LS).

A dimensional analysis was introduced to seek relations between the inputs and outputs of our simulations with jet centerline (JC) velocity and JC scalar forcing. It was found that normalized scalar statistics, such as variance, flux, and dissipation rate, should only be a function of Reynolds number. Our simulation results indicate that such quantities approach constant values as the Reynolds number increases.

Normalized scalar flux quantities and scaling exponents of scalar energy spectra were compared against experiments. Unfortunately, only a small number of data is available in the literature, and some scatter among the experimental values exists. Nevertheless, the simulation results are comparable to the round jet measurements.

The effects of velocity forcing schemes on the scalar fields were also investigated by altering the velocity forcing coefficients while maintaining the same JC scalar forcing. It was observed that velocity forcing had a slight influence on the resulting time scale ratio  $r_\chi$  and scalar flux. More importantly, however, changing velocity forcing terms may result in unstable scalar fields even under the same scalar forcing.

This finding reinforces our argument that the velocity and scalar forcing schemes cannot be selected independently from each other.

The current study devised the first scalar forcing technique that replicates the mixing nature in a practical flow. It proves the possibility of creating a realistic mixing environment in a simple 3D periodic domain instead of computing an entire flow. The mathematical methodology is not limited to turbulent round jet centerlines and should be applied to different flow configurations in future studies.

## Chapter 4

### EFFECTS OF SCHMIDT NUMBER ON SCALAR STATISTICS UNDER JET CENTERLINE FORCING

The behaviors of passive scalars can vary significantly, depending on their diffusivity. One way to quantify the extent of diffusion is to use the Schmidt number, defined as the ratio of fluid viscosity to scalar diffusivity,  $Sc = \nu/D$ .

Unity Schmidt number passive scalars diffuse comparatively rapidly, and thus the mixing process is fast and simple. On the other hand, high Schmidt number scalars display complex interactions of convection, diffusion, and turbulence.

Examples of the high Schmidt scalars are aerosols like soot, metal oxides, and dust; their Schmidt numbers may reach  $O(10^4)$  if the particle diameter is as large as 100 nm [82]. In water, high  $Sc$  scalars can be algae ( $O(10)$ ) [83], dissolved gases ( $O(10^2)$ ) [84], or dye ( $O(10^3)$ ) [75]. These small particles may be generated by a variety of natural phenomena and combustion devices, and they are transported in turbulent flow fields. Thus, it is important to understand the behaviors of high Schmidt number passive scalars in a turbulent mixing process.

#### 4.1 Background

According to Kolmogorov's similarity hypothesis [42], the local statistics of any turbulent small-scale motion have a universal form that is uniquely determined by two parameters,  $\nu$  and  $\varepsilon$ , at sufficiently high Reynolds number. As a result of dimensional analysis with  $\nu$  and  $\varepsilon$ , the Kolmogorov velocity scale,  $u_k = (\nu\varepsilon)^{1/4}$ , and length scale,  $\eta_k = (\nu^3/\varepsilon)^{1/4}$ , can be found. These scales represent the smallest scales present in the flow, at which the energy is dissipated. Also, they are the scales at which the Reynolds number is equal to 1, such that

$$\text{Re} = \frac{u_k \eta_k}{\nu} = 1. \quad (4.1)$$

The inertial subrange of typical kinetic energy spectra is the wavenumber region,  $O(1/L) < \kappa < O(1/\eta_k)$ , where  $L$  is the scale at which energy is supplied to the turbulence. It is described in Fig. 4.1 that shows a kinetic energy spectrum  $\phi_k(\kappa)$ , defined in Eq. (2.63), in log-log scales. The kinetic energy spectrum begins to dissipate at  $\kappa > O(1/\eta_k)$ .

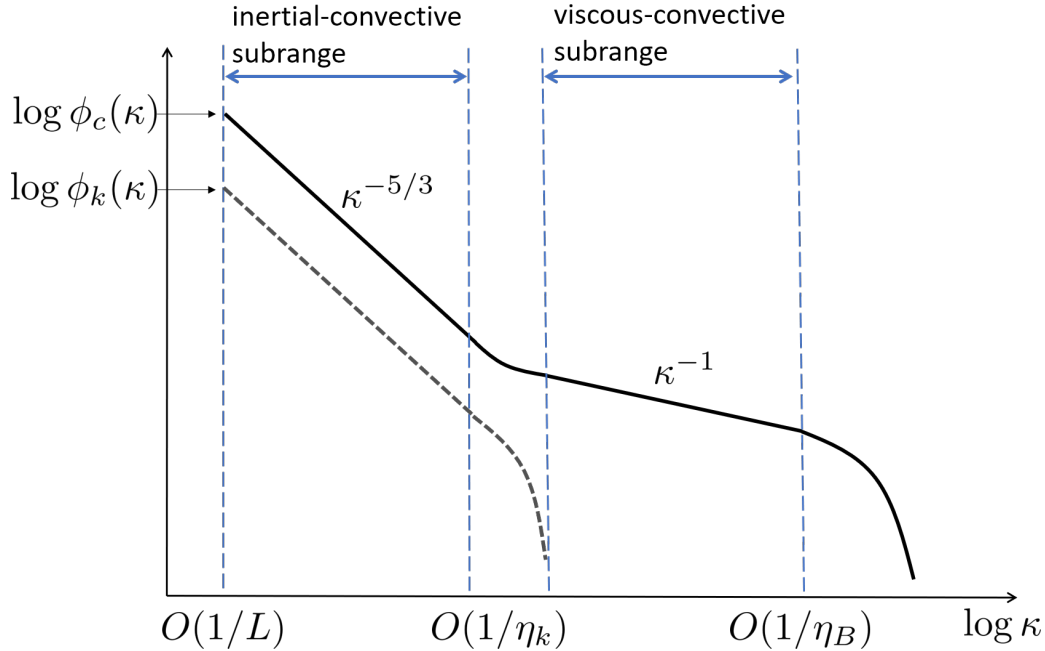


Figure 4.1: A schematic diagram of a scalar energy spectrum,  $\phi_c(\kappa)$ , and a kinetic energy spectrum,  $\phi_k(\kappa)$ , in log-log scales.

Oboukhov [85] and Corrsin [86] later extended Kolmogorov's analysis to scalar fields, to suggest the analogous length scale,  $(D^3/\varepsilon)^{1/4}$ . However, Batchelor [87] realized that the velocity field at scales smaller than the viscous cutoff,  $\eta_k$ , should be extremely smooth, and that the velocity gradients should be approximately uniform. Then, any distribution of passive scalars within this small material element of fluid should be at a pure straining motion. Therefore, he assumed that the rate-of-strain,  $\gamma = (\varepsilon/\nu)^{1/2}$ , should be an important parameter for small-scale scalar statistics, instead of  $\varepsilon$ . As a result, the Batchelor length scale, which is an analogous term to the Kolmogorov length scale, was found to be  $\eta_B = (D/\gamma)^{1/2} = (D^2\nu/\varepsilon)^{1/4} = \eta_k/\text{Sc}^{1/2}$ .

In [87], Batchelor explains that when  $D$  is smaller than  $\nu$ , the scalar energy spectrum extends beyond  $1/\eta_k$ , up to  $(\varepsilon/\nu D^2)^{1/4}$ . The ratio of  $\nu$  to  $D$  is the Schmidt number, and the reciprocal of the maximum wavenumber is the Batchelor length scale. Thus, as the Schmidt number increases,  $\eta_B$  decreases. Figure 4.1 shows a schematic diagram of  $\phi_c(\kappa)$ , defined in Eq. (3.24), in log-log scales. The high Sc scalar energy spectrum has a viscous-diffusive subrange at  $\kappa > O(1/\eta_B)$ . Because of the difference in length scales, a subrange between  $O(1/\eta_k)$  and  $O(1/\eta_B)$  emerges. This region is called the viscous-convective subrange, in which the viscous effects exceed the inertial effects.

Experiments have been conducted for high Reynolds numbers and high Schmidt numbers [59, 75, 88–93]. However, they cannot measure small scalar fluctuations close to the Batchelor length scale. Simulations with high Schmidt numbers (up to  $Sc = 1024$ ) have been performed [8, 9, 94–97], but only at low Reynolds numbers ( $Re_\lambda = 8$ ). The reason for this lack of simulation data is the high cost of direct numerical simulations (DNS) for high Schmidt number scalars. As the Schmidt number increases, DNS need to resolve much smaller length scales for the scalars. Thus, large-eddy simulations (LES) may be more appropriate, since LES reduce the cost of computation by modeling the small scale dynamics. LES have been used for many studies dealing with scalars [98–103], but they predominantly focused on unity Schmidt number scalars. Therefore, there is a need for the development of different simulation methods for high Schmidt scalars. One of the purposes for the high  $Sc$  and high  $Re$  simulations is to examine the scalar energy spectra.

Batchelor [87] assumed that small scalar fluctuations under high  $Sc$  environments would experience a velocity field of uniform straining. With the assumption of uniform rate-of-strain, he derived the following expression for an energy spectrum in the viscous-convective subrange for high  $Sc$  scalar fields:

$$\hat{\phi}_c(\kappa) = C_B \chi \left(\frac{\nu}{\varepsilon}\right)^{\frac{1}{2}} \kappa^{-1} \exp[-C_B \kappa^2 \eta_B^2], \quad (4.2)$$

where  $C_B$  is a constant.

Subsequently, Kraichnan [104] extended this analysis by incorporating the intermittency of rate-of-strain to find changes in the dissipative region:

$$\hat{\phi}_c(\kappa) = C_k \chi \left(\frac{\nu}{\varepsilon}\right)^{\frac{1}{2}} \kappa^{-1} \left(1 + \kappa \eta_B \sqrt{6C_k}\right) \exp\left[-\sqrt{6C_k} \kappa \eta_B\right], \quad (4.3)$$

where  $C_k$  is a constant.

There have been many attempts to verify the scaling  $\phi_c \sim \kappa^{-1}$  in the viscous-convective subrange for high  $Sc$  scalars. However, the results have been inconsistent in regards to the  $\kappa^{-1}$  scaling. Experiments conducted in oceans [88], shear layers [89], and turbulent jets [90, 91] have not shown  $\kappa^{-1}$  scaling in high Schmidt number scalars, but a recent experiment with  $Sc \sim 10^4$  [93] has displayed the  $\kappa^{-1}$  scaling. On the other hand, numerical simulations have shown  $\kappa^{-1}$  scaling [8, 9, 94, 95, 97], for low their Reynolds and Schmidt numbers. Unfortunately at the moment, no simulations at high  $Re$  and  $Sc$  have validated Batchelor's theory. There is a need to develop numerical schemes that can simulate high  $Sc$  and high  $Re$  scalar mixing

of a practical flow. One of the ultimate objectives is to validate  $\kappa^{-1}$  scaling in the viscous-convective subrange.

## 4.2 Simulation procedure

Using the jet centerline (JC) forcing schemes introduced in Chapter 2 and Chapter 3, we can recreate the turbulent mixing environment of round jets for any scalars, including high Sc scalars. The simulation procedure is the same as shown in Sec. 3.3.1. The simulation parameters are shown in Table 4.1.

Table 4.1: Relevant parameters of the target experiments and the corresponding simulations

	Corresponding experiments					Simulation parameters			
	$U_c/x_o$	$C_c/x_o$	$\nu [\times 10^{-5}]$	Sc	$Re_D$	$L_x$	$\kappa_{max}\eta_B$	$N$	$Re_\lambda$
SCH1	0.0531	2.41	1.64	4	1500	0.649	2.0	256	51
SCH2	0.134	2.41	1.64	4	3900	0.649	2.0	512	81
SCH3	0.339	2.41	1.64	4	9800	0.649	2.0	1024	129
SCH4	0.0531	2.41	1.64	8	1500	0.649	2.0	384	51
SCH5	0.134	2.41	1.64	8	3900	0.649	2.0	768	81
SCH6	0.0531	2.41	1.64	16	1500	0.649	2.0	512	51
SCH7	0.134	2.41	1.64	16	3900	0.649	2.0	1024	81
SCH8	0.0531	2.41	1.64	32	1500	0.649	2.0	768	51
SCH9	0.0531	2.41	1.64	64	1500	0.649	2.0	1024	51

The computations are combinations of five different Schmidt numbers (Sc= 4, 8, 16, 32, 64) and three different Reynolds numbers ( $Re_\lambda = 51, 81, 129$ ). They are variations of simulations conducted in Chapter 3; the only differences are the higher Schmidt number and the larger number of grid points to satisfy  $\kappa_{max}\eta_B \geq 2.0$ . The number of grid points in each direction,  $N$ , can be determined by the following equation, which is adapted from Eq. (3.18):

$$N \geq \frac{2.0}{15^{\frac{1}{4}}\pi} \frac{L_x}{l} Re_\lambda^{\frac{3}{2}} Sc^{\frac{1}{2}}. \quad (4.4)$$

As seen in the relation, simulations with higher Schmidt numbers are computationally more expensive than unity Schmidt number simulations at the same Reynolds number.

## 4.3 Results

### 4.3.1 Instantaneous mixing structures

Scalar fields with two different Schmidt numbers are displayed in Fig. 4.2. The plots on the left have Sc = 1, and those on the right have Sc = 16. Both have the same

Reynolds numbers ( $Re_\lambda = 51$ ), grid resolutions ( $N = 512$ ), and numbers of contour levels (10). These two flows do not share the exactly same velocity field, but their velocity fields are under the same velocity forcing coefficients and viscosity.

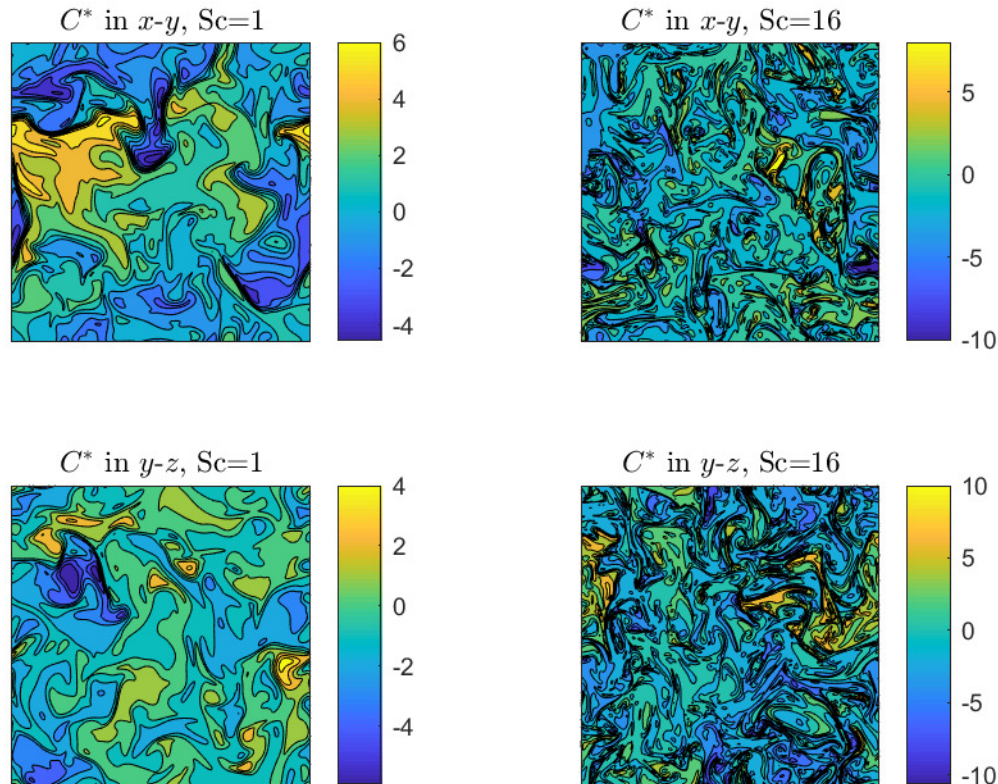


Figure 4.2: Contours of scalar fields in  $xy$  (top) and  $yz$  (bottom) planes with  $Sc = 1$  and  $Sc = 16$ .

As explained in Sec. 4.1, the Batchelor lengthscale becomes smaller as the Schmidt number increases. As a result, the mixing structures of  $Sc = 16$  are much finer than the those of  $Sc = 1$ , which is the difference between the two cases. As in the  $Sc = 1$  case, the mixing structures of  $Sc = 16$  appear homogeneous. For both Schmidt numbers, the structures seem isotropic in  $xy$  and  $yz$  planes. As mentioned previously in Sec. 3.3.3, the anisotropy created by the forcing method does not appear in the contour plots.

There is also a difference in the scalar gradients. A larger scalar gradient corresponds to many iso-contour lines being close to each other in a small region. In the  $Sc = 16$  plots, these sharp scalar gradients are observed throughout the cross-sections, but

in the  $Sc = 1$  plots, there are only a few number of regions with the contour lines crammed in a small region.

### 4.3.2 Scaling coefficient

Section 3.3.2 presents the scaling coefficients,  $\alpha_1$ ,  $\alpha_2$ , and  $\alpha_3$ , defined in Eq. (3.15-3.17). The same quantities have been computed from SCH1-8, and plotted in Fig. 4.3 as a function of the Reynolds number,  $Re_\lambda$ , (left) and as a function of the Schmidt number,  $Sc$ , (right).

For any data with  $Sc > 1$ , the variance coefficient,  $\alpha_1$ , increases with  $Re_\lambda$  for each Schmidt number, and increases with  $Sc$  for each Reynolds number. It seems that  $\alpha_1$  continues to increase with the Schmidt number, instead of reaching a constant high  $Sc$  limit. The scalar flux coefficient,  $\alpha_2$ , displays a similar trend, but the increase with  $Sc$  is very small at  $Re_\lambda = 51$ , as compared to  $\alpha_1$ . The relative values of the dissipation coefficient,  $\alpha_3$ , are almost the same as  $\alpha_1$ .

Dimotakis and Miller [105] also discusses the value of  $\overline{C'^2}/\overline{C}^2$ , which is proportional to  $\alpha_1$  (Eq. (3.15)). They show that in the limit of  $D \rightarrow 0$ , the probability density function (pdf) of the scalar should be

$$p(C) \rightarrow (1 - \overline{C})\delta(C) + \overline{C}\delta(1 - C), \quad (4.5)$$

and therefore,  $\overline{C'^2}/\overline{C}^2$  can be any value between zero and infinity as

$$\overline{C'^2}/\overline{C}^2 \rightarrow (1 - \overline{C})/\overline{C} \quad \text{as } Sc \rightarrow \infty. \quad (4.6)$$

This accords with our  $\alpha_1$  values, which increase with the Schmidt number for any Reynolds number.

### 4.3.3 Scalar flux

Normalized scalar flux quantities,  $\langle\langle u_x^* C^* \rangle\rangle / \sqrt{\langle\langle u_x^{*2} \rangle\rangle \langle\langle C^{*2} \rangle\rangle}$ , have been calculated from simulations in Table 4.1, and displayed in Fig. 4.4. The unity Schmidt number results from Table 3.2 with the same  $Re_\lambda$  are also displayed for comparison. The relation  $Re_\lambda = 1.3\sqrt{Re_D}$  has been applied to the experiments to convert  $Re_D$  to  $Re_\lambda$  [72].

At  $Re_\lambda = 51$ , the scalar flux value decreases as the Schmidt number increases, although the difference is very small for  $Sc \geq 16$ . A similar pattern is observed at  $Re_\lambda = 81$ , and there is little difference between  $Sc = 8$  and 16 values. At  $Re_\lambda = 129$ , however, the flux values are almost the same for  $Sc = 4$  and  $Sc = 1$ .

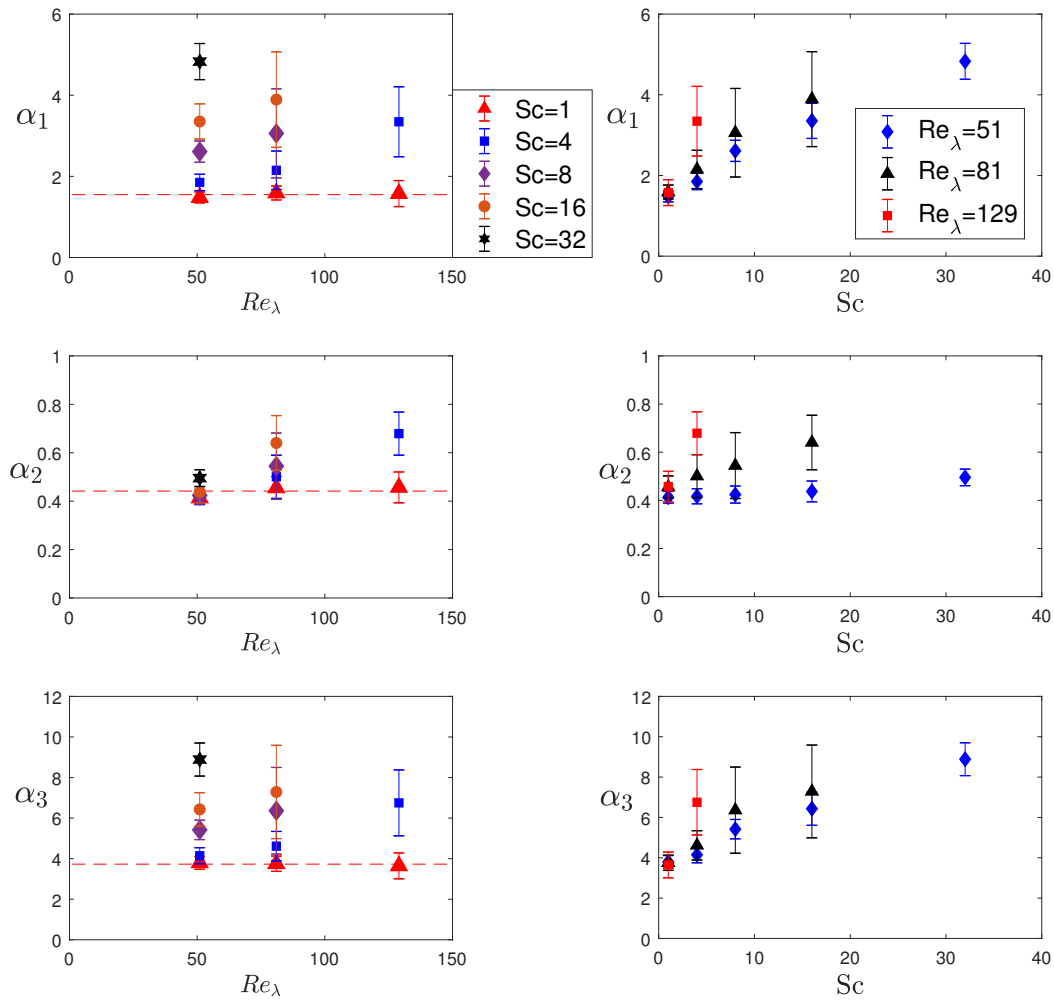


Figure 4.3: Scaling coefficients for the variance ( $\alpha_1$ , Eq. (3.15)), the scalar flux ( $\alpha_2$ , Eq. (3.16)), and the dissipation rate ( $\alpha_3$ , Eq. (3.17)) from SCH1-8, plotted as a function of  $Re_\lambda$  (left) and as a function of  $Sc$  (right). The dashed lines are the mean values for  $Sc = 1$ .

It seems that the effect of Schmidt number diminishes with increasing Reynolds number. Unfortunately, the number of high  $Sc$  experiments is too small to draw any conclusion.

At  $Sc = 4, 8,$  and  $16$ , the scalar flux increases with Reynolds number. This increase is in contrast with the unity Schmidt number values, whose increase with the Reynolds number is either small or unapparent. This difference is more evident in Fig. 4.5, which plots the scalar flux as a function of  $Sc$  for our simulation results.

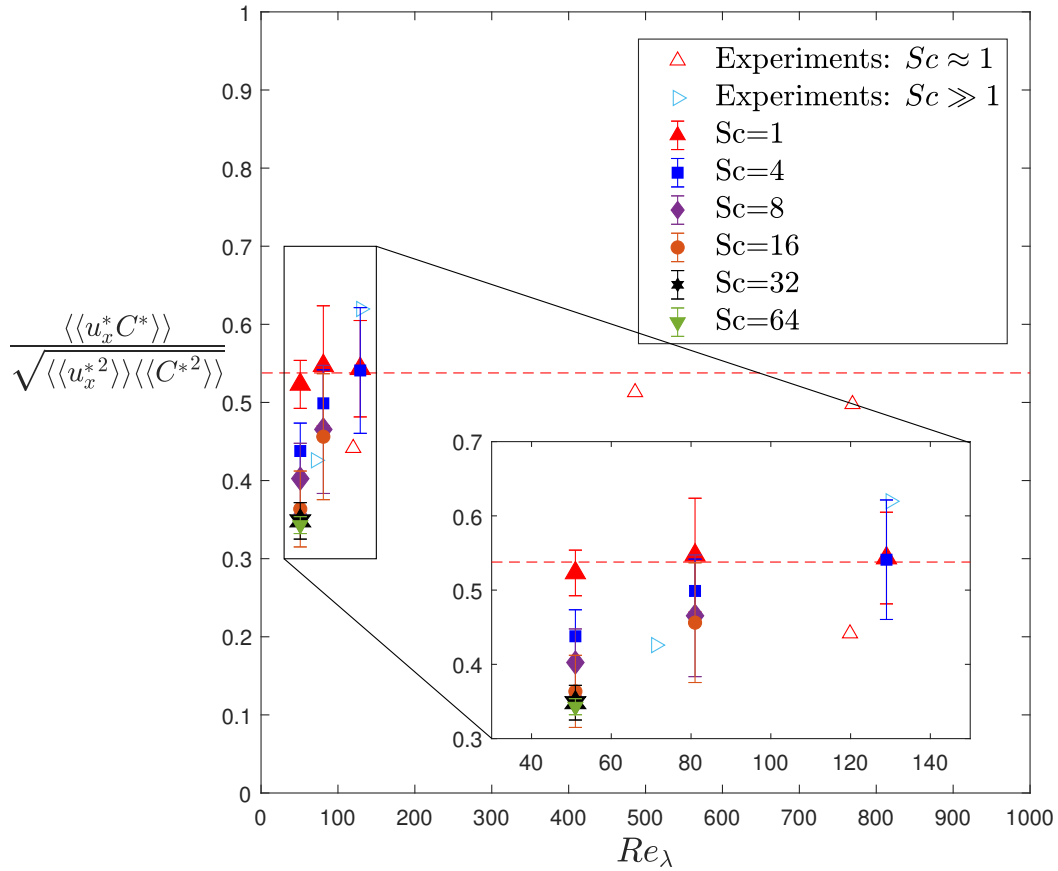


Figure 4.4: Comparison of numerical and experimental normalized scalar flux as a function of  $Re_\lambda$  for different Schmidt numbers. Round jet experiments with  $Sc \approx 1$  are Anderson & Bremhorst [71], Darisse *et al.* [31], and Chevray & Tutu [74], from low to high Reynolds numbers. Round jet experiments with  $Sc \gg 1$  are Webster *et al.* [59] and Antoine *et al.* [75], from low to high Reynolds numbers. A detailed summary is shown in Table 3.3. The figure displays SCL2,3,5 and SCH1-9 results. The mean of SCL2,3,5 values is shown as the red dashed line.

As previously mentioned, the flux values decrease with  $Sc$  for  $Re_\lambda = 51$  and  $81$ , and ultimately reach plateaus at  $Sc \geq 16$  and  $Sc \geq 8$ , respectively. Thus, an exponential fitting is provided to estimate the high Schmidt number limit for  $Re_\lambda = 51$  and  $81$ . The dashed lines for these two are weighted least-squares fits of a functional form  $q(Sc) = a_1 + a_2 \exp(-a_3 Sc)$ . The red dashed line is the mean of  $Re_\lambda = 129$  values.

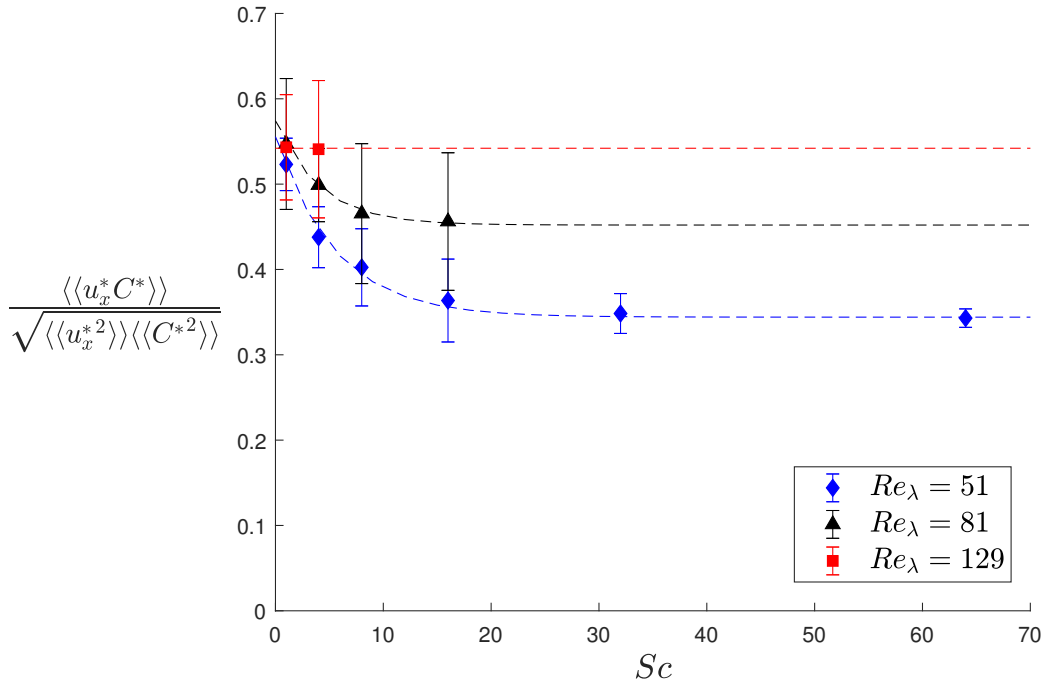


Figure 4.5: Normalized scalar flux as a function of  $Sc$ . The figure displays SCL2,3,5 and SCH1-9 results. The dashed lines for  $Re_\lambda = 51$  and  $81$  are weighted least-squares fits of a functional form  $q(Sc) = a_1 + a_2 \exp(-a_3 Sc)$ . The red dashed line is the mean of  $Re_\lambda = 129$  values.

Then, for  $Re_\lambda = 51$  and  $81$ , each scalar flux approaches

$$Re_\lambda = 51 : \frac{\langle\langle u_x^* C^* \rangle\rangle}{\sqrt{\langle\langle u_x^{*2} \rangle\rangle \langle\langle C^{*2} \rangle\rangle}} \rightarrow 0.344, \quad (4.7)$$

$$Re_\lambda = 81 : \frac{\langle\langle u_x^* C^* \rangle\rangle}{\sqrt{\langle\langle u_x^{*2} \rangle\rangle \langle\langle C^{*2} \rangle\rangle}} \rightarrow 0.452. \quad (4.8)$$

For  $Re_\lambda = 129$ , the mean of the two data is

$$Re_\lambda = 129 : \frac{\langle\langle u_x^* C^* \rangle\rangle}{\sqrt{\langle\langle u_x^{*2} \rangle\rangle \langle\langle C^{*2} \rangle\rangle}} = 0.542. \quad (4.9)$$

These three values from Eq. (4.7-4.9) are plotted in Fig. 4.7 as simulation data. There are also two high  $Sc$  experiments. Webster *et al.* [59] ( $Sc = 1000$ ,  $Re_\lambda = 71$ ) is between  $Re_\lambda = 51$  and  $Re_\lambda = 81$  lines, and Antoine *et al.* [75] ( $Sc = 2740$ ,  $Re_\lambda = 130$ ) is above  $Re_\lambda = 129$  line. The experiments show the same increasing trend with the Reynolds number.

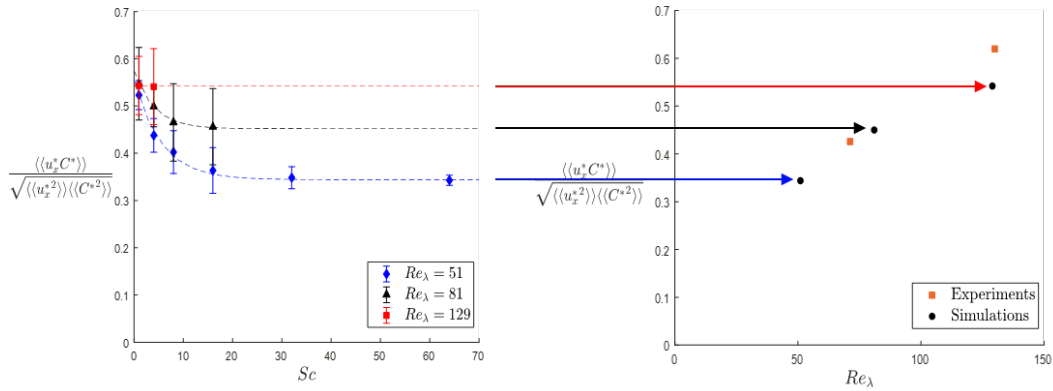


Figure 4.6: The mean of normalized scalar flux values for  $Re_\lambda = 129$ , and extrapolated high Schmidt number limits for  $Re_\lambda = 51$  and  $81$  from Fig. 4.5 are plotted in Fig. 4.7 as simulation data (black circles).

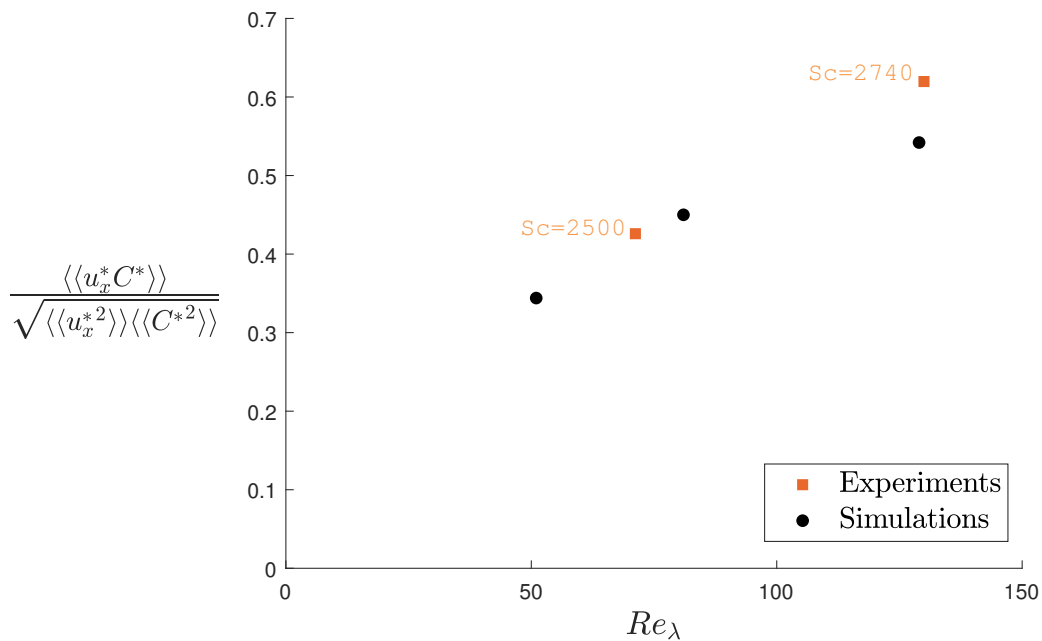


Figure 4.7: Comparison of extrapolated high Schmidt number limits of numerical normalized scalar flux for  $Re_\lambda = 51$  and  $81$ , the mean value for  $Re_\lambda = 129$ , and their corresponding experimental quantity as a function of  $Re_\lambda$ . Round jet experiments with  $Sc \gg 1$  are Webster *et al.* [59] ( $Re_\lambda = 71$ ) and Antoine *et al.* [75] ( $Re_\lambda = 130$ ), from low to high Reynolds numbers. A detailed summary of the experiments is shown in Table 3.3.

Energy spectra can be used to explain the observed behavior of the scalar flux values.

The normalized scalar flux can be expressed as integrals in spectral space:

$$\frac{\langle\langle u'_x C' \rangle\rangle}{\sqrt{\langle\langle u_x'^2 \rangle\rangle \langle\langle C'^2 \rangle\rangle}} = \frac{\int \widehat{u}_x(\boldsymbol{\kappa}) \widehat{C}^*(\boldsymbol{\kappa}) d\boldsymbol{\kappa}}{\sqrt{\int |\widehat{u}_x(\boldsymbol{\kappa})|^2 d\boldsymbol{\kappa} \int |\widehat{C}(\boldsymbol{\kappa})|^2 d\boldsymbol{\kappa}}}, \quad (4.10)$$

where  $\widehat{u}_x(\boldsymbol{\kappa})$  and  $\widehat{C}(\boldsymbol{\kappa})$  are the Fourier transforms of  $u'_x(\boldsymbol{x})$  and  $C'(\boldsymbol{x})$ . As explained in Sec. 4.1 with Fig. 4.1, the velocity and scalar spectra are both non-zero in the inertial-convective subrange, and the velocity spectrum decays rapidly to zero in the viscous-convective subrange. Thus, for low Reynolds number flows (small inertial-convective subrange), the normalized scalar flux value decreases with higher Schmidt number (larger viscous-convective subrange). However, as the Reynolds number increases (larger inertial-convective subrange), the effect of Schmidt number gets reduced; hence, the normalized scalar flux value for the same Re approaches a constant value independently of Sc. This explanation is consistent with most of the data presented in this section.

#### 4.3.4 Scaling exponent of energy spectra

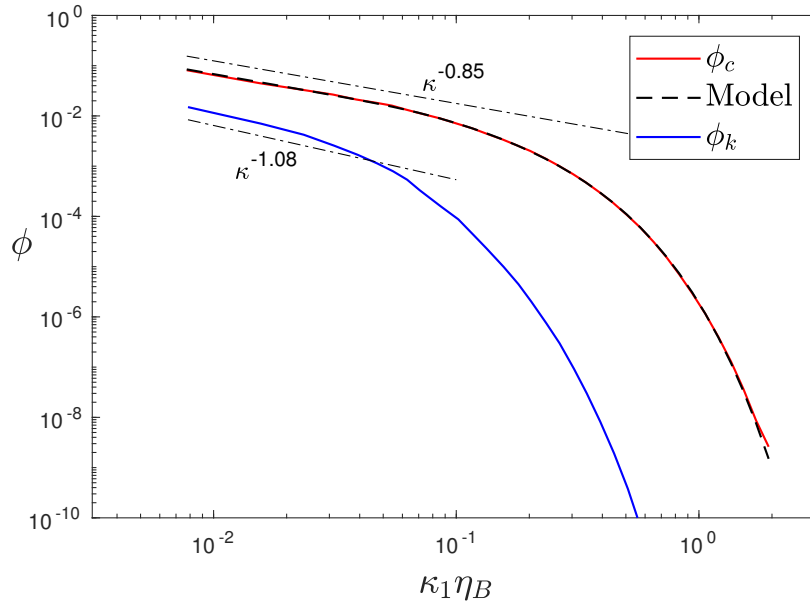


Figure 4.8: Scalar energy spectrum:  $\phi_c(\kappa_1)$  computed from SCH6 at  $Sc = 16$ ,  $Re_\lambda = 51$ , and its least-squares fit result with model spectrum, Eq. (4.11). The velocity spectrum  $\phi_k(\kappa_1)$  from SCH6 has been computed and divided by  $10^{3.5}$  to show the comparison.

One-dimensional energy spectra,  $\phi_c(\kappa_1)$ , have been computed from SCL2,3,5 and SCH1-5. In a similar fashion to Sec. 3.3.5, the scaling exponent  $n$  is estimated by using the following model:

$$\hat{\phi}_c(\kappa_1) = H_1 \kappa_1^{-n} \exp \left[ -H_2 \left( \left( (\eta_B \kappa_1)^4 + H_3^4 \right)^{\frac{1}{4}} - H_3 \right) \right], \quad (4.11)$$

where  $H_1$ ,  $H_2$ , and  $H_3$  are constants. This model is inspired by Eq. (3.25). An example of high Sc scalar spectra is shown in Fig. 4.8, computed from SCH4 at  $Re_\lambda = 51$  and  $Sc = 16$ . It shows a single slope,  $\phi_c \sim \kappa^{-0.85}$ .

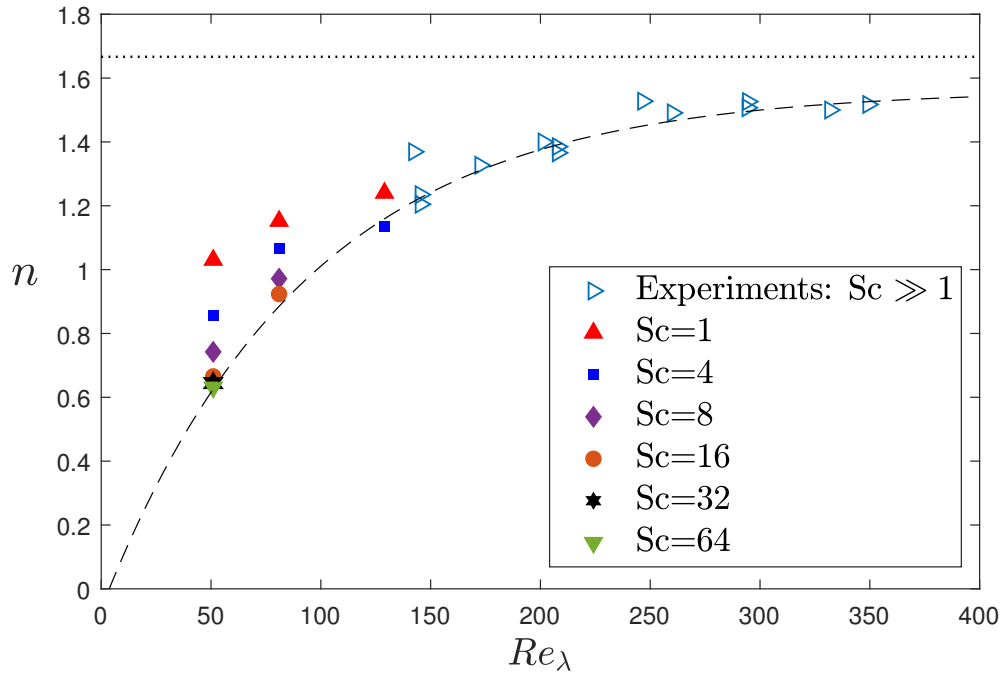


Figure 4.9: Scaling exponent  $n$  for the scalar energy spectra,  $\phi \sim \kappa^{-n}$ , calculated from SCL2,3,5 and SCH1-9. Experimental values are taken from round jets with  $Sc = 1900$  [92]. The dashed line is an exponential fitting using the three high Sc simulation data and all of the experimental values. The dash-dot line shows  $n = 5/3$ .

According to Batchelor's theory, at very high Reynolds and Schmidt numbers, the scalar energy spectrum is expected to display two different slopes (i.e.,  $-5/3$  and  $-1$ ) as shown in Fig. 4.1. However, because the simulations are performed at relatively low Reynolds and Schmidt numbers in this study, the spectra from our simulations show only a single slope. This slope is likely to be a mix of the two slopes from the inertial-convective and viscous-convective subranges. The scaling exponent  $n$  computed from SCH1-9 is shown in Fig. 4.9. The fitting results are

shown in Table 4.2. The scalar variance has been computed from  $\langle C^{*2} \rangle = \int 2\hat{\phi}_c d\kappa$ , as the spectrum is defined such that  $\int \phi_c(\kappa) d\kappa = \frac{1}{2}\langle C^{*2} \rangle$  in Eq. (3.25). The scalar dissipation rate has been computed from  $\chi = 2D|\nabla C'|^2 = 2D \int 2\kappa^2 \hat{\phi}_c d\kappa$ . These two parameters are compared against the actual values for the verification of fitting results.

Table 4.2: Least-squares fit results.

Name (Sc, Re $_\lambda$ )	$H_1$	$H_2$	$H_3$	$n$	$C_{\text{fit}}^2$	$C^2$	$\chi_{\text{fit}}$	$\chi$
SCH1 (4, 51)	0.167	6.16	$8.19 \cdot 10^{-2}$	0.855	2.46	2.46	0.382	0.376
SCH2 (4, 81)	0.876	6.29	$1.05 \cdot 10^{-1}$	1.07	12.1	12.1	5.02	5.08
SCH3 (4, 129)	1.20	6.27	$1.23 \cdot 10^{-1}$	1.14	11.54	12.23	10.84	10.49
SCH4 (8, 51)	0.147	4.95	$1.01 \cdot 10^{-4}$	0.742	3.64	3.68	0.457	0.450
SCH5 (8, 81)	0.633	7.87	$4.26 \cdot 10^{-4}$	0.972	4.63	4.56	1.37	1.41
SCH6 (16, 51)	0.150	7.55	$3.53 \cdot 10^{-2}$	0.665	4.29	4.31	0.519	0.504
SCH7 (16, 81)	0.749	5.67	$6.45 \cdot 10^{-2}$	0.923	16.4	15.8	5.31	5.51
SCH8 (32, 51)	0.557	7.22	$2.42 \cdot 10^{-4}$	0.645	12.1	12.3	1.28	1.18
SCH8 (64, 51)	0.158	6.31	$2.02 \cdot 10^{-2}$	0.631	7.63	7.65	0.739	0.784

At all simulated Reynolds numbers (Re $_\lambda$  = 51, 81, 129), the value of  $n$  decreases as the Schmidt number increases. This is consistent with an expected smaller value for the viscous-convective subrange (becoming more dominant for high Sc) than for the inertial subrange. For the results with Sc = 4, 8, and 16, respectively, the  $n$  value increases with the Reynolds number. Unlike the scalar flux in Sec. 4.3.3, however, the difference between the unity Schmidt number and higher Schmidt number values does not decrease with increasing Reynolds number.

Miller and Dimotakis [92] measured spectral slopes from round jets with Sc = 1900 at different Reynolds numbers. They estimated the  $n$  values by first plotting the derivatives  $d(\log(\phi_c))/d(\log(\kappa))$  as a function of  $\log(\kappa)$ . For each of these plots, there was a wavenumber range in which the derivatives seem to fluctuate around a constant value. Then, they used the mean of the derivatives over this range as

the  $n$  value. Note that they also found each scalar energy spectrum displayed a single region with a constant slope, even at this high Schmidt number. The  $n$  values measured from this constant-slope region show an increasing trend with  $Re_\lambda$ , which is also observed in our simulation results. However, it is surprising to find that the high  $Sc$  experimental values are larger than those from two jets with  $Sc \approx 1$  [77, 78] at similar  $Re_\lambda$ .

Figure 4.10 plots the  $n$  value as a function of  $Sc$  for our simulation results. As previously mentioned, the  $n$  values decrease for all Reynolds numbers. Since we have more than two points for  $Re_\lambda = 51$  and 81, an exponential fitting is provided to estimate the high Schmidt number limit. The dashed lines for these two are weighted least-squares fits of a functional form  $q(Sc) = a_1 + a_2 \exp(-a_3 Sc)$ .

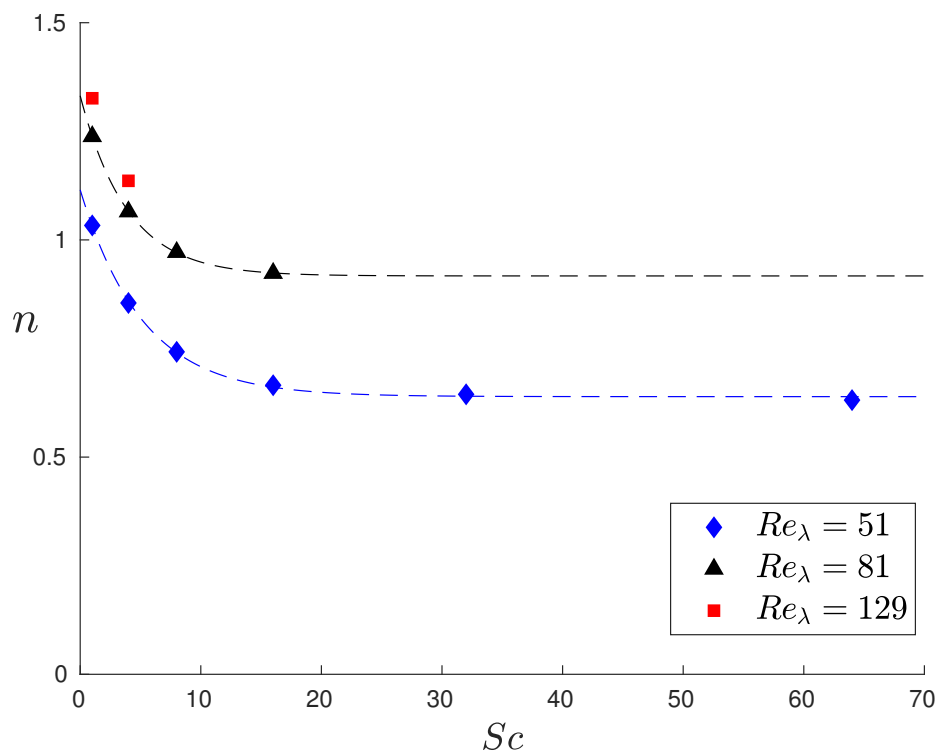


Figure 4.10: Scaling exponent  $n$  as a function of  $Sc$ . The figure displays SCL2,3,5 and SCH1-9 results. The dashed lines for  $Re_\lambda = 51$  and 81 are weighted least-squares fits of a functional form  $q(Sc) = a_1 + a_2 \exp(-a_3 Sc)$ .

As shown in Fig. 4.1, the scaling slope in the viscous-convective region is theoretically less than that in the inertial-convective region. The  $n$  values computed from high  $Sc$  simulations are presumed to be the mixture of the two slopes; therefore,

$1 < n < 5/3$ . Thus, it makes sense that the  $n$  values from  $Sc > 1$  are smaller than those from  $Sc = 1$  or from  $\phi_k(\kappa_1)$ , as seen in Fig. 4.9. The velocity spectrum  $\phi_k(\kappa_1)$  must have a larger  $n$  than  $\phi_c(\kappa_1)$  with  $Sc > 1$ , because  $\phi_k(\kappa_1)$  does not include the viscous-convective subrange. Our speculation that  $\phi_c(\kappa_1)$  with  $Sc > 1$  shows the mixture of the two regions may also explain the reason why the  $n$  values from  $Sc = 4$  are also larger than 1 at higher Reynolds numbers.

#### 4.3.5 Discussion on the scaling exponent

As previously mentioned in Sec. 4.3.2, Dimotakis and Miller [105] discuss the scalar mixing behavior in the limit of infinite Schmidt numbers. First, the scalar values are initially bounded as  $0 \leq C \leq 1$ . Then, the pdf of the scalar for  $D \rightarrow 0$ , shown in Eq. (4.5), leads to the following relation for the scalar variance at infinite  $Sc$ :

$$\overline{C'^2} \rightarrow \overline{C}(1 - \overline{C}) \quad \text{as } Sc \rightarrow \infty. \quad (4.12)$$

Therefore, the scalar variance should be finite at the limit of infinite Schmidt numbers.

This boundedness is, in fact, consistent with our finding that  $n < 1$  at the high  $Sc$  limit for some low  $Re_\lambda$  data. As a reminder, the spectrum is defined such that  $\int \phi_c(\kappa) d\kappa = \frac{1}{2} \langle C'^2 \rangle$  in Eq. (3.25). The model spectrum used in Eq. (4.11) can be simplified to

$$\hat{\phi}_c(\kappa) = J_1 \kappa^{-n} \exp[-J_2 \kappa \eta_B]. \quad (4.13)$$

We may find an expression for  $J_1$  from the following relation:

$$\chi = 2 \int_{2\pi/L}^{\infty} 2D\kappa^2 \hat{\phi}_c(\kappa) d\kappa \quad (4.14)$$

$$= 4DJ_1 \int_{2\pi/L}^{\infty} \kappa^{-n+2} \exp[-J_2 \kappa \eta_B] d\kappa, \quad (4.15)$$

where  $L$  is the geometrical dimension of the system, such as the domain length.

When  $w = J_2 \kappa \eta_B$  or  $\kappa = \frac{w}{J_2 \eta_B}$  is applied, the following relation can be obtained:

$$\chi = 4DJ_1 (J_2 \eta_B)^{n-3} \int_{2\pi J_2 \eta_B / L}^{\infty} w^{-n+2} \exp[-w] dw. \quad (4.16)$$

Then, we define  $p(J_2) = J_2^{n-3} \int_{2\pi J_2 \eta_B / L}^{\infty} w^{-n+2} \exp[-w] dw$  for simplicity, and solve for  $J_1$ :

$$J_1 = \frac{\chi}{4} \left( \frac{\nu}{\varepsilon} \right)^{1/2} \eta_B^{-n+1} \frac{1}{p}. \quad (4.17)$$

The value of  $p(J_2)$  is finite at  $Sc \rightarrow \infty$ , because

$$= \lim_{Sc \rightarrow \infty} J_2^{n-3} \int_{2\pi J_2 \eta_k / L \sqrt{Sc}}^{\infty} w^{-n+2} \exp[-w] dw \quad (4.18)$$

$$= J_2^{n-3} \int_0^{\infty} w^{-n+2} \exp[-w] dw \quad (4.19)$$

$$= J_2^{n-3} \Gamma[3-n] < \infty \quad \text{for } n < 3, \quad (4.20)$$

where  $\Gamma[z] = \int_0^{\infty} x^{z-1} e^{-x} dx$  is the Gamma function.

Thus, we now suggest the following form for the scalar energy spectrum:

$$\phi_c(\kappa) = G_1 \chi \left( \frac{\nu}{\varepsilon} \right)^{1/2} \eta_B^{-n+1} \kappa^{-n} \exp[-G_2 \kappa \eta_B]. \quad (4.21)$$

The expressions suggested by Batchelor, Eq. (4.2), and Kraichnan, Eq. (4.3), also include  $\chi(\nu/\varepsilon)^{1/2}$  as coefficients. The exponential part of Eq. (4.21) is essentially the same as that of the Kraichnan-form. A difference is that the scaling exponent of Eq. (4.21) is  $n$ , instead of 1.

Now, we may obtain the variance from Eq. (4.21):

$$\overline{C'^2} = \int_{2\pi/L}^{\infty} \phi_c(\kappa) d\kappa \quad (4.22)$$

$$= G_1 \chi \left( \frac{\nu}{\varepsilon} \right)^{1/2} \eta_B^{-n+1} \int_{2\pi/L}^{\infty} \kappa^{-n} \exp[-G_2 \kappa \eta_B] d\kappa \quad (4.23)$$

Apply  $z = G_2 \kappa \eta_B$  or  $\kappa = \frac{z}{G_2 \eta_B}$ :

$$\overline{C'^2} = G_1 G_2^{n-1} \chi \left( \frac{\nu}{\varepsilon} \right)^{1/2} \int_{2\pi G_2 \eta_B / L}^{\infty} w^{-n} \exp[-w] dw \quad (4.24)$$

Then, at the infinite  $Sc$  limit:

$$\lim_{Sc \rightarrow \infty} \overline{C'^2} = G_1 G_2^{n-1} \chi \left( \frac{\nu}{\varepsilon} \right)^{1/2} \int_0^{\infty} w^{-n} \exp[-w] dw \quad (4.25)$$

$$= G_1 G_2^{n-1} \chi \left( \frac{\nu}{\varepsilon} \right)^{1/2} \Gamma[1-n] < \infty. \quad (4.26)$$

Therefore, our simulation results that  $n$  is smaller than 1 at the high  $Sc$  limit are consistent with the boundedness of scalar variance at  $Sc \rightarrow \infty$ .

## Chapter 5

### CONCLUSION

A set of novel forcing schemes was derived and validated. The goal of the current study was to find forcing terms used for a triply periodic box that would produce turbulence of a practical flow. These new methods are distinct from the previous ones in that they generate turbulent flows of a round jet on the centerline.

#### 5.1 Jet centerline (JC) velocity forcing scheme

The derivation of velocity forcing terms began with examining the Navier-Stokes equation. There were three important steps. The first was to obtain the governing equations for fluctuating velocities from  $NS(\bar{\mathbf{u}} + \mathbf{u}') - \overline{NS(\bar{\mathbf{u}} + \mathbf{u}')}$ . The second was to apply the mean velocity information of a round jet (centerline region) to every term, and the third was to apply  $x/x_o$  normalization to make velocity fluctuations homogeneous. These treatments on velocity fields enabled the derivation of a unique forcing scheme.

These jet centerline (JC) forcing terms were used in a 3D cubic box, and turbulent characteristics computed from the simulation results were compared against round jet experiments. First, the statistical mean for each term in the energy budget equation was found to match that of experimental measurement. Second, the mean values for anisotropy, kinetic energy, and dissipation were found to be within the range of experiment values. A normalized kinetic energy spectrum in the longitudinal direction was computed from the highest  $Re_\lambda$  simulation we performed. Our simulation result was very close to the spectrum calculated from the experiment by Burattini *et al.* [30]. Thus, the JC scheme was proved to indeed generate turbulence of round jets on the centerline.

#### 5.2 JC scalar forcing scheme

A similar procedure was applied to the scalar transport equation, to derive JC scalar forcing terms. The mean scalar profile of a round jet on the centerline was used to evaluate  $\bar{C}$  terms in the advection-diffusion equation, and  $x/x_o$  normalization was also applied to the scalar fluctuations. Unity Schmidt number simulations were performed with these forcing terms. Scalar mixing properties, such as normalized scalar flux and scaling exponents of scalar energy spectra, were found to be

comparable to experiments.

In addition, a dimensional analysis was conducted to relate the inputs of the simulations, such as forcing coefficients, length of domain, and viscosity, to outputs, such as scalar variance, flux, and dissipation rate. When adequately non-dimensionalized, the outputs are only functions of the Reynolds number.

We also explored the effects of the velocity forcing terms on the scalar results. Coefficients of the velocity forcing terms were varied, while keeping the scalar forcing terms as the same. Some of the test simulations turned out to be unstable; the scalar variance increased exponentially over time, failing to converge to statistically steady states. The velocity fields, on the other hand, were stable for all the test simulations. Therefore, our results indicated that the relation between the velocity and scalar forcings must be considered, as opposed to the previous scalar forcing schemes that were derived independently of the velocity forcing schemes. In contrast, the proposed JC scalar forcing has an intrinsic connection to the JC velocity forcing; they were both derived to produce turbulence of round jets.

### 5.3 Effects of Schmidt number under JC forcing schemes

Additional computations with  $Sc > 1$  were performed for three Reynolds numbers,  $Re_\lambda = 51, 81,$  and  $129$ . Normalized scalar flux and scaling exponents of scalar energy spectra were computed, and compared with  $Sc = 1$  results. Our finding indicated that the scalar fluxes decrease with increasing  $Sc$  for  $Re_\lambda = 51$  and  $81$ , but stay the same for  $Re_\lambda = 129$ . Also, the terms reached high  $Sc$  limits at  $Sc \geq 16$  and  $Sc \geq 8$  for  $Re_\lambda = 51$  and  $81$ , respectively. These high  $Sc$  limits increase with increasing  $Re_\lambda$ .

Since we could not perform very high  $Sc$  simulations because of high computational costs, the scalar energy spectra computed from our simulations do not show clearly separated inertial-convective and viscous-convective subranges. Instead, each spectrum seems to display a single power-law region before the diffusive subrange. The scaling exponents  $n$  computed from these single slopes were compared with  $Sc = 1$  results. It was found that the  $n$  values decrease with increasing  $Sc$ . It was suspected that this seemingly single slope can be a mix of the two subranges. Therefore, the  $n$  values from  $Sc > 1$  data must be lower than  $Sc = 1$  ones, because the viscous-convective subrange should have a lower scaling exponent than inertial-convective subrange, according to Batchelor's theory [87].

#### 5.4 Significance and future work

The objective of the current research was achieved. We successfully developed a pair of novel velocity and scalar forcing schemes, which generate turbulent flow fields of round jets on the centerline.

There were additional significant discoveries as well. In Chapter 2, we derived unique algebraic expressions for the centerline kinetic energy and dissipation rate that involved only the anisotropy ratio, integral length-scale, mean centerline velocity, and longitudinal coordinate. These relations are not just applicable to our simulations, but should also hold true for any turbulent round jets, because our entire derivations are based on physical properties. The derivation of our forcing terms was essential to the discovery of these expressions.

In Chapter 3, we did not discover closed equations for scalar variance or dissipation rate, but we found scaling coefficients for the normalized scalar variance, flux, and dissipation rate, through dimensional analysis. The dimensional analysis was possible, only because we used the simulation property that the input parameters control the scalar statistics (outputs). Thus, our cubic box simulations led to the discovery of important relations pertinent to turbulent round jets.

We were also able to explore the effect of Reynolds and Schmidt numbers carefully in Ch. 4, because they are easy to control in these 3D box computations. For both normalized scalar flux values and scaling exponents, we traced how they changed with  $Sc$  respectively, and determined their high  $Sc$  limits. This type of parametric study is difficult with experiments.

More importantly, We discovered a new way of deriving forcing terms. The information about velocity and scalar fields of a specific practical flow was used to derive forcing terms that would create the same turbulence in a simple geometry. This has potential to be applied to various flows. In fact, Dhandapani *et al.* [106] has already expanded it to turbulent mixing layers and other parts of planar and round jets (not centerline region).

Although the current study focused on the local region of one type of flow, it has opened a new category of forcing schemes, which is more realistic than the previous ones. By using the methodology introduced here, other realistic forcing terms can be derived for different purposes.

## Appendix A

### UNCERTAINTY QUANTIFICATION

#### A.1 Definitions

Suppose there are  $N$  time-sequential samples available, modeled as a stationary ergodic random process  $x_i$  sampled at every  $\Delta t$ . The autocorrelation function for this random process is defined as

$$\rho(k) \equiv \frac{E[(x_i - \mu)(x_{i+k} - \mu)]}{\sigma^2}, \quad (\text{A.1})$$

where  $k$  is the lag,  $\mu$  is the expected mean of  $x_i$ , and  $\sigma^2$  is the variance,  $E[(x_i - \mu)^2]$ .

These samples are then divided into  $p$  number of non-overlapping segments with length  $n = N/p$ . A mean value,  $\hat{s}_j$ , is calculated for each  $j$ th segment:

$$\hat{s}_j = \frac{1}{n} \sum_{i=1+n(j-1)}^{nj} x_i. \quad (\text{A.2})$$

The set of mean values from the segments,  $\{\hat{s}_j\}$ , can also be considered as the elements of a random process. The expected mean of  $\hat{s}_j$  is  $\mu$ . Let us define the expected averaging error as

$$\delta_n^2 \equiv E[(\hat{s}_j - \mu)^2]. \quad (\text{A.3})$$

The goal of this uncertainty quantification is to estimate  $\delta_n^2$  when  $n \rightarrow N$ .

#### A.2 Modeling

According to [107],

$$\delta_n^2 = \frac{\sigma^2}{n} \left[ 1 + 2 \sum_{k=1}^{n-1} \left(1 - \frac{k}{n}\right) \rho(k) \right]. \quad (\text{A.4})$$

Rearranging the terms, we obtain

$$\delta_n^2 = \frac{1}{n} \left( \sigma^2 + 2\sigma^2 \sum_{k=1}^{n-1} \rho(k) \right) - \frac{1}{n^2} \left( 2\sigma^2 \sum_{k=1}^{n-1} k \rho(k) \right). \quad (\text{A.5})$$

Inspired by the form of Eq. (A.5), we suggest modeling the averaging error as

$$\delta_n^2 \approx f(n; \mathbf{B}) = \frac{B_1}{n} + \frac{B_2}{n^2}, \quad (\text{A.6})$$

where  $\mathbf{B} = [B_1, B_2]$  is a vector of parameters. This expression is exact in the limit of  $n\Delta t$  sufficiently larger than the integral time scale.

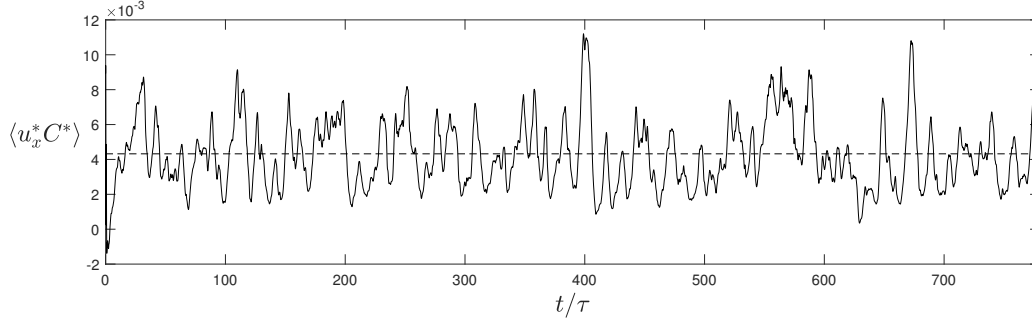


Figure A.1: Volume-averaged scalar flux,  $\langle u_x^* C^* \rangle$ , from SCL2 plotted as a function of the time normalized by the eddy time scale,  $\tau_o$ . The horizontal dashed line indicates its time-averaged value.

### A.3 Calculation

In practice, we compute the averaging error for segments of length  $n$  as

$$\hat{\delta}^2(n) = \frac{1}{p} \sum_{j=1}^p (\hat{s}_j(n) - \hat{\mu})^2, \quad (\text{A.7})$$

where

$$\hat{\mu} = \frac{1}{N} \sum_{i=1}^N x_i. \quad (\text{A.8})$$

Then, a least-squares fit is used over  $\hat{\delta}^2(n)$  with Eq. (A.6) to determine  $\mathbf{B}$  by solving:

$$\mathbf{B} = \arg \min_{\mathbf{B}} \sum_{n=n_k}^{N/2} \left( \hat{\delta}^2(n) - f(n; \mathbf{B}) \right)^2. \quad (\text{A.9})$$

Theoretically, the minimum number of segments is  $p = 2$ ; thus, the maximum segment length is  $N/2$ . As mentioned previously, the minimum segment length must be sufficiently large for Eq. (A.6) to be valid. We suggest varying  $n_k$ , determining  $\mathbf{B}$  for each  $n_k$  value, and finally finding the maximum  $f(N)$ :

$$\hat{\delta}_N^2 = \max_{n_k} f(N; \mathbf{B}|_{n_k}). \quad (\text{A.10})$$

Because it is the most conservative choice, we will use this maximum  $f(N; \mathbf{B})$  as the final estimation for  $\delta_n^2$  as  $n \rightarrow N$ .

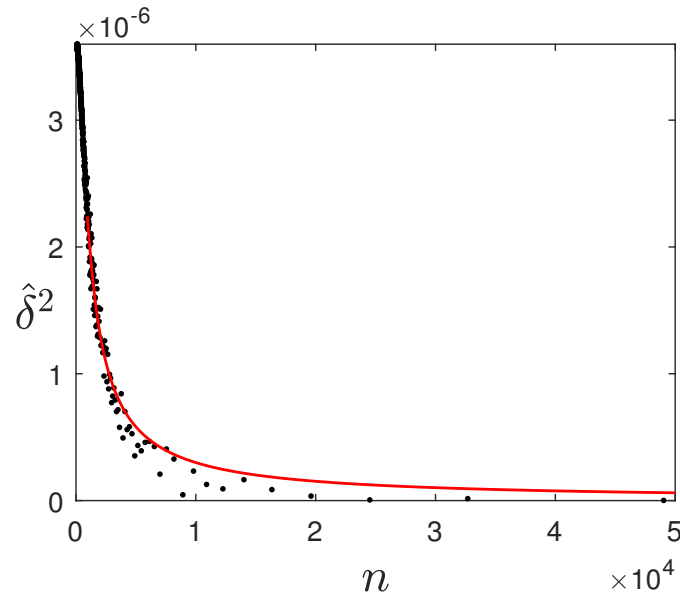


Figure A.2: Averaging error  $\hat{\delta}^2$  as a function of  $n$ , for  $\langle u_x^* C^* \rangle$  data presented in Fig. A.1. The solid line represents the least-squares fit result with  $\hat{\delta}^2$  for  $n \geq 920$ :  $\hat{\delta}^2 = 0.00309/n - 0.911/n^2$ .

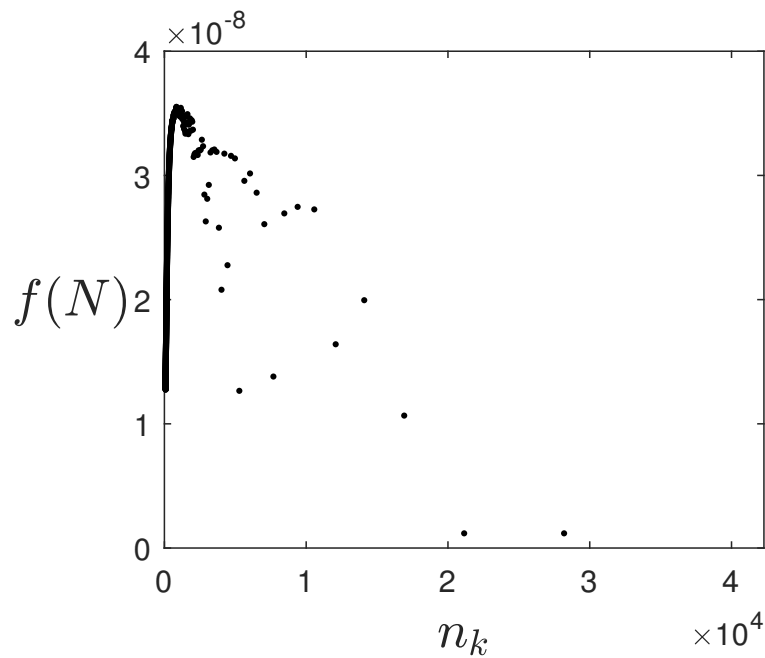


Figure A.3:  $f(N; \mathbf{B}|_{n_k})$  from Eq. (A.10) is computed as a function of  $n_k$ .

#### A.4 Example

The volume-averaged scalar flux,  $\langle u_x^* C^* \rangle$ , has been computed from SCL2 in Chapter 3, and is shown in Fig. A.1, as a function of normalized time. In this example, the transient period is about  $15\tau_o$ . The dashed line indicates the time-averaged value of the entire data. The algorithm introduced in Sec. A.3 is applied to this data.

$\hat{\delta}^2(n)$  from Eq. (A.7) is shown in Fig. A.2. Then,  $f(N; \mathbf{B}|_{n_k})$  from Eq. (A.10) is computed as a function of  $n_k$ , and displayed in Fig. A.3. In this example,

$$\arg \max_{n_k} f(N; \mathbf{B}|_{n_k}) = 920. \quad (\text{A.11})$$

The corresponding fit result,  $f(n; \mathbf{B}|_{n_k=920})$  for  $n \geq 920$ , is shown in Fig. A.2. Finally, the estimated averaging error is

$$\hat{\delta}_N^2 = 3.56 \times 10^{-8}, \quad (\text{A.12})$$

$$\sqrt{\hat{\delta}_N^2} = 1.87 \times 10^{-4}. \quad (\text{A.13})$$

$\sqrt{\hat{\delta}_N^2}$  is about 4.32% of the mean value  $\mu = 0.00437$ .

The same procedure has been repeated for each data point presented throughout the paper. The error bar indicates  $\pm \sqrt{\hat{\delta}_N^2}$ .

*Appendix B*

## RESOLUTION TEST

All the simulations presented in this work have been performed in a triply periodic box with uniform grids. The resolution of those computations can be determined by using a maximum wavenumber  $\kappa_{max}$  and the smallest length-scales, such as the Kolmogorov length-scale  $\eta_k$  for velocity fields or the Batchelor length-scale  $\eta_B$  for scalar. These quantities are defined as

$$\kappa_{max} = \pi/\Delta x = \pi N/L_x, \quad (\text{B.1})$$

$$\eta_k = \left( \nu^3/\varepsilon \right)^{1/4}, \quad (\text{B.2})$$

$$\eta_B = \eta_k/\text{Sc}^{1/2}. \quad (\text{B.3})$$

Conventionally, the resolution of  $\kappa_{max}\eta_k > 1.5$  for velocity fields [19, 56, 108, 109] and  $\kappa_{max}\eta_B > 1.5$  for scalar fields [9, 110, 111] are considered to be adequate for up to second-order statistics. In this chapter, different resolutions will be tested by repeating some of the simulation results presented in Chapter 2 and 3.

Table B.1: Relevant parameters of simulations for resolution test

	$U_c/x_o$	$C_c/x_o$	$\nu = D$	$L_x$	$\kappa_{max}\eta_k$	$N$	$\text{Re}_\lambda$
SCL2	0.0531	2.41	$1.64 \times 10^{-5}$	0.649	2.0	128	51
RES1	0.0531	2.41	$1.64 \times 10^{-5}$	0.649	1.5	96	51
RES2	0.0531	2.41	$1.64 \times 10^{-5}$	0.649	3.0	192	51

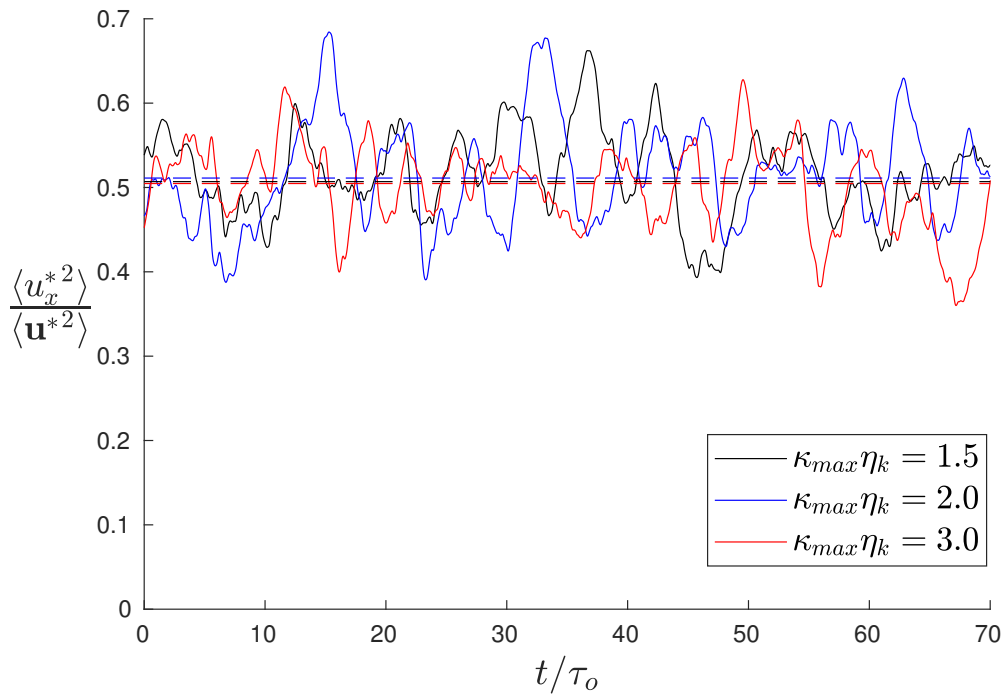


Figure B.1: Temporal fluctuations of anisotropy  $\langle u_x^{*2} \rangle / \langle \mathbf{u}^{*2} \rangle$  as a function of the time normalized by the eddy time scale,  $\tau_o$ . The time-averaged value for each curve is indicated as a dashed-line.

One of the important quantities discussed in Chapter 2 is the anisotropy ratio,  $\langle \langle u_x^{*2} \rangle \rangle / \langle \langle \mathbf{u}^{*2} \rangle \rangle$ . The temporal fluctuations of this quantity for the three simulations listed in Table B.1 are shown in Fig. B.1. Time-averaged values of  $\langle u_x^{*2} \rangle / \langle \mathbf{u}^{*2} \rangle$  for the three resolutions are virtually the same:  $0.507 \pm 0.00984$  for  $\kappa_{max}\eta_k = 1.5$ ;  $0.511 \pm 0.0117$  for  $\kappa_{max}\eta_k = 2.0$ ; and  $0.505 \pm 0.0137$  for  $\kappa_{max}\eta_k = 3.0$ . The uncertainties are obtained by using the algorithm explained in Appendix A.

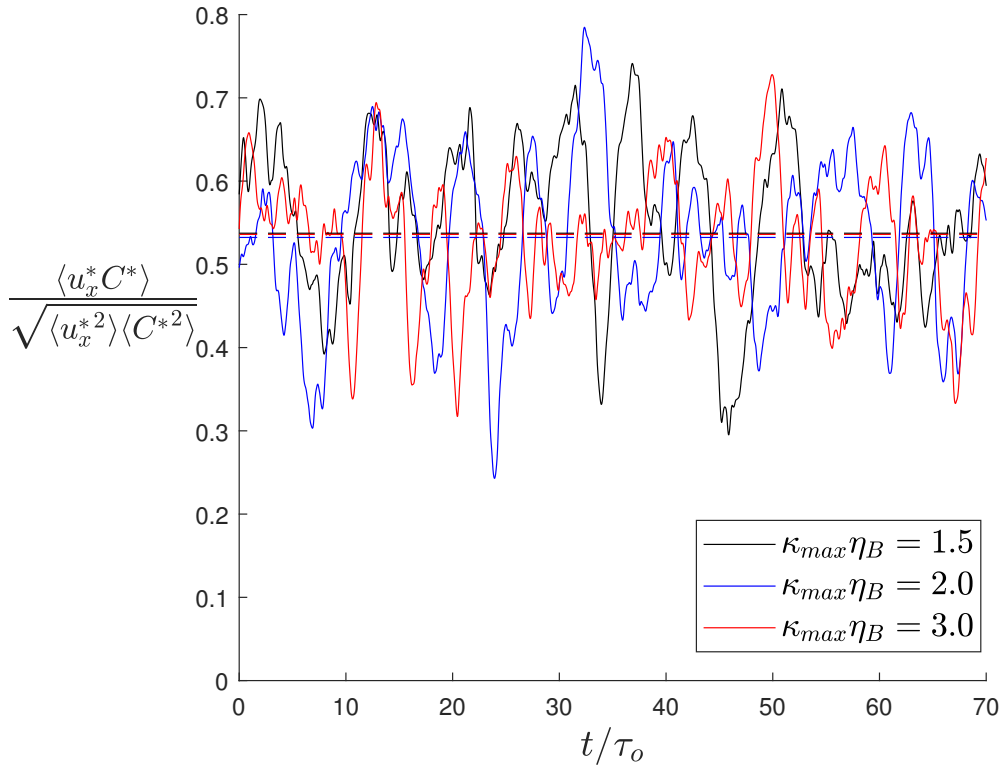


Figure B.2: Temporal fluctuations of normalized scalar flux  $\langle u_x^* C^* \rangle / \sqrt{\langle u_x^{*2} \rangle \langle C^{*2} \rangle}$  as a function of time normalized by the eddy time scale,  $\tau_o$ . The time-averaged value for each curve is indicated as a dashed-line.

SCL2 is the baseline simulation from Chapter 3. RES1 and RES2 are the additional computations conducted for different resolutions. Note that all three simulations have unity Schmidt numbers; thus,  $\eta_k$  is equal to  $\eta_B$ .

The next parameter for this resolution test is the normalized scalar flux value discussed in Chapter 3. Figure B.2 displays the test result. As in the anisotropy ratio test, the time-averaged values of  $\langle u_x^* C^* \rangle / \sqrt{\langle u_x^{*2} \rangle \langle C^{*2} \rangle}$  for the three resolutions are also very close to one another:  $0.537 \pm 0.0182$  for  $\kappa_{max}\eta_B = 1.5$ ;  $0.532 \pm 0.0173$  for  $\kappa_{max}\eta_B = 2.0$ ; and  $0.536 \pm 0.0119$  for  $\kappa_{max}\eta_B = 3.0$ .

This resolution test confirms that the minimum requirement is  $\kappa_{max}\eta_k > 1.5$  for velocity fields and  $\kappa_{max}\eta_B > 1.5$  for scalar fields, at least for second-order statistics. Since the current study does not deal with statistics higher than second-order ones, all the computations presented in this work satisfy the resolution requirement.

## Appendix C

### SIMULATION CODE (NGA)

The computational results presented in this thesis were performed with the NGA code. This simulation code is capable of computing variable density flows in complex geometries with various boundary conditions. The order of accuracy can be determined by the user. NGA uses an iterative semi-implicit scheme with staggering in space and time between a velocity field and scalar/density/pressure fields. In this section, we will give a brief description of how NGA calculates velocity and scalar fields for constant density flows with a uniform mesh and second-order accuracy, which are all the simulations presented in the current study. More details can be found in Desjardins *et al.* [61].

#### C.1 Discretization

The governing equations are

- Continuity

$$\frac{\partial u_j}{\partial x_j} = 0, \quad (\text{C.1})$$

- Momentum

$$\frac{\partial u_i}{\partial t} = -\frac{\partial}{\partial x_j}(u_i u_j) - \frac{1}{\rho} \frac{\partial p}{\partial x_i} + \frac{\partial \sigma_{ij}}{\partial x_j}, \quad (\text{C.2})$$

$$\text{where } \sigma_{ij} = \nu \left( \frac{\partial u_i}{\partial x_j} + \frac{\partial u_j}{\partial x_i} \right) - \frac{2}{3} \nu \frac{\partial u_k}{\partial x_k} \delta_{ij}, \quad (\text{C.3})$$

- Scalar

$$\frac{\partial C}{\partial t} = -\frac{\partial}{\partial x_j}(u_j C) + \frac{\partial}{\partial x_j} \left( D \frac{\partial C}{\partial x_j} \right). \quad (\text{C.4})$$

Here,  $u_i$  is one of the three-components of the velocity field,  $\rho$  is the density,  $p$  is the pressure,  $\sigma_{ij}$  is the deviatoric stress tensor,  $\nu$  is the kinematic viscosity,  $\delta_{ij}$  is the Kronecker delta function,  $C$  is the scalar, and  $D$  is the diffusivity. The summation convention over repeated indices is adopted.

The physical space, represented as  $\boldsymbol{x} = x_1 \hat{\mathbf{i}} + x_2 \hat{\mathbf{j}} + x_3 \hat{\mathbf{k}}$ , is mapped to a uniform computational grid of unity spacing. The grid spacing is written as  $\boldsymbol{\xi} = \xi_1 \hat{\mathbf{i}} + \xi_2 \hat{\mathbf{j}} + \xi_3 \hat{\mathbf{k}}$ ,

where  $\xi_1$  is the spacing increment in the x-direction,  $\xi_2$  is the spacing increment in the y-direction, and  $\xi_3$  is the spacing increment in the z-direction. For our geometry of a uniform mesh, the scaling factor associated with this transformation from a physical space representation to a computational space representation is  $h = dx_1/d\xi_1 = dx_2/d\xi_2 = dx_3/d\xi_3$ .

Velocity components are stored at cell faces, and all scalar quantities are stored at cell centers. Variables are staggered in time also, as shown in Fig. C.1.

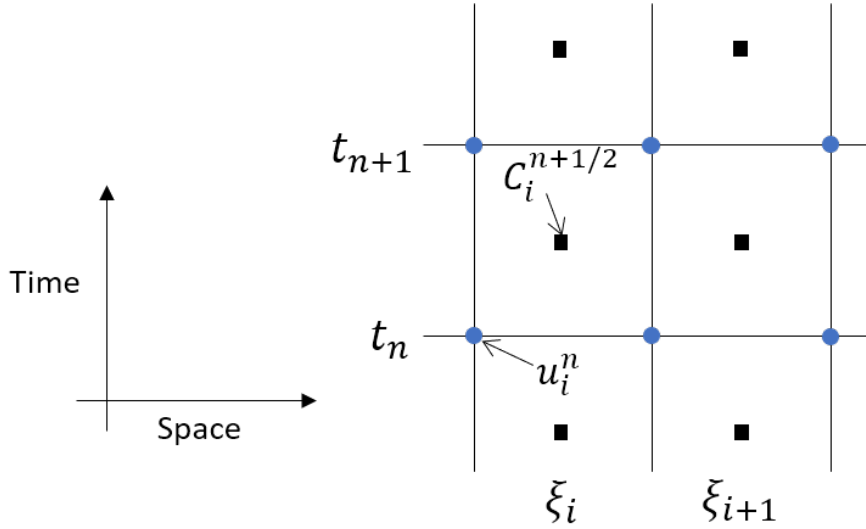


Figure C.1: Staggering in space and time. Velocity components are stored at cell faces, and all scalar quantities are stored at cell centers.

A second-order interpolation operator in the  $\xi_1$  direction acting on variable  $Z(\xi)$  is defined as  $\bar{Z}^{\xi_1}(\xi)$ :

$$\bar{Z}^{\xi_1}(\xi) = \frac{Z(\xi_1 + 1/2, \xi_2, \xi_3) + Z(\xi_1 - 1/2, \xi_2, \xi_3)}{2}. \quad (\text{C.5})$$

A second-order differentiation operator in the  $\xi_1$  direction acting on variable  $Z(\xi)$  is defined as  $\frac{\delta Z}{\delta \xi_1}(\xi)$ :

$$\frac{\delta Z}{\delta \xi_1}(\xi) = Z(\xi_1 + 1/2, \xi_2, \xi_3) - Z(\xi_1 - 1/2, \xi_2, \xi_3). \quad (\text{C.6})$$

## C.2 Temporal integration

Each time step involves  $Q$  number of sub-iterations. For the variables in this section, the superscript denotes the time, and the subscript denotes the sub-iteration level,  $k \in [1, Q]$ : e.g.  $Z_k^n$ .

• **Step 1**

Choose initial values:

$$\mathbf{u}_0^{n+1} = \mathbf{u}_0^n, \quad p_0^{n+3/2} = p_0^{n+1/2}, \quad C_0^{n+3/2} = C_0^{n+1/2}. \quad (\text{C.7})$$

• **Step 2**

The scalar field is advanced using a semi-implicit method:

$$C_k^{n+3/2} = C_k^{n+1/2} + \Delta t \cdot \left( \frac{M_k^{n+1/2} + M_{k-1}^{n+3/2}}{2} \right) + \frac{\Delta t}{2} \left( \frac{\partial M}{\partial C} \right)_k^{n+1} (C_k^{n+3/2} - C_{k-1}^{n+3/2}) \quad (\text{C.8})$$

where  $M$  represents the right-hand-side (RHS) of the scalar transport equation, Eq. (C.4), for compactness. Different scalar schemes exist to find a solution for Eq. (C.8), but the current study used the Bounded Cubic Hermite polynomial (BCH) transport scheme [73].

• **Step 3**

The momentum equation is solved using a semi-implicit method:

$$u_k^\dagger = u_k^n + \Delta t \cdot \left( \frac{N_k^n + N_{k-1}^{n+1}}{2} + \nabla p_{k-1}^{n+3/2} \right) + \frac{\Delta t}{2} \cdot \left( \frac{\partial N}{\partial u} \right)_k^{n+1/2} \cdot (u_k^\dagger - u_{k-1}^{n+1}), \quad (\text{C.9})$$

where  $u_k^\dagger$  is an intermediate velocity. For compactness,  $N$  represents the RHS of the momentum equation, Eq. (C.2). Here,  $u$  is the velocity component in  $x_1$  direction. The same procedure is applied to the velocity components in  $x_2$  and  $x_3$  directions.

• **Step 4**

We adjust the pressure field to make sure that the continuity is satisfied, by considering corrections to velocity,  $\delta u$ , and to pressure,  $\delta p$ , such that

$$\nabla^2 (\delta p_k^{n+3/2}) = \frac{\rho}{\Delta t} (\nabla \cdot \mathbf{u}_k^\dagger). \quad (\text{C.10})$$

This Poisson equation is solved via preconditioned Bi-CGStab method [112], which is a linear systems solver.

The velocity field is updated:

$$\mathbf{u}_k^{n+1} = \mathbf{u}_k^\dagger - \frac{\Delta t}{\rho} \cdot \nabla (\delta p_k^{n+3/2}). \quad (\text{C.11})$$

Then, the divergence of  $\mathbf{u}_k^{n+1}$  is zero, as a direct result of Eq. (C.10).

• **Step 5**

The pressure is updated:

$$p_k^{n+3/2} = p_{k-1}^{n+3/2} + \delta p_k^{n+3/2}. \quad (\text{C.12})$$

This completes a full cycle of the  $k$ th iteration, which is repeated  $Q$  times. Once the sub-iterations are converged, variables for the next time step are updated with the final results:

$$C^{n+3/2} = C_Q^{n+3/2}, \quad \mathbf{u}^{n+3/2} = \mathbf{u}_Q^{n+3/2}, \quad p^{n+3/2} = p_Q^{n+3/2}. \quad (\text{C.13})$$

## BIBLIOGRAPHY

- [1] Bruno Savard, Brock Bobbitt, and Guillaume Blanquart. Structure of a high Karlovitz n-C7H16 premixed turbulent flame. *Proceedings of the Combustion Institute*, 35(2):1377–1384, 2015.
- [2] Alexei Y Poludnenko and Elaine S Oran. The interaction of high-speed turbulence with flames: Global properties and internal flame structure. *Combustion and Flame*, 157(5):995–1011, 2010.
- [3] Peter E Hamlington, Alexei Y Poludnenko, and Elaine S Oran. Intermittency in premixed turbulent reacting flows. *Physics of Fluids*, 24(7):075111, 2012.
- [4] Daniele Carati, Sandip Ghosal, and Parviz Moin. On the representation of backscatter in dynamic localization models. *Physics of Fluids*, 7(3):606–616, 1995.
- [5] Jeffrey R Chasnov. Simulation of the Kolmogorov inertial subrange using an improved subgrid model. *Physics of Fluids A: Fluid Dynamics*, 3(1): 188–200, 1991.
- [6] Sandip Ghosal, Thomas S Lund, Parviz Moin, and Knut Akselvoll. A dynamic localization model for large-eddy simulation of turbulent flows. *Journal of Fluid Mechanics*, 286:229–255, 1995.
- [7] Christelle Seror, Pierre Sagaut, Christophe Bailly, and Daniel Juvé. On the radiated noise computed by large-eddy simulation. *Physics of Fluids*, 13(2): 476–487, 2001.
- [8] PK Yeung, Shuyi Xu, and KR Sreenivasan. Schmidt number effects on turbulent transport with uniform mean scalar gradient. *Physics of Fluids*, 14 (12):4178–4191, 2002.
- [9] PK Yeung, S Xu, DA Donzis, and KR Sreenivasan. Simulations of three-dimensional turbulent mixing for schmidt numbers of the order 1000. *Flow, turbulence and combustion*, 72(2-4):333–347, 2004.
- [10] PA O’GORMAN and DI Pullin. Effect of schmidt number on the velocity–scalar cospectrum in isotropic turbulence with a mean scalar gradient. *Journal of Fluid Mechanics*, 532:111–140, 2005.
- [11] PK Yeung and KR Sreenivasan. Direct numerical simulation of turbulent mixing at very low schmidt number with a uniform mean gradient. *Physics of Fluids*, 26(1):015107, 2014.

- [12] Toshiyuki Gotoh and Takeshi Watanabe. Scalar flux in a uniform mean scalar gradient in homogeneous isotropic steady turbulence. *Physica D: Nonlinear Phenomena*, 241(3):141–148, 2012.
- [13] DA Donzis, KR Sreenivasan, and PKc Yeung. Scalar dissipation rate and dissipative anomaly in isotropic turbulence. *Journal of Fluid Mechanics*, 532:199–216, 2005.
- [14] DA Donzis, PK Yeung, and KR Sreenivasan. Dissipation and enstrophy in isotropic turbulence: resolution effects and scaling in direct numerical simulations. *Physics of Fluids*, 20(4):045108, 2008.
- [15] Diego A Donzis, KR Sreenivasan, and PK Yeung. The batchelor spectrum for mixing of passive scalars in isotropic turbulence. *Flow, turbulence and combustion*, 85(3-4):549–566, 2010.
- [16] Takeshi Watanabe and Toshiyuki Gotoh. Statistics of a passive scalar in homogeneous turbulence. *New Journal of Physics*, 6(1):40, 2004.
- [17] KP Iyer and PK Yeung. Structure functions and applicability of yaglom’s relation in passive-scalar turbulent mixing at low schmidt numbers with uniform mean gradient. *Physics of Fluids*, 26(8):085107, 2014.
- [18] Neal P Sullivan, Shankar Mahalingam, and Robert M Kerr. Deterministic forcing of homogeneous, isotropic turbulence. *Physics of Fluids*, 6(4):1612–1614, 1994.
- [19] Vinayak Eswaran and Stephen B Pope. An examination of forcing in direct numerical simulations of turbulence. *Computers & Fluids*, 16(3):257–278, 1988.
- [20] Krister Alvelius. Random forcing of three-dimensional homogeneous turbulence. *Physics of Fluids*, 11(7):1880–1889, 1999.
- [21] Thomas S Lundgren. Linearly forced isotropic turbulence. In *Annual Research Briefs*, pages 461–473, Center for Turbulence Research, Stanford, 2003.
- [22] Phares L Carroll and Guillaume Blanquart. A proposed modification to Lundgren’s physical space velocity forcing method for isotropic turbulence. *Physics of Fluids*, 25(10):105114, 2013.
- [23] Don Daniel, Daniel Livescu, and Jaiyoung Ryu. Reaction analogy based forcing for incompressible scalar turbulence. *Physical Review Fluids*, 3(9):094602, 2018.
- [24] Panos N Papanicolaou and E John List. Investigations of round vertical turbulent buoyant jets. *Journal of Fluid Mechanics*, 195:341–391, 1988.

- [25] Nagangudy R Panchapakesan and John L Lumley. Turbulence measurements in axisymmetric jets of air and helium. Part 1. Air jet. *Journal of Fluid Mechanics*, 246:197–223, 1993.
- [26] Robert A Antonia and Q Zhao. Effect of initial conditions on a circular jet. *Experiments in Fluids*, 31(3):319–323, 2001.
- [27] Giampaolo P Romano and Robert A Antonia. Longitudinal and transverse structure functions in a turbulent round jet: effect of initial conditions and Reynolds number. *Journal of Fluid Mechanics*, 436:231–248, 2001.
- [28] Gu Xu and Robert Antonia. Effect of different initial conditions on a turbulent round free jet. *Experiments in Fluids*, 33(5):677–683, 2002.
- [29] Israel Wygnanski and Ho Fiedler. Some measurements in the self-preserving jet. *Journal of Fluid Mechanics*, 38(3):577–612, 1969.
- [30] Paolo Burattini, Robert A Antonia, and Luminita Danaila. Similarity in the far field of a turbulent round jet. *Physics of fluids*, 17(2):025101, 2005.
- [31] Alexis Darisse, Jean Lemay, and Azemi Benaïssa. Budgets of turbulent kinetic energy, Reynolds stresses, variance of temperature fluctuations and turbulent heat fluxes in a round jet. *Journal of Fluid Mechanics*, 774:95–142, 2015.
- [32] Bendiks J Boersma, Geert Brethouwer, and Frans TM Nieuwstadt. A numerical investigation on the effect of the inflow conditions on the self-similar region of a round jet. *Physics of fluids*, 10(4):899–909, 1998.
- [33] Bendiks J Boersma. Numerical simulation of the noise generated by a low Mach number, low Reynolds number jet. *Fluid Dynamics Research*, 35(6):425–447, 2004.
- [34] Seyed G Saddoughi and Srinivas V Veeravalli. Local isotropy in turbulent boundary layers at high reynolds number. *Journal of Fluid Mechanics*, 268:333–372, 1994.
- [35] Stavros Tavoularis and Stanley Corrsin. Experiments in nearly homogenous turbulent shear flow with a uniform mean temperature gradient. part 1. *Journal of Fluid Mechanics*, 104:311–347, 1981.
- [36] C Cambon, R Rubinstein, and FS Godeferd. Advances in wave turbulence: rapidly rotating flows. *New Journal of Physics*, 6(1):73, 2004.
- [37] José Gaité. Anisotropy in homogeneous rotating turbulence. *Physical Review E*, 68(5):056310, 2003.
- [38] X Shen and Z Warhaft. The anisotropy of the small scale structure in high reynolds number ( $r \lambda \gg 1000$ ) turbulent shear flow. *Physics of Fluids*, 12(11):2976–2989, 2000.

- [39] Susan Kurien and Katepalli R Sreenivasan. Anisotropic scaling contributions to high-order structure functions in high-reynolds-number turbulence. *Physical Review E*, 62(2):2206, 2000.
- [40] M Ferchichi and S Tavoularis. Reynolds number effects on the fine structure of uniformly sheared turbulence. *Physics of Fluids*, 12(11):2942–2953, 2000.
- [41] Theodore De Karman and Leslie Howarth. On the statistical theory of isotropic turbulence. *Proceedings of the Royal Society of London. Series A-Mathematical and Physical Sciences*, 164(917):192–215, 1938.
- [42] Andrey Nikolaevich Kolmogorov. The local structure of turbulence in incompressible viscous fluid for very large Reynolds numbers. *Cr Acad. Sci. URSS*, 30:301–305, 1941.
- [43] Laurent Mydlarski and Zellman Warhaft. On the onset of high-reynolds-number grid-generated wind tunnel turbulence. *Journal of Fluid Mechanics*, 320:331–368, 1996.
- [44] M Xu, A Pollard, J Mi, F Secretain, and H Sadeghi. Effects of reynolds number on some properties of a turbulent jet from a long square pipe. *Physics of Fluids*, 25(3):035102, 2013.
- [45] Trushar B Gohil, Arun K Saha, and K Muralidhar. Numerical study of instability mechanisms in a circular jet at low reynolds numbers. *Computers & Fluids*, 64:1–18, 2012.
- [46] Jonathan B Freund and Parviz Moin. Mixing enhancement in jet exhaust using fluidic actuators: direct numerical simulations. *ASME: FEDSM98*, 5235, 1998.
- [47] Koichi Tsujimoto, Koji Ao, Toshihiko Shakouchi, and Toshitake Ando. Numerical investigation on flow structures and mixing performances of vector-controlled free jet using dns. *Journal of Fluid Science and Technology*, 6(4): 401–411, 2011.
- [48] Sylvain Lardeau, Éric Lamballais, and Jean-Paul Bonnet. Direct numerical simulation of a jet controlled by fluid injection. *Journal of turbulence*, 3(3): N2, 2002.
- [49] Kyupaekc Jeff Rah, Chandru Dhandapani, and Guillaume Blanquart. Derivation of a realistic forcing term to reproduce the turbulent characteristics of round jets on the centerline. *Physical Review Fluids*, 3(8):084606, 2018. doi:[10.1103/PhysRevFluids.3.084606](https://doi.org/10.1103/PhysRevFluids.3.084606).
- [50] Phares L Carroll, Siddhartha Verma, and Guillaume Blanquart. A novel forcing technique to simulate turbulent mixing in a decaying scalar field. *Physics of Fluids*, 25(9):095102, 2013.

- [51] Nelson Wax. *Selected papers on noise and stochastic processes*. Courier Dover Publications, 1954.
- [52] Carlos Rosales and Charles Meneveau. Linear forcing in numerical simulations of isotropic turbulence: Physical space implementations and convergence properties. *Physics of Fluids*, 17(9):095106, 2005.
- [53] Stephen B Pope. *Turbulent flows*. Cambridge University Press, Cambridge, 2001.
- [54] Hussein J Hussein, Steven P Capp, and William K George. Velocity measurements in a high-Reynolds-number, momentum-conserving, axisymmetric, turbulent jet. *Journal of Fluid Mechanics*, 258:31–75, 1994.
- [55] Genrikh N Abramovich. The theory of turbulent jets. *Moscow Izdatel Nauka*, 1984.
- [56] Pui-Kuen Yeung and Stephen B Pope. Lagrangian velocity statistics obtained from direct numerical simulations of homogeneous turbulence. In *6th Symposium on Turbulent Shear Flows*, pages 3–7, 1987.
- [57] Pui-Kuen Yeung and Stephen B Pope. Lagrangian statistics from direct numerical simulations of isotropic turbulence. *Journal of Fluid Mechanics*, 207:531–586, 1989.
- [58] Alexandros P Vouros and Thrassos Panidis. Turbulent properties of a low Reynolds number, axisymmetric, pipe jet. *Experimental Thermal and Fluid Science*, 44:42–50, 2013.
- [59] Donald R Webster, Philip JW Roberts, and L Ra'ad. Simultaneous DPTV/PLIF measurements of a turbulent jet. *Experiments in Fluids*, 30(1):65–72, 2001.
- [60] Robert A Antonia, BR Satyaprakash, and Fazle Hussain. Measurements of dissipation rate and some other characteristics of turbulent plane and circular jets. *The Physics of Fluids*, 23(4):695–700, 1980.
- [61] Olivier Desjardins, Guillaume Blanquart, Guillaume Balarac, and Heinz Pitsch. High order conservative finite difference scheme for variable density low Mach number turbulent flows. *Journal of Computational Physics*, 227(15):7125–7159, 2008.
- [62] Thierry Passot and Annick Pouquet. Numerical simulation of compressible homogeneous flows in the turbulent regime. *Journal of Fluid Mechanics*, 181:441–466, 1987.
- [63] Phares L Carroll. *Towards understanding the mixing characteristics of turbulent buoyant flows*. PhD thesis, California Institute of Technology, 2014.

- [64] Geoffrey I Taylor. The spectrum of turbulence. *Proceedings of the Royal Society of London A: Mathematical, Physical and Engineering Sciences*, 164 (919):476–490, 1938.
- [65] F Thiesset, RA Antonia, and L Djenidi. Consequences of self-preservation on the axis of a turbulent round jet. *Journal of Fluid Mechanics*, 748, 2014.
- [66] Carl A Friehe, CW Van Atta, and Carl H Gibson. Jet turbulence: dissipation rate measurements and correlations. *AGARD Turbul. Shear Flows*, 18:1–7, 1971.
- [67] Kyupaekc Jeff Rah and Guillaume Blanquart. Numerical forcing scheme to generate passive scalar mixing on the centerline of turbulent round jets in a triply periodic box. *Physical Review Fluids*, (Under review).
- [68] VD Zimin and PG Frik. Averaged temperature fields in asymmetrical turbulent streams over localized heat sources. *Fluid Dynamics*, 12(2):335–339, 1977.
- [69] AD Birch, DR Brown, MG Dodson, and JR Thomas. The turbulent concentration field of a methane jet. *Journal of Fluid Mechanics*, 88(3):431–449, 1978.
- [70] Paul CK Chu, Joseph H Lee, and Vincent H Chu. Spreading of turbulent round jet in coflow. *Journal of Hydraulic Engineering*, 125(2):193–204, 1999.
- [71] Susan M Anderson and Klaus Bremhorst. Investigation of the flow field of a highly heated jet of air. *International journal of heat and fluid flow*, 23(2): 205–219, 2002.
- [72] Emmanuel Ruffin, R Schiestel, Fabien Anselmet, Muriel Amielh, and L Fula-chier. Investigation of characteristic scales in variable density turbulent jets using a second-order model. *Physics of Fluids*, 6(8):2785–2799, 1994.
- [73] Siddhartha Verma, Y Xuan, and Guillaume Blanquart. An improved bounded semi-lagrangian scheme for the turbulent transport of passive scalars. *Journal of Computational Physics*, 272:1–22, 2014.
- [74] R Chevray and NK Tutu. Intermittency and preferential transport of heat in a round jet. *Journal of Fluid Mechanics*, 88(1):133–160, 1978.
- [75] Yan Antoine, Fabrice Lemoine, and Michel Lebouché. Turbulent transport of a passive scalar in a round jet discharging into a co-flowing stream. *European Journal of Mechanics-B/Fluids*, 20(2):275–301, 2001.
- [76] SK Lee, L Djenidi, and RA Antonia. Spectral method for determining mean dissipation rates of turbulent kinetic energy and passive scalar variance. In *Proc. 18th Australas. Fluid Mech. Conf. Paper*, volume 259, 2012.

- [77] David R Dowling and Paul E Dimotakis. Similarity of the concentration field of gas-phase turbulent jets. *Journal of Fluid Mechanics*, 218:109–141, 1990.
- [78] JC Duffet and A Benaïssa. Influence of initial conditions on the evolution towards similarity of passive scalar in turbulent round jets. *Experimental Thermal and Fluid Science*, 44:834–843, 2013.
- [79] Katepalli R Sreenivasan. On local isotropy of passive scalars in turbulent shear flows. *Proc. R. Soc. Lond. A*, 434(1890):165–182, 1991.
- [80] Patrice Mestayer. Local isotropy and anisotropy in a high-reynolds-number turbulent boundary layer. *Journal of Fluid Mechanics*, 125:475–503, 1982.
- [81] S Pond. Smith, s. d., hamblin, pf & burling, rw. *J. Atmos. Sci.*, 1966:23–376, 1966.
- [82] Sheldon K Friedlander et al. *Smoke, dust, and haze*, volume 198. Oxford university press New York, 2000.
- [83] RV Vincent and NA Hill. Bioconvection in a suspension of phototactic algae. *Journal of Fluid Mechanics*, 327:343–371, 1996.
- [84] Carlo Gualtieri, Athanasios Angeloudis, Fabian Bombardelli, Sanjeev Jha, and Thorsten Stoesser. On the values for the turbulent schmidt number in environmental flows. *Fluids*, 2(2):17, 2017.
- [85] AM Oboukhov. Struktura temperaturnovo polia v turbulentnom potoke. *Izv. Akad. Nauk SSSR Ser. Geofiz.*, 3:59, 1949.
- [86] Stanley Corrsin. On the spectrum of isotropic temperature fluctuations in an isotropic turbulence. *Journal of Applied Physics*, 22(4):469–473, 1951.
- [87] George K Batchelor. Small-scale variation of convected quantities like temperature in turbulent fluid part 1. general discussion and the case of small conductivity. *Journal of Fluid Mechanics*, 5(1):113–133, 1959.
- [88] Carl H Gibson. Kolmogorov similarity hypotheses for scalar fields: sampling intermittent turbulent mixing in the ocean and galaxy. *Proceedings of the Royal Society of London. Series A: Mathematical and Physical Sciences*, 434(1890):149–164, 1991.
- [89] Satoru Komori, Takao Kanzaki, and Yasuhiro Murakami. Simultaneous measurements of instantaneous concentrations of two reacting species in a turbulent flow with a rapid reaction. *Physics of Fluids A: Fluid Dynamics*, 3(4):507–510, 1991.
- [90] Paul L Miller and Paul E Dimotakis. Stochastic geometric properties of scalar interfaces in turbulent jets. *Physics of Fluids A: Fluid Dynamics*, 3(1):168–177, 1991.

- [91] Paul L Miller and Paul E Dimotakis. Reynolds number dependence of scalar fluctuations in a high schmidt number turbulent jet. *Physics of Fluids A: Fluid Dynamics*, 3(5):1156–1163, 1991.
- [92] Paul L Miller and Paul E Dimotakis. Measurements of scalar power spectra in high schmidt number turbulent jets. *Journal of Fluid Mechanics*, 308: 129–146, 1996.
- [93] Marie-Caroline Jullien, Patrizia Castiglione, and Patrick Tabeling. Experimental observation of batchelor dispersion of passive tracers. *Physical review letters*, 85(17):3636, 2000.
- [94] RA Antonia and P Orlandi. Effect of schmidt number on small-scale passive scalar turbulence. *Applied Mechanics Reviews*, 56(6):615–632, 2003.
- [95] FTM Nieuwstadt and G Brethouwer. Turbulent transport and mixing. *Advances in Turbulence VIII*, pages 133–140, 2000.
- [96] Gregory C Burton. The nonlinear large-eddy simulation method applied to  $Sc \approx 1$  and  $Sc \gg 1$  passive-scalar mixing. *Physics of Fluids*, 20(3):035103, 2008.
- [97] Gregory C Burton. Scalar-energy spectra in simulations of  $Sc \gg 1$  mixing by turbulent jets using the nonlinear large-eddy simulation method. *Physics of Fluids*, 20(7):071701, 2008.
- [98] Parviz Moin, Kyle Squires, W Cabot, and Sangsan Lee. A dynamic subgrid-scale model for compressible turbulence and scalar transport. *Physics of Fluids A: Fluid Dynamics*, 3(11):2746–2757, 1991.
- [99] Charles D Pierce and Parviz Moin. A dynamic model for subgrid-scale variance and dissipation rate of a conserved scalar. *Physics of Fluids*, 10(12): 3041–3044, 1998.
- [100] C Jiménez, F Ducros, Benedicte Cuenot, and Benoit Bédard. Subgrid scale variance and dissipation of a scalar field in large eddy simulations. *Physics of Fluids*, 13(6):1748–1754, 2001.
- [101] Guillaume Balarac, Heinz Pitsch, and Venkat Raman. Development of a dynamic model for the subfilter scalar variance using the concept of optimal estimators. *Physics of fluids*, 20(3):035114, 2008.
- [102] Dale I Pullin. A vortex-based model for the subgrid flux of a passive scalar. *Physics of Fluids*, 12(9):2311–2319, 2000.
- [103] MRH Sheikhi, TG Drozda, P Givi, and SB Pope. Velocity-scalar filtered density function for large eddy simulation of turbulent flows. *Physics of fluids*, 15(8):2321–2337, 2003.

- [104] Robert H Kraichnan. Small-scale structure of a scalar field convected by turbulence. *The Physics of Fluids*, 11(5):945–953, 1968.
- [105] Paul E Dimotakis and Paul L Miller. Some consequences of the boundedness of scalar fluctuations. *Physics of Fluids A: Fluid Dynamics*, 2(11):1919–1920, 1990.
- [106] Chandru Dhandapani, Kyupaekc Jeff Rah, and Guillaume Blanquart. Effective forcing for direct numerical simulations of the shear layer of turbulent free shear flows. *Physical Review Fluids*, 2019.
- [107] Jan Beran. *Statistics for long-memory processes*. CRC Press, 1994.
- [108] MJ Lee and WC Reynolds. Numerical experiments on the structure of homogeneous turbulence. rep. tf-24. department of mechanical engineering, 1985.
- [109] PK Yeung and SB Pope. An algorithm for tracking fluid particles in numerical simulations of homogeneous turbulence. *Journal of computational physics*, 79(2):373–416, 1988.
- [110] Darek Bogucki, J Andrzej Domaradzki, and PK Yeung. Direct numerical simulations of passive scalars with  $Pr > 1$  advected by turbulent flow. *Journal of Fluid Mechanics*, 343:111–130, 1997.
- [111] Lian-Ping Wang, Shiyi Chen, and James G Brasseur. Examination of hypotheses in the kolmogorov refined turbulence theory through high-resolution simulations. part 2. passive scalar field. *Journal of Fluid Mechanics*, 400: 163–197, 1999.
- [112] Henk A Van der Vorst. Bi-cgstab: A fast and smoothly converging variant of bi-cg for the solution of nonsymmetric linear systems. *SIAM Journal on scientific and Statistical Computing*, 13(2):631–644, 1992.